SoLID Heavy Gas Cherenkov and DEMP Event Generator

A Thesis

Submitted to The Faculty of Graduate Studies and Research

In Partial Fulfillment of the Requirements

For the Degree of

Master of Science

in

Physics

University of Regina

By

Rory Stephen Evans

Regina, Saskatchewan

August, 2019

Abstract

The future Solenoidal Large Intensity Device (SoLID) at Jefferson Lab will enable a new series of high luminosity, large acceptance, fixed angle experiments [1]. These include the proposed Semi-Inclusive Deep Inelastic Scattering (SIDIS) series of experiments [2][3][4]. The requirements of one of the SIDIS experiments coincides with those for a measurement of the transverse nucleon, single-spin asymmetries $A_{UT}^{\sin(\mu\phi+\lambda\phi_S)}$, in particular, the largest two, $A_{UT}^{\sin(\phi-\phi_S)}$ and $A_{UT}^{\sin(\phi_S)}$. These asymmetries are of high value to the study of Generalized Parton Distributions (GPDs), as they are believed to be highly sensitive to the most poorly known GPD, $\tilde{E}$. As such, the SoLID Deep Exclusive Meson Production (DEMP) experiment has been proposed to run parasitically with the SIDIS experiment. In this thesis, model-based asymmetry data are parameterized as part of cross section calculations in a Monte-Carlo event generator for use in the experimental proposal [5]. This thesis also details a complete rewrite of this event generator in order to improve computation time, readability, and stability, enabling greater statistics for further studies.

A critical component of the SoLID apparatus is the Heavy Gas Cherenkov (HGC), which is used for $\pi^{\pm}$ identification. The University of Regina has received funding from CFI and the Fedoruk Institute to build a prototype segment HGC. A key requirement of the HGC is to maintain a 1.5 atm operating pressure, with minimal leaking over long periods, while also having a thin, low-Z entry window. This thesis investigates solutions for the entry window using different materials, finding the optimal solution to be a hard carbon fiber shell to take the stress of the elevated pressure, with Mylar providing the air-tightness.

Acknowledgments

I'd like to give my first and foremost thanks to my thesis adviser, Prof. Garth Huber, for mentoring and guiding me through this project, and for helping me when I couldn't see the forest for the trees.

My deepest gratitude to Zafar Ahmed and Zhihong Ye for laying the ground work for the DEMP Event Generator, and taking the time to answer my questions, without which, I could not have completed the project.

My thanks to Gary Swift and Zhiwen Zhao at Duke University for their invaluable feedback on the HGC window prototyping, and their work towards completion of the HGC project.

Special thanks to Derek Gervais and Lorenz Weber for their tireless work in the machine shop, constructing the window prototypes and testing apparatus.

For my fellow students and office-mates, Ryan Ambrose, Samip Basnet, Dilli Paudyal, Wenliang Li, and Ahmed Foda, thank you for the moral support, lunch outings, trivia nights, and for tolerating my rants about ROOT code.

Finally, thank you to University of Regina, NSERC, CFI, and Fedoruk Institute for their funding.

Contents

List of Figures

List of Abbreviations

CEBAF	Continuous Electron Beam Accelerator Facility
CERN	The European Organization for Nuclear Research
CINT	Command-line C/C++ Interpreter
DEMP	Deep Exclusive Meson Production
DIS	Deep Inelastic Scattering
EC	Electromagnetic Calorimeter
EC	Large Angle Electromagnetic Calorimeter
EC	Forward Angle Electromagnetic Calorimeter
FSI	Final State Interactions
GEM	Gas Electron Multiplier
GK model	Goloskokov and Kroll GPD model
GPD	Generalized Parton Distribution
GWS	Glashow-Weinberg-Salam
HGC	Heavy Gas Cherenkov Detector
JLab	Thomas Jefferson National Accelerator Facility
LGC	Light Gas Cherenkov Detector
LTCC	Low Threshold Cherenkov Detector
MRPC	Multi-Gap Resistive Plate Chamber detector
PDF	Parton Distribution Function
PDG	Particle Data Group Review
PET	Polyethylene Terephthalate
PMT	Photomultiplier Tube

pQCD	Perturbative Quantum Chromodynamics
PVDIS	Parity Violating Deep Inelastic Scattering
QCD	Quantum Chromodynamics
QED	Quantum Electrodynamics
QFT	Quantum Field Theory
SIDIS	Semi-inclusive Deep Inelastic Scattering
SoLID	Solenoidal Large Intensity Device
UML	Unbinned Maximum Likelihood
VR model	Vrancx-Ryckebusch model

Chapter 1

Physics Background

Before introducing the DEMP experiment and the physics motivations behind it, it is important to develop and discuss some foundational concepts.

1.1 The Standard Model of Particle Physics

The theoretical framework describing fundamental particles and their interactions, one of the most successful theories to date, is known as "The Standard Model of Particle Physics" (often, simply, "The Standard Model"). The best-known component of The Standard Model is the "Particle Zoo", visualized in diagrams such as Fig. 1.1. This diagram details the fundamental properties of all known fundamental (or elementary) particles; that is, particles which may not be divided further into constituent particles. Fundamental Particles have no internal structure and are considered "point like". Particles are divided into two broad categories: Fermions, having half-integer spin quantum number, make up the building blocks of matter, and Bosons, having integer spin quantum number, act as mediators of the fundamental interactions.

The Standard Model also describes the interactions between these particles via three of the four known fundamental forces (or interactions): the electromagnetic, weak nuclear, and strong nuclear interactions. The mathematical framework describing these interactions is Quantum Field Theory (QFT). QFT is only a framework however, not an all-encompassing theory for interactions under the Standard Model. Several QFTs fall under the umbrella of the Standard Model, each dealing with different interactions. The oldest, simplest, and most thoroughly verified of these theories is Quantum Electrodynamics (QED). QED describes the electromagnetic interactions between charged particles and photons (the boson associated with the elec-

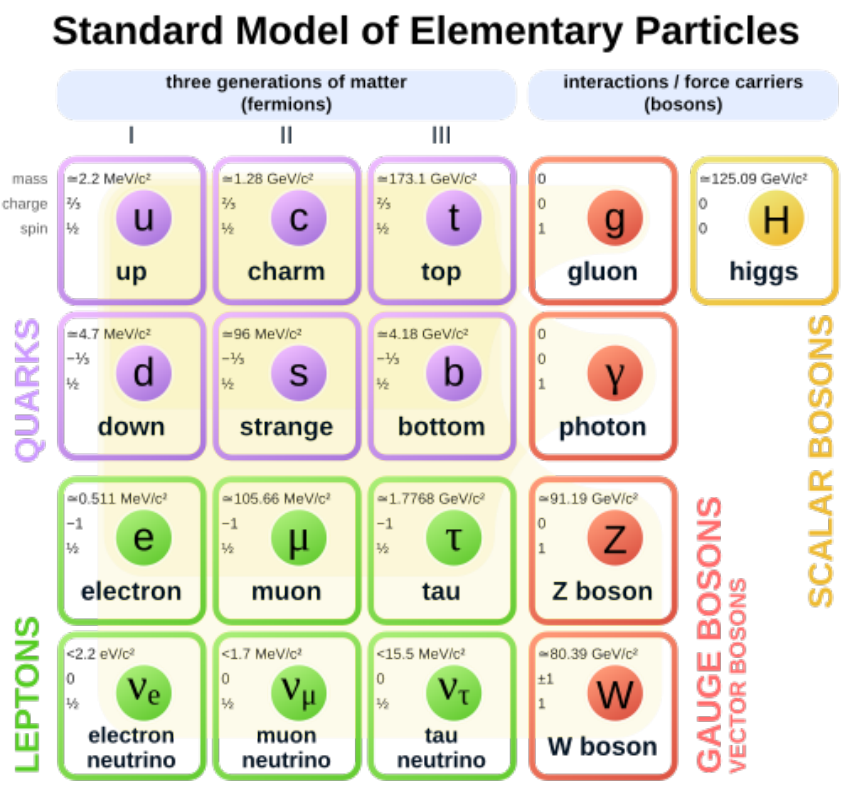

Figure 1.1: Elementary Particles of the Standard Model are organised into categories of fermions (particles of half-integer spin) and bosons (particles of integer spin), further grouped into quarks, leptons, and their three generations (for the fermions), gauge bosons and scalar bosons (consisting only of the higgs boson). Indicated with each particles is its mass, charge (in units of the elementary charge), and the spin quantum number [6].

tromagnetic interaction, often referred to as the "mediator"). The weak nuclear interaction is best described by the Glashow-Weinberg-Salam (GWS) theory [7], sometimes called flavordynamics, or electroweak theory. GWS theory models interactions between particles according to their flavor quantum numbers, mediated by the neutral Z bosons, and the charged W bosons. All quarks and leptons experience interactions via the weak interaction, with neutrinos being the only particles to interact with it exclusively (they also interact gravitationally, having mass, but both these facts go beyond the Standard Model). This theory can also describe the electromagnetic interaction, as well as the weak interaction, treating them as two manifestations of a singular electroweak interaction.

The strong nuclear interaction is described by Quantum Chromodynamics (QCD), so named for its use of "color" in place of charge as the property responsible for the interaction. Only the quarks interact with the strong interaction, with gluons acting as the mediating boson. QCD has proved highly successful at high

interaction energies, where perturbative expansions of the theory are feasible.

The strong force is responsible for binding quarks together into composite particles called hadrons. Hadrons are far more numerous in variety than elementary particles, but can be broken down into two categories: mesons, consisting of a quark-antiquark valence pair, and baryons, consisting of three valence quarks. Valence quarks are those which carry the quantum numbers of the hadron, and are distinguished from other, virtual, particles appearing within the hadron due to the uncertainty principle. Hadrons of particular relevance to this work include: the charged pion, a meson consisting of either an up-antidown quark pair, or down-antiup quark pair; the proton, consisting of two up quarks and a down quark; and the neutron, consisting of two down quarks and an up quark. Together, protons and neutrons are known as nucleons, being the particles making up the atomic nuclei of all matter in the universe, with mesons (particularly pions) acting as the mediator binding them together.

Clearly, QCD is central to understanding the structure of subatomic matter. However, the energy scale of the interactions binding quarks into hadrons, and subsequently nucleons into nuclei, is much lower than the high energy that allows for a perturbative analysis. For reasons that will be shown in the following sections, as the energy decreases, higher order terms become more and more significant. This renders perturbative QCD (pQCD) ineffective at modeling the internal structure and dynamics of composite particles. While there exist successful theories modeling the binding of nucleons into nuclei (quantum hadrodynamics), occurring at lower energies, the intermediate energy region, where quark binding (hadronization) occurs, is much less understood. It is to this intermediate energy region that this work pertains.

1.2 Feynman diagrams

An invaluable tool in QFT is the Feynman diagram. A Feynman diagram is a graphical representation of the sometimes large and complicated integrals involved in calculating the probability amplitudes of particle interactions. Their use extends beyond such calculations, however, as they provide a helpful visualization, and insight into the behavior of the underlying mathematics.

In a typical Feynman diagram, a specific direction is chosen to represent the passage of time. In this work, time is selected to flow from left to right. Particles are represented by vectors in the diagram. Typically, particles are drawn with arrows pointing forwards in time, and anti-particles (such as a positron) are drawn pointing backwards in time (though this should not be taken literally). The interactions between particles are indicated by vertices connecting the vectors. Particle vectors with an end not connected to a vertex

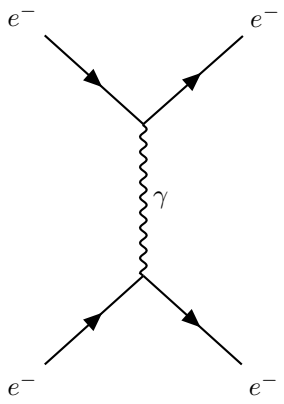

Figure 1.2: Feynman diagram showing Møller scattering to first order, in which two electrons interact via the exchange of a single virtual photon, γ. Time flows from left to right.

are considered real particles, which exist in some other state (whether free or bound) before or after the interaction, having mass equal to the mass listed in Fig. 1.1. Fully internal particle vectors represent virtual particles, which may have masses different from those given in Fig. 1.1 (for example, while real photons are always massless, a virtual photon may have mass). For example, Fig. 1.2 shows Møller scattering, the QED analog to Coulomb repulsion, in which two electrons interact via a virtual photon.

Formally, Feynman diagrams are drawn with stringent rules and limitations assuring that fundamental laws are correctly adhered to. This includes restrictions on which types of particle vectors, and how many, may connect at vertices. For example, photons do not interact directly with other photons, and as such no vertex may have two photons connected to it. Each of the three QFTs (QED, QCD, and GWS) have a set of fundamental vertices which form the building blocks for any particle interaction [8]. These fundamental vertices are shown in Fig. 1.3.

Most of these vertices, however, cannot represent physical processes when alone. The Feynman rules enforce conservation laws, including energy and momentum. For example, the basic QED vertex can be viewed as annihilation of an electron and a positron into a single photon, however, if viewed in the center of mass frame, the total momentum is, obviously, zero. It is not possible for a real photon to have zero momentum in any reference frame, and thus, the interaction is only possible for virtual photons.

Energy and momentum are not the only quantities which must be conserved, though many conservation rules are dependent on the type of interaction. Every quark carries a baryon quantum number of $\frac{1}{3}$ ($-\frac{1}{3}$ for antiquarks, thus all baryons have a baryon number of one, and mesons a baryon number of zero), which must be conserved through all interactions. Similarly (anti)leptons (including neutrinos) each have a lepton number of $+(-)1$, which must be conserved. Charge number is also conserved in all interactions. Each quark

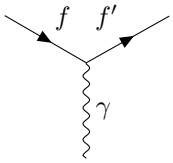

(a) Fundamental QED vertex. The lines labeled f and f' indicate charged fermions. Time may flow in any direction.

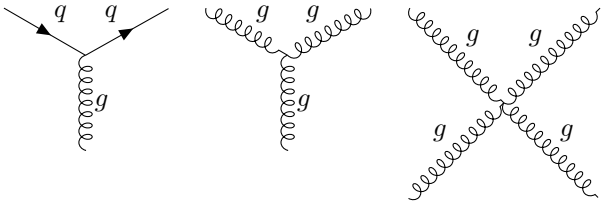

(b) Fundamental QCD vertices showing quark-gluon interaction, and gluon-gluon interaction. The lines labeled q indicate quarks, and g, gluons. Time may flow in any direction.

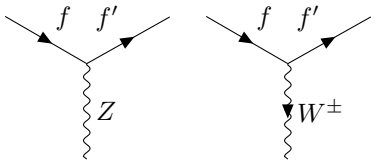

(c) Fundamental neutral (left) and charged (right) GWS vertices. The lines labeled f and f' indicate fermions (including either quarks or leptons). Time may flow in any direction.

Figure 1.3: Fundamental vertices for the three Quantum Field Theories: QED (top), QCD (middle), and GWS (bottom). These vertices function as "building blocks" for Feynman diagrams in the standard model [8].

species has an associated flavor quantum number, which is conserved through strong and electromagnetic interactions, but not through the weak interaction.

There are many more considerations in drawing a valid, and physical, Feynman diagram, but the above covers those rules relevant to the reactions of interest to this work. While these rules are stringently applied to any formal Feynman diagram, this is primarily to enforce rigor in the underlying mathematics. In many cases, visually similar, but less rigorous, cartoons are useful in demonstrating particle interactions conceptually, and are used frequently in the following sections.

An important feature of the Feynman rules is that each vertex has an associated coupling constant. This constant acts as scaling factor on the calculated probability amplitude, and characterizes the strength of the interaction. For QED, the coupling constant is the fine structure constant: $\alpha \approx \frac{1}{137}$. This implies that, with all else equal, every additional vertex in the diagram represents a 137-times less likely process.

This provides a visual interpretation of the perturbative expansion, where the diagram with least number of vertices for a given set of incoming and outgoing particles is the leading order process, or tree-level diagram. For example, Fig. 1.2 is the leading order process for Møller scattering. Adding more vertices gives higher order terms in the expansion. Fig. 1.4 shows some example Feynman diagrams for Møller scattering at second order. These diagrams have four vertices (three isn't possible within the Feynman rules), compared to leading order with only two. Experimentally, however, the virtual particles, represented by fully internal lines, cannot be detected. The incoming and outgoing particles are the same in all cases and so the processes are indistinguishable. As such, the probability must be summed over all possible diagrams. But, as mentioned, terms of increasingly higher order are exponentially less likely. A leading order, or at most next-to-leading-order, is almost always sufficient for QED.

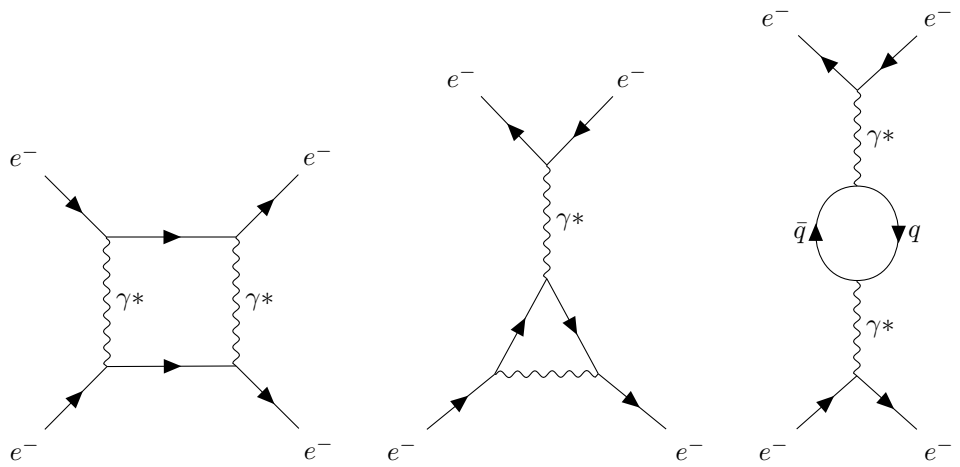

Figure 1.4: Some second order Feynman diagrams showing Møller scattering. Time flows left to right. $q\bar{q}$ indicates any charged fermion/antifermion pair [8].

1.3 Scattering Experiments

The following discussion is based on chapter 6 of "Subatomic Physics" by Hans Frauenfelder and Ernest M. Henley [9]. The mathematical framework of the Standard Model is usually connected to experiment through either decay rates, or scattering cross sections. Decay rates concern unstable particle states spontaneously transitioning to more stable states, typically with a greater total number of particles. The initial state is either a single elementary particle, or multiple particles bound in an unstable state.

In a scattering experiment, the initial state consists of two or more particles incident upon one another. Given the prior example of Møller scattering, one of the initial electrons may be bound as part of an atom in a solid target, while the other is fired as part of a beam of electrons. Scattering itself refers to the deflection of an incident particle away from its original trajectory as a result of the interaction. The cross section for a scattering process represents the probability of the process occurring in a way that is independent of the experiment. The simplest way to define a cross section is as follows: If a beam of incident particles with flux F is incident on a stationary target with N scattering centers (target particles) per unit area, then the total number of scattered particles, $\mathcal{N}_S$ per unit time is:

$$\mathcal{N}_S = FN\sigma_{tot} \tag{1.1}$$

where σ_{tot} is the total scattering cross section.

What is frequently more useful, however, is the differential scattering cross section. Where the total

cross section represents the probability of the process occurring anywhere in its phase space (the possible energy and momenta of the particles), many detectors will only be able to observe some fraction of this phase space at a time. This differential cross section will most frequently be a function of scattering angle, and often other variables like the energy of the scattered particle, or the momentum transfer in the reaction. For example, the differential scattering cross section for a spin-$\frac{1}{2}$ charged particle, scattering off of a spinless target, is [9]

$$\left(\frac{d\sigma}{d\Omega}\right)_{\text{Mott}} = 4(Ze^2)^2 \frac{E^2}{(|\vec{q}|c)^4}\left(1 - \beta^2 \sin^2\frac{\theta}{2}\right) \tag{1.2}$$

where $d\Omega = sin\theta d\theta d\phi$ is a differential solid angle, Z is the charge of the target, E is the energy of the incident particle, $\vec{q}$ is the momentum transfer, β is the incident particle velocity in units of c, e is the elementary charge (i.e. magnitude of the charge of an electron), and θ is the scattering angle. This is known as the Mott cross section [10]. It is based on a few simplifications however: it applies only to point particles, interacting via a single photon, with no recoil in the target. Probing of the interiors of particles with internal structure begins at its most simple with elastic scattering.

In elastic scattering, the scattered particle interacts, to leading order, with the target as a single object (rather than interacting with, say, a single quark) as indicated in Fig. 1.5. Given an incident electron with momentum $\vec{p_i}$ and scattered electron with momentum $\vec{p_f}$, the scattering cross section may be factorized as a product of the scattering cross section for a point particle (Mott cross section) and a form factor, which is a function of momentum transfer $\vec{q} = \vec{p_i} - \vec{p_f}$:

$$\left(\frac{d\sigma}{d\Omega}\right) = \left(\frac{d\sigma}{d\Omega}\right)_{Mott} |F(\vec{q})|^2$$

A simplified interpretation of the form factor is as analogous to the Fourier transform of the charge distribution from position to momentum space, although this only holds when assuming zero recoil in the target particle.

The above assumes a single photon interaction, as shown in Fig. 1.5. Higher-order interactions, such as the examples in Fig. 1.6, give rise to different kinematics, which break down the factorization of the form factor. As discussed previously, the measured cross section will include these higher-order interactions. However, as described by the Feynman rules, the scattering amplitude for each of these second order processes is on the order of 1/137 times the scattering amplitude of the first order process. The single photon approximation is thus usually sufficient, but next to leading order can be handled if necessary.

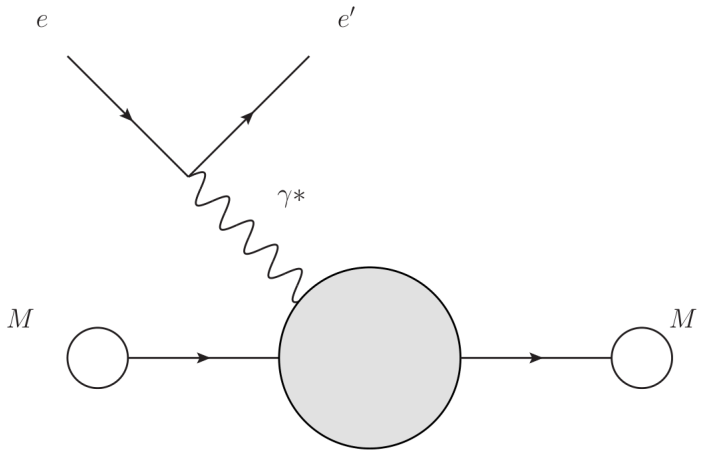

Figure 1.5: Leading order elastic scattering off a nucleus or single nucleon of mass M, in which the electron interacts with the target as a whole via a single virtual photon. The circles represent higher order processes which are either not explicitly considered, or are being probed in the experiment. The white circles represent binding of the nuclear or hadronic states, and the gray circle represents the target interacting with the photon collectively, and hides the physics of the internal interactions binding the nucleus or nucleon.

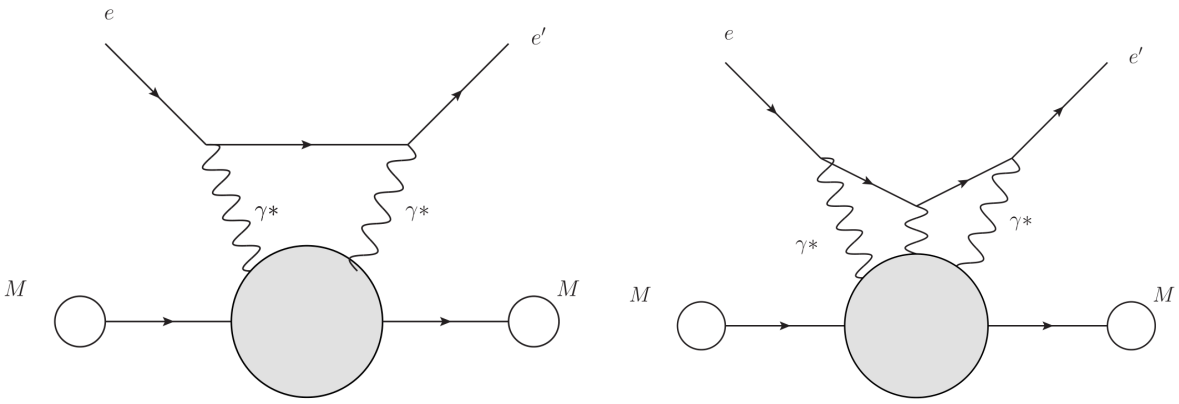

(a) Second order interaction.

(b) Third order interaction.

Figure 1.6: Elastic scattering in which the electron interacts via two (left) and three (right) virtual photon exchanges.

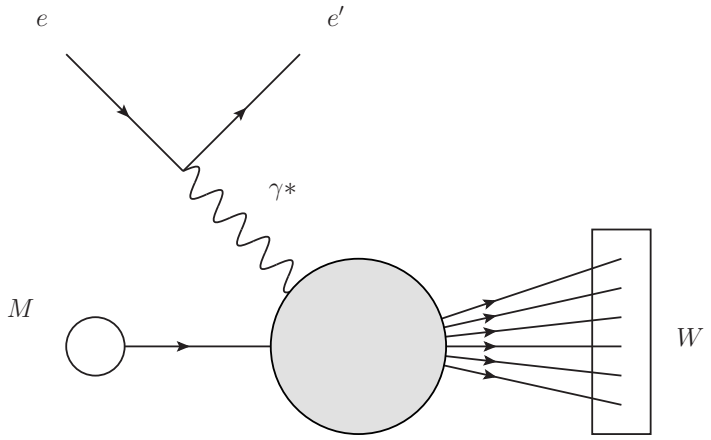

Figure 1.7: General Feynman cartoon for inelastic electron scattering. The blobs represent the higher order processes. The white blob represents the binding of the initial nuclear or hadron state. The gray blob represents the processes by which the final state is produced. The final states are a collection of hadrons with total mass W.

1.4 Deep Inelastic Scattering (DIS)

For inelastic electron scattering, the invariant mass of the final hadronic state may differ to varying degrees from the initial hadronic state. Fig. 1.7 shows the general Feynman-like diagram for fully inclusive inelastic scattering. Once again, a single photon interaction is assumed, but in principle, more photon interactions may be included. However, the same logic applies as with elastic scattering, and the single photon approximation can be taken as sufficient for experimental purposes. This diagram indicates an initial hadronic state, which may be a single nucleon or a heavier nucleus, being struck by the electron via some "hidden" interactions.

Since the initial and final mass are different, the differential scattering cross section is not only a function of the transferred momentum (i.e. scattering angle), but also of the energy transfer. Here, a frame-independent formalism is used, and we introduce the concept of four-momentum: $p = (E/c, p_x, p_y, p_z)$. q is the four-momentum of the virtual photon, then q^2 is taken to be the square of the four-momentum transfer:

$$q^2 = -Q^2 = \frac{(E - E')^2}{c^2} - |\vec{p} - \vec{p'}|^2 \tag{1.3}$$

where E and E' are the initial and final energy of the electron, and $\vec{p}$ and $\vec{p'}$ are the initial and final

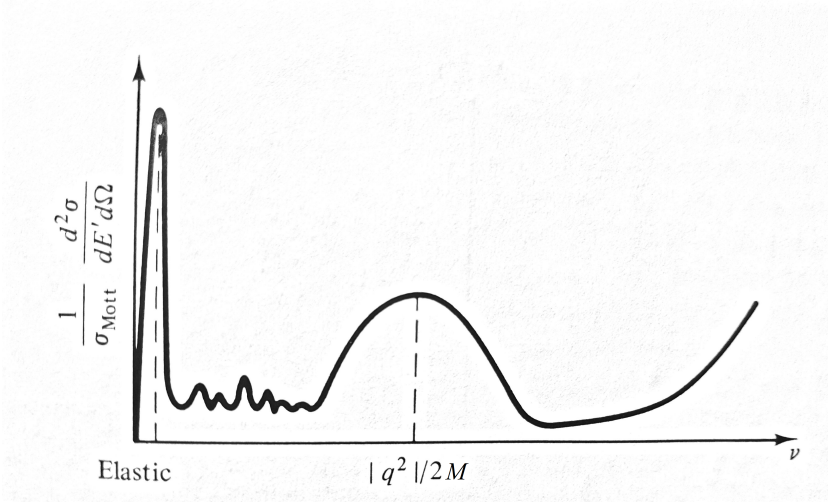

Figure 1.8: Sketch of typical inelastic differential scattering cross section off of a nucleus, normalized by the Mott cross section [9]. The horizontal axis is in units of energy, typically on the order of 10s of MeV.

three-momenta of the electron. One can also define the energy loss of the electron:

$$\nu = E - E' = \frac{q \cdot P}{M} \tag{1.4}$$

where P is the four-momentum of the nucleon with mass M, and the invariant mass of the final system of hadrons with electron mass m_e) is:

$$W^2 = m_e^2 c^4 + q^2 c^2 + 2\nu m_e c^2 \tag{1.5}$$

These quantities are invariant under relativistic coordinate transforms (Lorentz invariant). Since the interaction now depends on two variables, the double differential scattering cross section: $d^2\sigma/dE'd\Omega$ must be used. Fig 1.8 shows a typical double differential scattering cross section, normalized by the Mott cross section, for inelastic scattering off of a nucleus. At low values of ν, one may see the peak corresponding to elastic scattering, followed by several smaller peaks corresponding to excited nuclear states. The broader peak, indicated at $\nu = |q^2|/2m$, corresponds to the quasi-elastic peak, where the photon interacts with a single nucleon of mass m, which is typically ejected from the nucleus. Beyond the quasi-elastic peak is the continuum region, and higher still is where the production of pions and higher mass particles occurs.

Probing of the nuclear structure with inelastic scattering is possible with projectile energies in the range of up to 100 MeV. At higher energies, the electron can be considered to interact with a single nucleon, as shown in Fig. 1.9. This is the general, inclusive, interaction. Fig. 1.10 shows the behavior of inelastic scattering

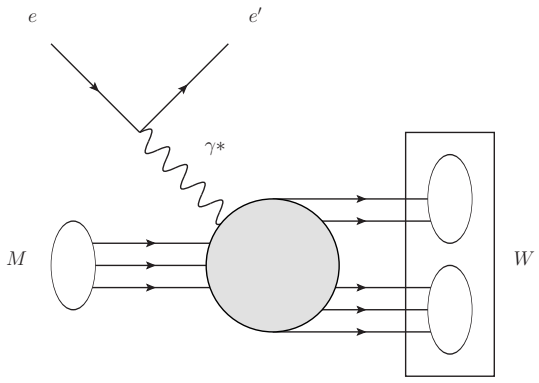

Figure 1.9: Leading order general Feynman diagram for fully inclusive DIS. The final hadronic state, with mass W, in this example is shown as a baryon and a meson, but in principle may include many more mesons. It may also contain additional baryons and anti-baryons in equal numbers, the only requirement being that baryon number is conserved. The blobs represent higher order processes. The white blobs represent hadron states, and the gray blob represents interactions between partons leading to the final state. The physics hidden within this blob are what is being probed by such an experiment.

with a proton. It displays many of the same features as Fig. 1.8, but on an energy scale approximately 100 times larger. The resonance peaks once again indicate excited states of the target, i.e. the proton. This on its own is enough to clearly imply deeper structure within the nucleon, as only composite objects can have excited states. More detailed experimental analysis of scattering into the continuum region reveals Mott-like form factors. This means the proton contains point scatterers, which are now known to be quarks. Scattering experiments of this kind are known as Deep Inelastic Scattering (DIS), as they probe "deep" within the nucleon.

In the GeV energy range, it becomes possible for the electron to interact with a single quark, as such one may "peel back" the gray blob in Fig. 1.9 and consider some specific possibilities. Some examples for inelastic scattering off of a proton are shown in Figs. 1.11 and 1.12. These diagrams now include the gluons, indicating strong interactions between quarks [11].

Figs. 1.11 and 1.12 show only a single gluon interaction in the production of the pion (that is, not including the binding of the hadrons, indicated by the white blobs). This is referred to as a hard interaction, and is described well by pQCD. However, as shown by Fig. 1.13, the strong coupling constant, α_s, depends heavily on the four-momentum transfer. At lower momentum transfer, α_s is close enough to one, that the higher order terms become much more significant. Fig. 1.14 shows some second order versions of the interactions in Fig. 1.11, by use of gluon vertex corrections.

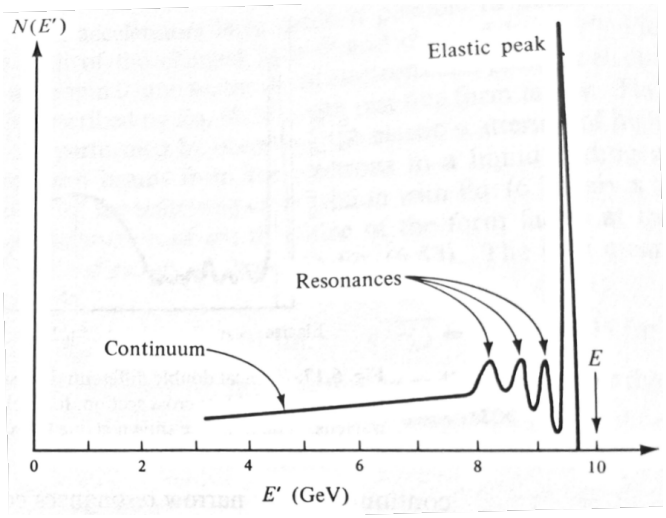

Figure 1.10: Inelastic electron scattering of a proton, giving rise to a series of baryonic "resonances" up to 2 GeV lower than the elastic scattering peak, and the DIS continuum at much lower energies. [9]

The higher order interactions are further complicated by considering gluon-gluon interactions. Similar examples are shown in Fig. 1.15. These different corrections can be combined together in a multitude of different ways. One can see, then, how for large α_s the higher order interactions, while each of smaller amplitude, can collectively overwhelm the first order interactions. One can also see that attempting to account for all possibilities beyond next to leading order would quickly become unmanageable.

The leading order approximation is also the basis of the perturbative analysis, so pQCD fails to describe these interactions. As such, they are collectively termed soft interactions, and separated from the leading order, hard interactions. The study of the soft interactions is then left to experiment (as well as Monte Carlo based lattice QCD).

DIS assumes only hard scattering. In this regime, the scattering cross section may be found in terms of two structure functions, W_1 and W_2, which are functions of ν and q^2:

$$\frac{d^2\sigma}{d|q|^2 d\nu} = \frac{4\pi\alpha^2\hbar^2 E'}{q^4 mc^2 E}\left[W_1(q^2,\nu)\cos^2\left(\frac{\theta}{2}\right) + 2W_2(q^2,\nu)\sin^2\left(\frac{\theta}{2}\right)\right]. \tag{1.6}$$

In the limit that $q^2, \nu \to \infty$ but the ratio is finite, these functions depend only on a quantity known as the Bjorken x:

$$x = \frac{-q^2}{2m\nu}. \tag{1.7}$$

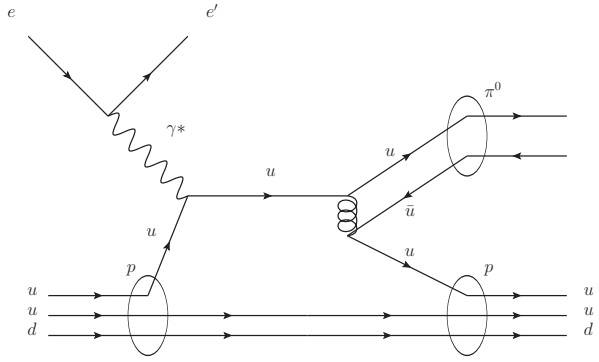

(a) Neutral pion production via the up quark.

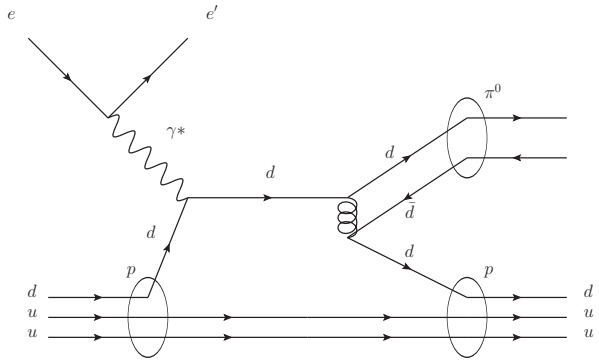

(b) Neutral pion production via the down quark.

Figure 1.11: Leading order Feynman diagrams for production of a neutral pion via interaction with a proton. The white blobs indicate higher order processes binding the incoming and outgoing hadrons together.

The structure functions then reduce to longitudinal Parton Distribution Functions (PDFs). In the high q^2 limit, the variable x may be interpreted as the fraction of the momentum carried by the struck parton, and the PDFs then give the probability of finding a parton with momentum fraction x. Examples of some experimentally determined PDFs are shown in Fig. 1.16. These PDFs indicate that the distribution of up and down valence quarks peak at $x \approx 1/3$, however, due to quark-gluon interactions, they are not delta functions, and some momentum is carried by other quarks (so-called "sea-quarks") and gluons.

The key limitation of PDFs to be addressed in this thesis is that they do not convey dynamic properties of the nucleon, such as the transition from a neutron to a proton (or vice versa) by emission of a pion. This limitation is addressed by the study of Generalized Parton Distributions (GPDs), as discussed in Secion 2.2.

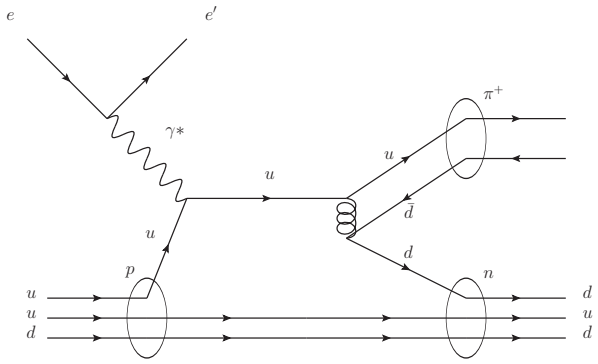

Figure 1.12: Leading order Feynman diagram for production of a positive pion via interaction with a proton. The white blobs indicate higher order processes binding the incoming and outgoing hadrons together.

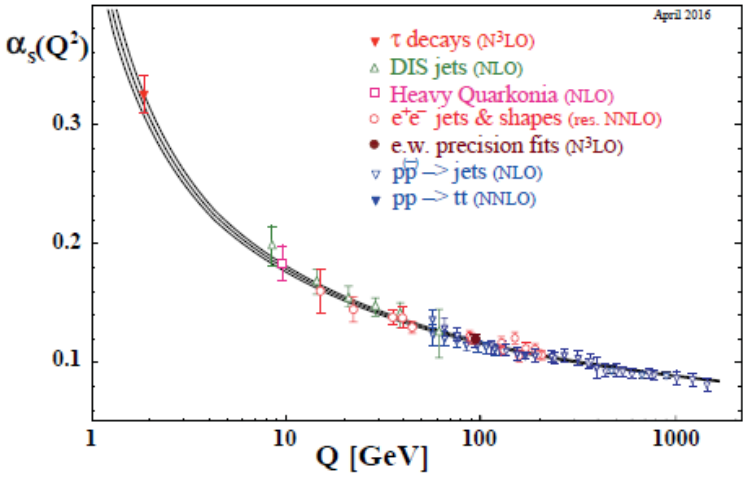

Figure 1.13: Strong coupling constant, α_s, as a function of energy scale Q [12]

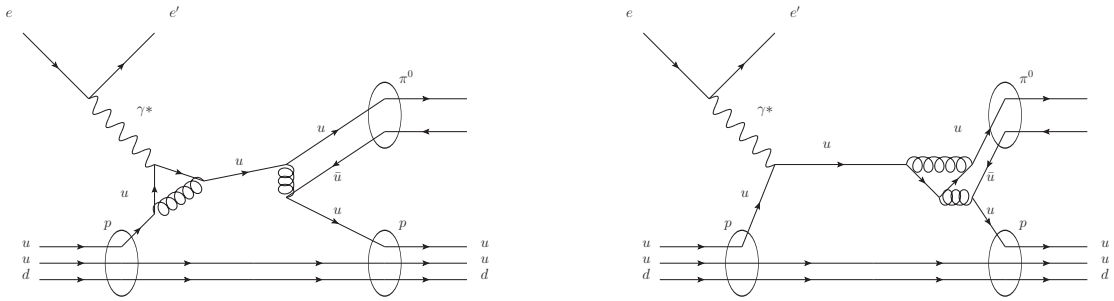

Figure 1.14: Feynman diagrams showing possible gluon vertex corrections to the $p \to p\pi^0$ reaction as shown in Fig. 1.11.

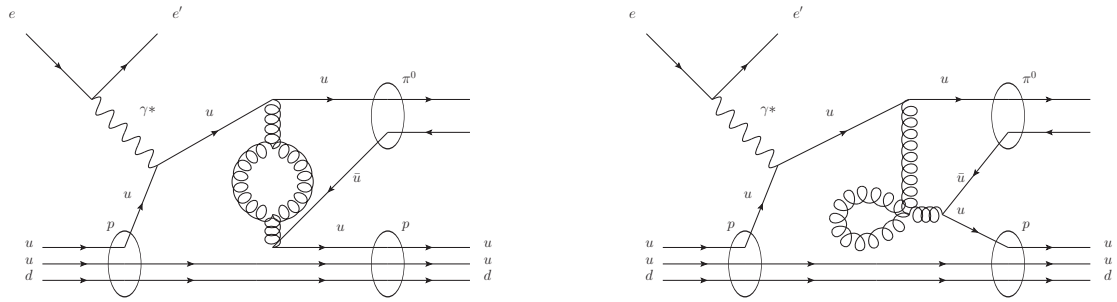

(a) Three gluon vertex.

(b) Four gluon vertex

Figure 1.15: Feynman diagrams showing some possible higher order corrections to the $p \to p\pi^0$ reaction (as in Fig. 1.11) due to gluon self-interactions.

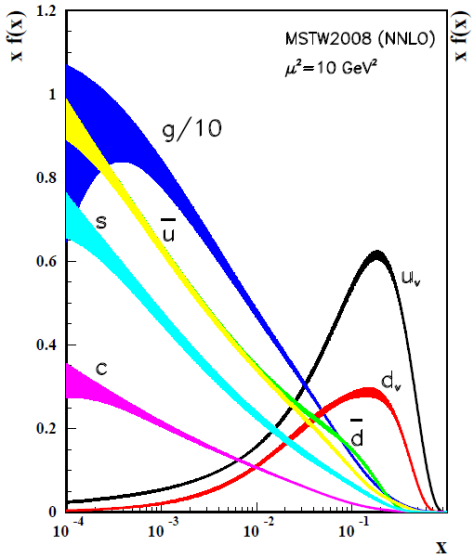

Figure 1.16: Parton distributions for different quark flavors and gluons, as a function of the Bjorken x. The width of the bands indicates the uncertainty [12]. These correspond to the momentum distribution of these constituents as a function of fractional momentum x.

Chapter 2

Deep Exclusive Meson Production (DEMP)

This chapter is based on the run-group proposal titled "Measurement of Deep Exclusive π^- Production using a Transversely Polarized ^{3}He Target and the SoLID Spectrometer" [5]. This proposal is to extract measurements of the transverse nucleon, single-spin asymmetries, $A_{UT}(\phi, \phi_s)$, in offline analysis of the SIDIS E12-10-006 experiment [2]. There are as many as six azimuthal modulations, $A_{UT}^{sin(\mu\phi+\lambda\phi_s)}$, contributing to the cross section of the $\vec{n}(e, e'\pi^-)p$ reaction. The largest two, $A_{UT}^{\sin(\phi-\phi_S)}$ and $A_{UT}^{\sin(\phi_s)}$, are of particular value in the study of Generalized Parton Distributions (GPDs), in particular, the spin-flip GPD $\tilde{E}$.

2.1 Unpolarized Deep Exclusive Meson Production

The reaction of primary interest in this thesis is $\vec{n}(e, e'\pi^-)p$, that is, scattering of an electron off of a polarized neutron, producing a negatively charged pion, and causing the impacted nucleon to recoil as a proton. As a foundation for the study of this reaction, the simpler case of the same reaction on an unpolarized neutron, $n(e, e'\pi^-)p$ must be discussed.

Fig. 2.1 shows the Feynman cartoon for the unpolarized reaction, along with definitions for the coordinate frame. For convenience we define a set of Lorentz invariant parameters called the Mandelstam variables. The invariant Mandelstam variables may be defined as follows for this reaction, and are useful in formulation

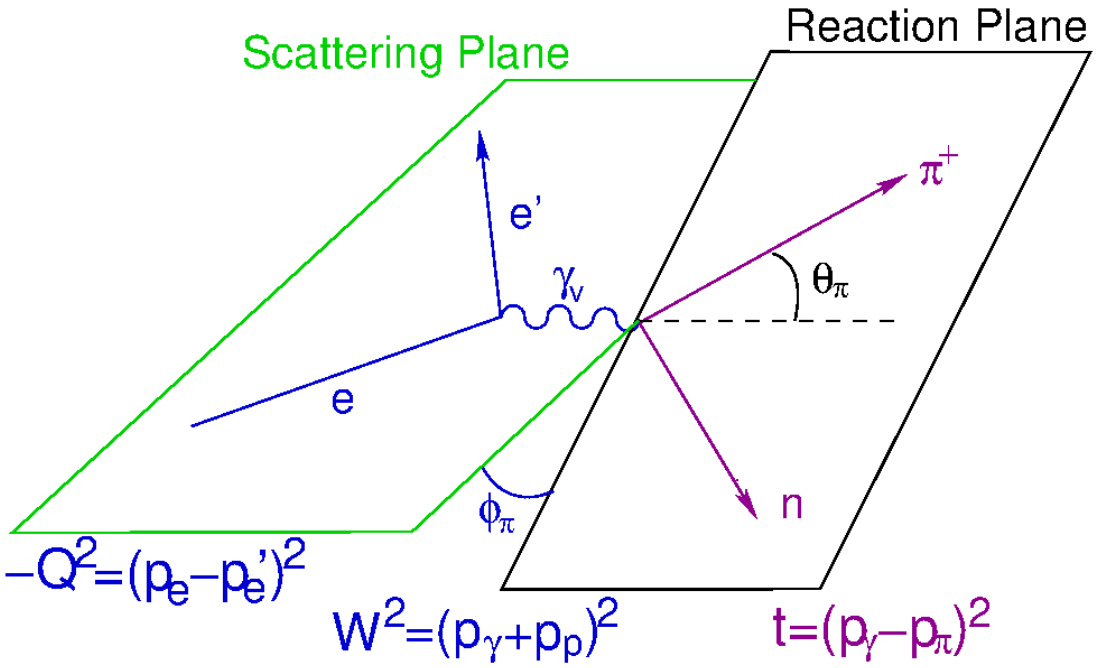

Figure 2.1: Feynman cartoon for unpolarized positive pion production, $n(e,e'\pi^-)p$, with definition of coordinate frame.

of the cross section:

$$s = (p_n + q)^2 = (p_p + p_{\pi^-})^2, \tag{2.1}$$

$$t = (p_n - p_p)^2 = (q - p_{\pi^-})^2, \tag{2.2}$$

$$u = (p_n - p_{\pi^-})^2 = (q - p_p)^2. \tag{2.3}$$

q, p_n, p_p, and p_{π^-} are the four-momenta of the virtual photon, target neutron, recoiled proton, and produced pion, respectively. In addition, the quantity Q^2 is useful, and is defined as

$$Q^2 = -q^2 = -(p_e - p_{e'})^2, \tag{2.4}$$

as before (Equation 1.3). The invariant mass of the photon-target system, $W = \sqrt{s}$ (Equation 1.5), is also useful. It is worth noting here that t is always negative, and, for a constant Q^2 and W, has a minimum (least negative) value, $t_{\min}$, which occurs in fully parallel kinematics (i.e. $\theta = 0^\circ$ or 180°).

In the single-photon approximation, the unpolarized cross section may be expressed as the sum of four

terms:

$$d\sigma_{UU} = \epsilon \frac{d\sigma_{\mathrm{L}}}{dt} + \frac{d\sigma_{\mathrm{T}}}{dt} + \sqrt{2\epsilon(\epsilon+1)} \frac{d\sigma_{\mathrm{LT}}}{dt} \cos\phi + \epsilon \frac{d\sigma_{\mathrm{TT}}}{dt} \cos 2\phi. \tag{2.5}$$

The first two terms correspond the the longitudinal (L) and transverse (T) polarization states of the virtual photon respectively. The latter two terms correspond to longitudinal-transverse (LT) and transverse-transverse (TT) interference of polarization states. ϵ is the polarization of the virtual photon:

$$\epsilon = \left(1 + \frac{2|\vec{q}|^2}{Q^2} \tan^2 \frac{\theta_e}{2}\right)^{-1}, \tag{2.6}$$

where $\epsilon = 0$ corresponds to transverse photons only, and $\epsilon = 1$ corresponds to equal fluxes of transverse and longitudinal photons. ϕ is the angle between the scattering plane and the reaction plane, as shown in Fig. 2.1, and θ_e is the polar angle of the scattered electron.

2.1.1 Parameterization of σ_{UU}

The unpolarized cross section, $d\sigma_{UU}$, shorthanded as σ_{UU}, and its components are parameterized from the phenomenological Vrancx-Ryckebusch (VR) model [13]. Model data are generated in the kinematic region of Q^2 from 4.0 to 7.5 GeV^2, $-t$ from $-t_{\min}$ to -1.0 GeV^2, and at $W = 3.0$ GeV [13] [14] [15]. The W dependence is then taken as $(W^2 - M_p^2)^{-2}$, where M_p is the proton mass [16].

These data were parameterized by Zafar Ahmed to fit the following functions [17]:

$$\sigma_L = \exp\left(P_1(Q^2) + |t| * P_1'(Q^2)\right) + \exp\left(P_2(Q^2) + |t| * P_2'(Q^2)\right), \tag{2.7}$$

$$\sigma_T = \frac{\exp\left(P_1(Q^2) + |t| * P_1'(Q^2)\right)}{P_1(|t|)}, \tag{2.8}$$

$$\sigma_{LT} = P_5(t(Q^2)), \tag{2.9}$$

$$\sigma_{TT} = P_5(t(Q^2)). \tag{2.10}$$

Each parameter, P_i is a polynomial function of i^{th} order.

Implementation of the parameterization and its use in the Monte-Carlo simulation is discussed in Section 4.3.1.

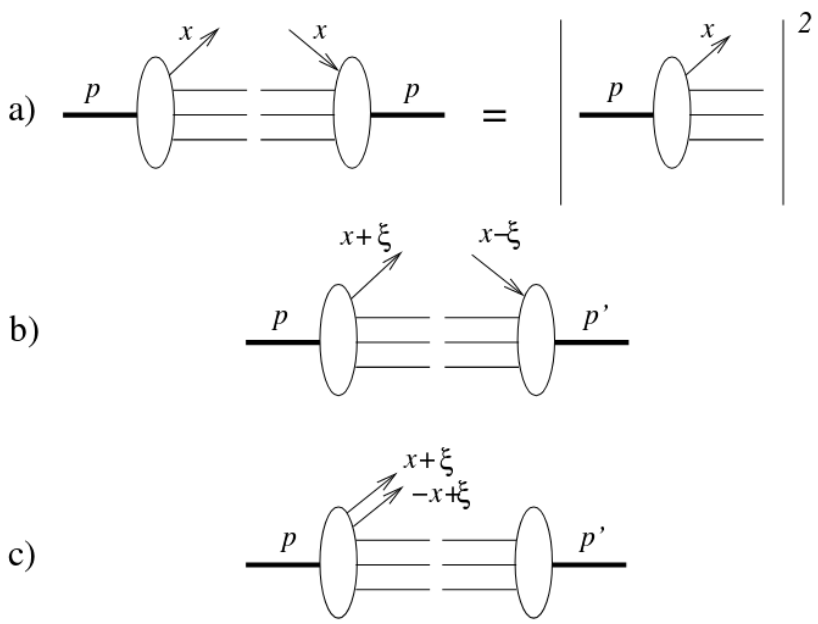

Figure 2.2: (a) PDF represented as the probability of finding a parton with momentum x in the hadron with momentum p. (b) GPD represented as the emission of a parton with momentum fraction $x + \xi$ and reabsorption at $x - \xi$. (c) GPD in the kinematic region of the emission of a quark-antiquark pair. [5]

2.2 Generalized Parton Distributions (GPDs)

GPDs in principle encode all information about not only the internal structure of hadrons, but also dynamic properties of the system, correlating different parton configurations. They are independent of the reaction used to probe them. In terms of quark and gluon wavefunctions of the hadron, the PDFs discussed in Section 1.4 and shown in Fig. 1.16 are obtained theoretically from the square of the wavefunction representing the probability of finding a parton with momentum fraction x (Fig. 2.2a). GPDs, on the other hand, are obtained from the interference of different wavefunctions with different momentum fractions, $x+\xi$ and $x-\xi$ (Fig. 2.2b). DEMP probes a special kinematic regime where the initial hadron emits a quark-antiquark pair (meson) or gluon pair (Fig. 2.2c).

In addition to x and ξ, the GPDs depend on the four momentum transfer t.

At leading order, the nucleon structure can be parameterized into four GPDs labeled E, H, $\tilde{E}$ and $\tilde{H}$. All four of these GPDs conserve quark chirality. H and $\tilde{H}$ conserve the helicity (the projection of spin onto momentum) of the nucleon, while E and $\tilde{E}$ allow for it to be flipped. H and E are summed over quark helicity, while $\tilde{H}$ and $\tilde{E}$ involve the difference between left- and right-handed quarks.

These four, leading-order, GPDs are linked most significantly to other nucleon structure quantities as

follows [18]:

$$\sum_q e_q \int_{-1}^{+1} dx H^q(x,\xi,t) = F_1(t), \tag{2.11}$$

$$\sum_q e_q \int_{-1}^{+1} dx E^q(x,\xi,t) = F_2(t), \tag{2.12}$$

$$\sum_q e_q \int_{-1}^{+1} dx \tilde{H}^q(x,\xi,t) = G_A(t), \tag{2.13}$$

$$\sum_q e_q \int_{-1}^{+1} dx \tilde{E}^q(x,\xi,t) = G_P(t), \tag{2.14}$$

where e_q is the charge of the relevant quark. $F_1(t)$ and $F_2(t)$ are electromagnetic nucleon form factors, and are well known from elastic scattering experiments. $G_A(t)$ and $G_P(t)$, on the other hand, are less well known weak form factors. In particular, $G_P(t)$ is only experimentally accessible from beta decay, which occurs only at very low momentum transfer.

As such, $\tilde{E}$ is the currently least well known of the leading order GPDs. At high momentum transfer, the observable most sensitive to this GPD is the single-spin asymmetry for exclusive charged pion production from a polarized nucleon target ($\vec{p}(e,e'\pi^+)n$ or $\vec{n}(e,e'\pi^-)p$), $A_L^\perp$. It is connected to the interference between and $\tilde{H}$ and $\tilde{E}$ by:

$$A_L^\perp = \frac{\sqrt{-t'}}{m_p} \frac{\xi\sqrt{1-\xi^2}\ \mathrm{Im}(\tilde{E}^*\tilde{H})}{(1-\xi^2)\tilde{H}^2 - \frac{t\xi^2}{4m_p}\tilde{E}^2 - 2\xi^2 \mathrm{Re}(\tilde{E}^*\tilde{H})}, \tag{2.15}$$

where t is the four momentum transfer onto the nucleon. This variable is defined as:

$$A_L^\perp = (\int_0^\pi d\beta \frac{d\sigma_L^\pi}{d\beta} - \int_\pi^{2\pi} d\beta \frac{d\sigma_L^\pi}{d\beta})(\int_0^{2\pi} d\beta \frac{d\sigma_L^\pi}{d\beta})^{-1}. \tag{2.16}$$

The cross section here, $d\sigma_L^\pi$, is for exclusive charged pion electroproduction using longitudinally polarized virtual photons. β is the angle between the nucleon polarization vector and the reaction plane, as shown in Fig. 2.3.

Frankfurt et al. [19] suggest that precocious scaling in this variable as a function of Q^2 may be expected in the range of $Q^2 \approx 2-4$ GeV [19], but scaling for the absolute cross section is not expected until $Q^2 > 10$ GeV. This range for Q^2 makes measurement of this asymmetry accessible at JLab.

The reaction of interest is then:

$$\vec{n} + e \rightarrow e' + \pi^- + p \tag{2.17}$$

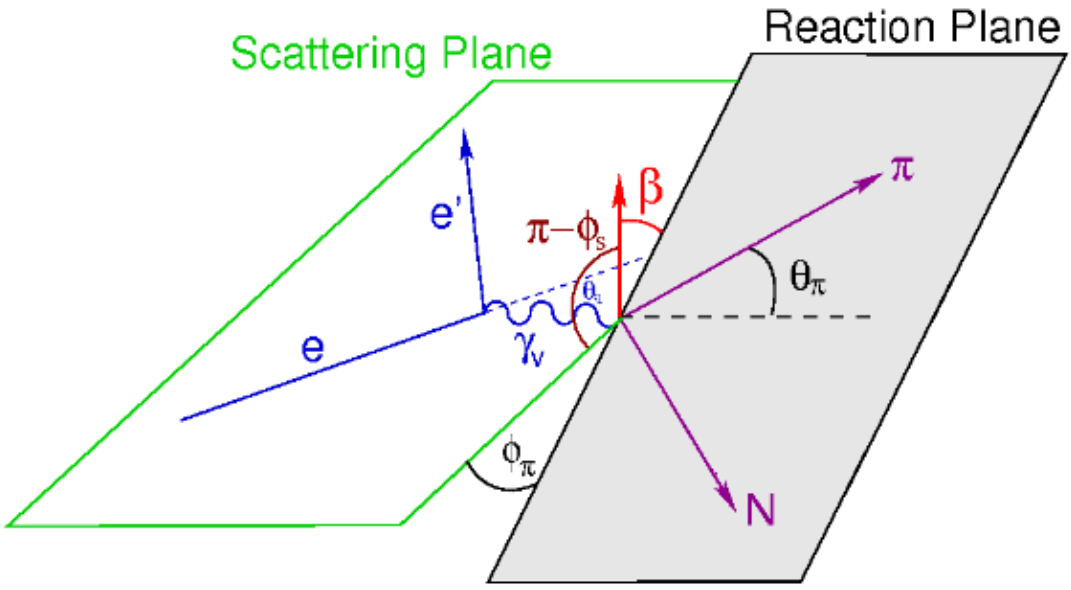

Figure 2.3: Coordinate system for the DEMP experiment in the target rest frame. ϕ is the azimuthal angle between the reaction plane and scattering plane. θ_q is the angle of the virtual photon relative to the trajectory of the incident electron. ϕ_s is the azimuthal angle between the nucleon polarization and the scattering plane. $\beta = \phi - \phi_s$ is the azimuthal angle between the nucleon polarization and the reaction plane.

or simply $\vec{n}(e, e'\pi^-)p$. Fig. 2.4 shows the "Handbag" Feynman cartoon for the reaction. This cartoon indicates the factorization between hard scattering (described well by pQCD) and soft scattering processes, which was first shown possible in DEMP by Collins et. al. [20]. S. V. Goloskokov and P. Kroll have built a phenomenological model (henceforth, the GK model) following this Handbag approach [21][22]. Data from the DEMP experiment will provide a comparison for this model. Predictions for the $\sin(\beta)$ modulation are shown in Fig. 2.5 and compared against previous data from HERMES [23].

The cross section for the $\vec{n}(e, e'\pi^-)p$ reaction is:

$$d\sigma = d\sigma_{UU} + d\sigma_{UT} \tag{2.18}$$

where $d\sigma_{uu}$ is the unpolarized cross section, as discussed in Section 2.1, and $d\sigma_{UT}$ is the additional contri-

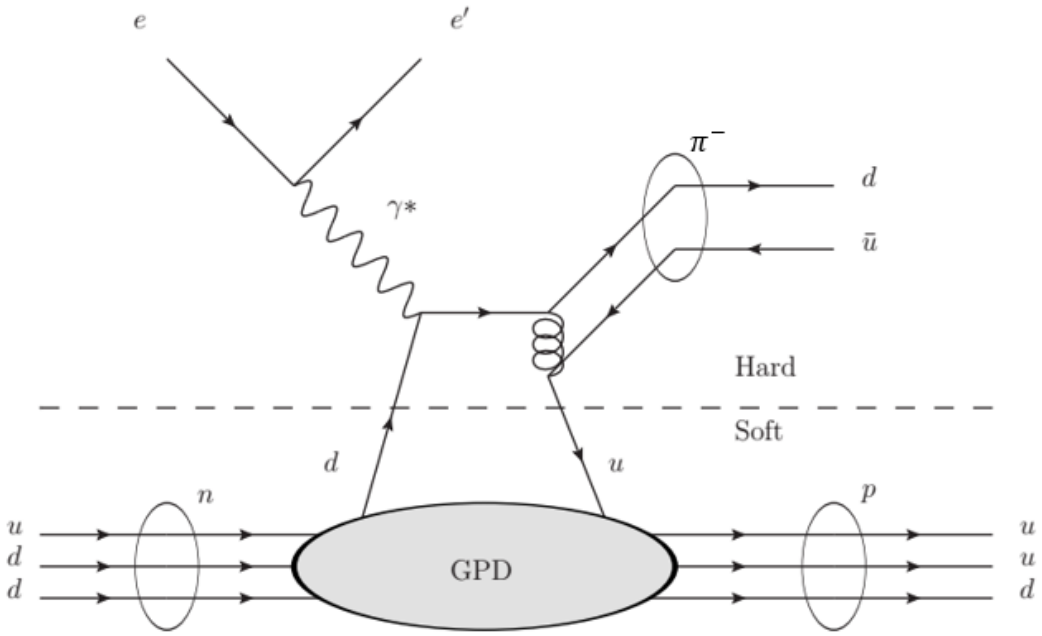

Figure 2.4: Feynman cartoon showing the handbag approach for $\vec{n}(e, e'\pi^-)p$ reaction in the DEMP experiment. The gray blob, concealing higher order processes, is described by the GPD. The dashed line indicates the factorization between hard and soft scattering components of the interaction.

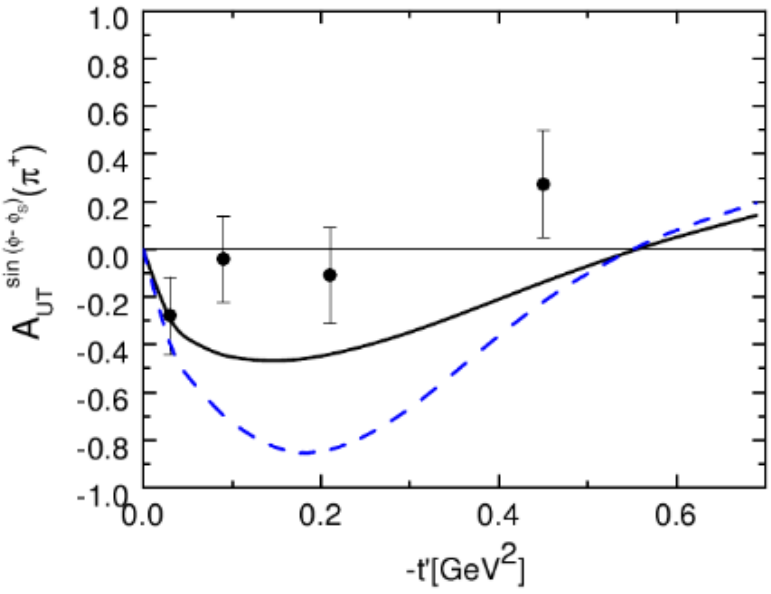

Figure 2.5: Predictions by Goloskokov and Kroll for the $\sin\beta$ moment of the azimuthal asymmetry vs. $t' = t - t_{\min}$. The data points are from HERMES [23]. The dashed line is the contribution only from longitudinally polarized photons, while the solid line includes contributions from transversely polarized photons.

bution when the target nucleon is transversely polarized. $d\sigma_{UT}$, can be expressed [23][24] as:

$$\begin{aligned} d\sigma_{UT}(\phi,\phi_s) = \sum_k d\sigma_{UT_k}(\phi,\phi_s) \; = -\frac{P_\perp \cos\theta_q}{\sqrt{1-\sin^2\theta_q \sin^2\phi_s}} \Big[\; & \sin\beta \; \mathrm{Im}(\sigma_{++}^{+-} + \epsilon\sigma_{00}^{+-}) \\ & + \; \sin\phi_s \; \sqrt{\epsilon(1+\epsilon)} \; \mathrm{Im}(\sigma_{+0}^{+-}) \\ & + \; \sin(\phi+\phi_s) \; \frac{\epsilon}{2} \; \mathrm{Im}(\sigma_{+-}^{+-}) \\ & + \; \sin(2\phi-\phi_s) \; \sqrt{\epsilon(1+\epsilon)} \; \mathrm{Im}(\sigma_{+0}^{-+}) \\ & + \; \sin(3\phi-\phi_s) \; \frac{\epsilon}{2} \; \mathrm{Im}(\sigma_{+-}^{-+}) \; \Big], \end{aligned} \tag{2.19}$$

where $P_\perp$ is the magnitude of the transverse polarization of the target. Definitions for angles ϕ, ϕ_s, and θ_q are given in Fig. 2.3. Note that this formulation is based on the Trento Conventions [25], which dictate definitions for the coordinate axes such that the virtual photon momentum is along the z-axis, and the x-axis lies in the scattering plane. The σ_{mn}^{ij} are cross sections corresponding to different nucleon polarizations, $ij = (+\frac{1}{2}, -\frac{1}{2})$, and photon polarizations, $mn = (+1, 0, -1)$. The cross section $\epsilon\sigma_{00}^{+-}$ then corresponds to $d\sigma_L^\pi/d\beta$ in equation 2.15, but it shares an azimuthal dependence with the σ_{++}^{+-} cross section, due to transversely polarized photons. While each of the other cross sections can be separated based on their azimuthal dependencies, separation of the two $\sin(\beta)$ dependent cross sections requires a Rosenbluth-type separation, which may not be possible with the available experimental apparatus. However, as indicated by Fig. 2.5, the GK model has considered the contribution of transverse photons, leaving extraction of the combined $\sin(\beta)$ modulation a valuable point of comparison nonetheless.

Equation 2.19 may be written more practically in terms of the unpolarized cross section σ_{UU} and the azimuthal asymmetry amplitudes $A_{UT}^{sin(\mu\phi+\lambda\phi_s)_k}$ as follows [23]:

$$\Sigma_k = d\sigma_{UU}(\phi) A_{UT}^{\sin(\mu\phi+\lambda\phi_s)_k} \tag{2.20}$$

$$d\sigma_{UT} = -\frac{P_T}{\sqrt{1-\sin^2\theta\sin^2\phi_s}} \sum_{k=1}^{6} \sin(\mu\phi+\lambda\phi_s)_k \Sigma_k. \tag{2.21}$$

where P_T is now the component of the target polarization perpendicular to the virtual photon, and the modulations are given by:

k	$\sin(\mu\phi + \lambda\phi_s)$
1	$\sin(\phi - \phi_s)$
2	$\sin(\phi + \phi_s)$
3	$\sin(\phi_s)$
4	$\sin(2\phi - \phi_s)$
5	$\sin(3\phi - \phi_s)$
6	$\sin(2\phi + \phi_s)$

The unpolarized cross section, σ_{UU}, is parameterized separately, as discussed in Section 2.1.

The above takes an interaction with a polarized neutron as granted. However, a pure polarized neutron target does not exist in practice. The DEMP experiment will use a polarized ^{3}He target (discussed in Section 3.3) as a good approximation. This leads to dilution by unpolarized interactions, which will be discussed in Section 4.3.3.

2.3 Parameterization of Azimuthal Modulations

S. V. Goloskokov and P. Kroll have provided model data for the $k = 1-5$ asymmetry amplitudes [26]. These data are at discrete values of Q^2 from 4.107 to 7.167 GeV^2, W from 2.362 to 3.191 GeV, and $t' = t - t_{\min}$ from 0 to 0.5 GeV^2. t is the momentum transfer $t = (q - p_{\pi^-})^2$ (where q and p_{π^-} are the four momenta of the virtual photon and produced pion, respectively) and $t_{\min}$ is the minimum value of t for a constant Q^2 and W. The raw GK model data are shown in Fig. 2.6. The sixth asymmetry amplitude is expected to be much smaller and is taken to be zero.

The fit functions were initially chosen only to closely match the shape of the model data, and were not based on any physical principle. They are as follows:

$$A_{UT}^{\sin(\mu\phi+\lambda\phi_s)_k} = \begin{cases} ae^{bt'} - (a+c)e^{dt'} + c, & k = 1 \\ ae^{bt'} + c, & k = 2,3,4,5 \end{cases} \tag{2.22}$$

where a, b, c, and d are fit parameters. These fits are done independently for each Q^2, W pair. The parameterized functions are displayed alongside the model data in Fig. 2.6. The $k = 1$ fit function originally had an additional, independent parameter in place of $(a + c)$, but the fit did not converge reliably. As such, it was constrained to pass through the origin, justified by the requirement that all asymmetries dependent

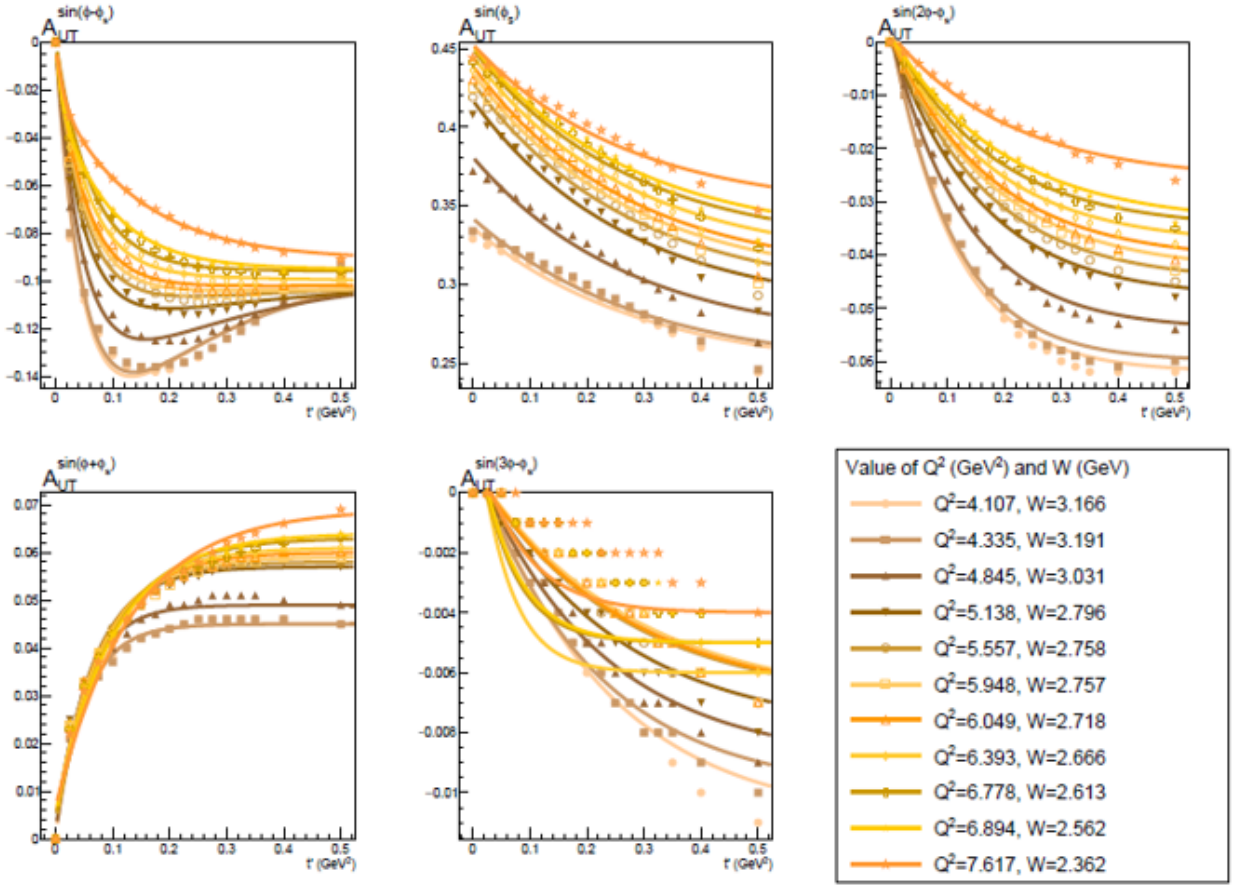

Figure 2.6: Asymmetry amplitudes vs t' for different values of Q^2 and W. Data points are the raw model data provided by Goloskokov and Kroll [26]. The lines are the parameterized fit for each Q^2, W pair.

on ϕ must vanish at $t = t_{\min}$, as ϕ is undefined in parallel kinematics. This also applies to all but the $k = 3$ asymmetry, however, the fits were satisfactory, and the additional constraint was not deemed necessary.

The main physics goal of the DEMP experiment is to measure the $k = 1$ asymmetry amplitude, $A_{UT}^{\sin(\phi-\phi_s)}$. In addition, the $k = 3$ asymmetry amplitude, $A_{UT}^{\sin(\phi_s)}$, may also be accessible through this experiment, and gives information on higher order GPDs. The DEMP experiment was proposed to run on the already approved SoLID apparatus (Chapter 3).

Chapter 3

SoLID Experimental Program

In this chapter, the apparatus used for the DEMP experiment, and how this provides the required data, is discussed.

3.1 Thomas Jefferson National Accelerator Facility

The Thomas Jefferson National Accelerator Facility (JLab) is a nuclear physics research laboratory in Newport News, Virginia. The main facility is the Continuous Electron Beam Accelerator Facility (CEBAF), a pair of 1400 m long linear accelerators, connected as a "racetrack" by two curving arcs. The primary benefit CEBAF provides over typical circular accelerators is the nearly continuous beam current.

Originally, CEBAF was able to deliver electrons of up to 6 GeV to three experiment halls, A, B, and C, simultaneously, with the electrons traversing the linear accelerators five times. The 12 GeV upgrade, completed as of December 2017, brought this up to 11 GeV for the existing experiment halls, and added another experiment hall, D, at the other end of the facility, capable of receiving up to 12 GeV electrons after they make another pass through just one of the accelerators. Fig. 3.1 shows CEBAF and the experiment halls from above, with the locations of the halls and linear accelerators indicated. Fig. 3.2 shows a schematic of the facility.

The Solenoidal Large Intensity Device (SoLID) is an upcoming fixed angle detector to be built in JLab's Expermiental Hall A. It is designed to be a high-acceptance, high-luminosity, and high-rate detector, intended to take fullmost advantage of the JLab 12 GeV upgrade.

The SoLID experimental program covers many different physics experiments. The three main categories

Figure 3.1: Aerial photograph of the CEBAF facility at JLab, with approximate locations of the underground experiment halls and linear accelerators marked [27].

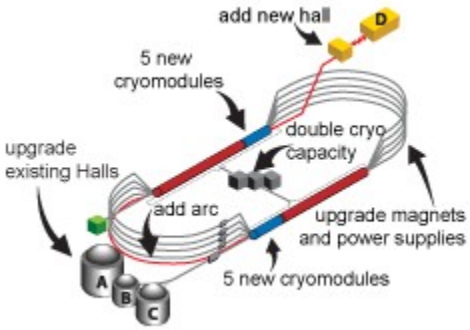

Figure 3.2: Schematic diagram of the 12 GeV upgrades to JLab's CEBAF and experiment halls [27].

of experiment for which SoLID has been designed are as follows:

- SIDIS: Semi-Inclusive Deep Inelastic Scattering
- J/Ψ
- PVDIS: Parity Violating Deep Inelastic Scattering

3.2 SIDIS Program with SoLID

The SIDIS Program with SoLID consists of three of SoLID's flagship experiments. These experiments all concern charged pion production, but each with different target configurations: Transversely Polarized ^{3}He Target (E12-10-006) [2], Longitudinally Polarized ^{3}He Target (E12-11-007) [3], and Transversely Polarized Proton Target (E12-11-108) [4]. The E12-10-006 experiment will operate with the following parameters [2]:

- A transversely polarized ^{3}He target.
- Identification of electrons and charged pions.
- Polar angle coverage for electrons from 8° to 24°.
- Polar angle coverage for pions from 8° to 16°.
- 0° to 360° azimuthal coverage.
- Momentum coverage of > 0.8 GeV/c for electrons and pions.
- $e^- + \pi^\pm$ double coincidence trigger.

These parameters suit the requirements for the DEMP experiment, as discussed in Chapter 2. The only additional key requirement is identification of the recoiled proton. While the SIDIS experiment has no need for proton detection, the recoiled proton is expected to create an identifiable signal in SoLID's Gas Elecxtron Multiplier (GEM) detectors (section 3.4.1). As such, the DEMP experiment has been approved as experiment E12-10-006B [5], running parasitically with E12-10-006. DEMP data will be obtained by offline analysis of SIDIS data, searching for $e^- + \pi^- + p$ triple coincidence events.

3.3 SoLID Polarized ^{3}He Cryogenic Target

Both the E12-10-006 and DEMP experiments concern interactions with a stationary, polarized, neutron target. However, free neutrons are unstable particles with a mean halflife of 614 s [12], and so no such target exists. As such, a polarized cryogenic ^{3}He target is used. The ^{3}He nucleus contains one neutron and two protons, however the spins of the two protons are anti-aligned, and so their wavefunctions, in a sense, cancel each other out. Polarized ^{3}He, then, makes for an excellent approximation for a polarized neutron target. Several studies have calculated the effective neutron polarization of ^{3}He to be 86.5% [28][29][30][31].

The SoLID ^{3}He target consists of a 40-cm-long target cell, polarized using three sets of Helmholtz coils, each consisting of a pair of axially aligned magnetic coils. The coils provide a 25 Gauss field, in multiple directions, allowing for transverse and longitudinal polarization. E12-10-006 and DEMP use the transverse configuration.

The polarization is periodically reversed (in previous experiments, every 20 minutes) to minimize systematic uncertainties. This contributes slightly to loss in polarization, leading to maximum in-beam polarization of approximately 60% [1].

3.4 The SoLID Detector

The information in this section is based primarily upon the SoLID Preliminary Conceptual Design Report [1].

SoLID is a proposed large-acceptance, high-intensity spectrometer to be built in JLab's Hall A. The detector has two different configurations based on the running experiment: The SIDIS configuration and the PVDIS configuration. The SIDIS configuration is of main interest, as this is, naturally, what is used for the SIDIS experiments (section 3.2), and consequently also for DEMP. The SIDIS configuration utilizes the following key components:

- CLEO II Solenoidal Magnet.
- Gas Electron Multiplier (GEM) tracking detector.
- Light Gas Cherenkov detector (LGC).
- Heavy Gas Cherenkov detector (HGC).
- Multi-Gap Resistive Plate Chamber detector (MRPC).

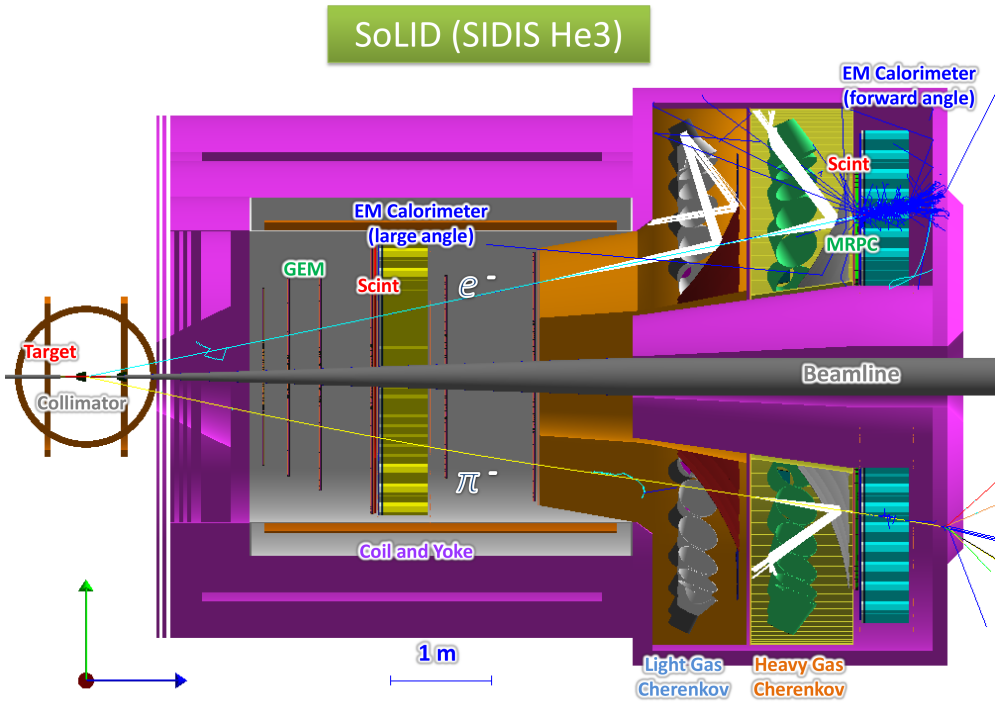

Figure 3.3: SoLID SIDIS configuration design overview [1]

- Electromagnetic Calorimeter.

These will be discussed in further detail in the following sections.

The SIDIS configuration uses the Hall A polarized ^{3}He target, and takes full advantage of the JLab 12-GeV-beam. The detectors are mounted around the beam line providing 2π azimuthal coverage, making the detector perfect for asymmetry studies. In total, the spectrometer covers polar angles from $8-24^\circ$ with a resolution of 0.6 milli-radians, and a momentum range of 0.8-7.0 GeV/c^2 with a resolution of approximately 2% full width at half maximum.

3.4.1 GEM Detectors and CLEO II

GEM trackers fulfill the high-resolution, high-rate, and large-area requirements for track reconstruction in SoLID. These relatively new detectors operate on gas avalanche multiplication confined to small ($\sim$100 µm) holes in several thin foil layers [32]. The high voltage applied between the GEM foils allows for large amplifications. SoLID will make use of multiple trapezoidal GEM chambers each with three foils. Fig. 3.4 shows a cross-sectional diagram of a GEM chamber.

The SIDIS configuration will have six GEM detectors, each having a wheel of 20 chambers, as shown in

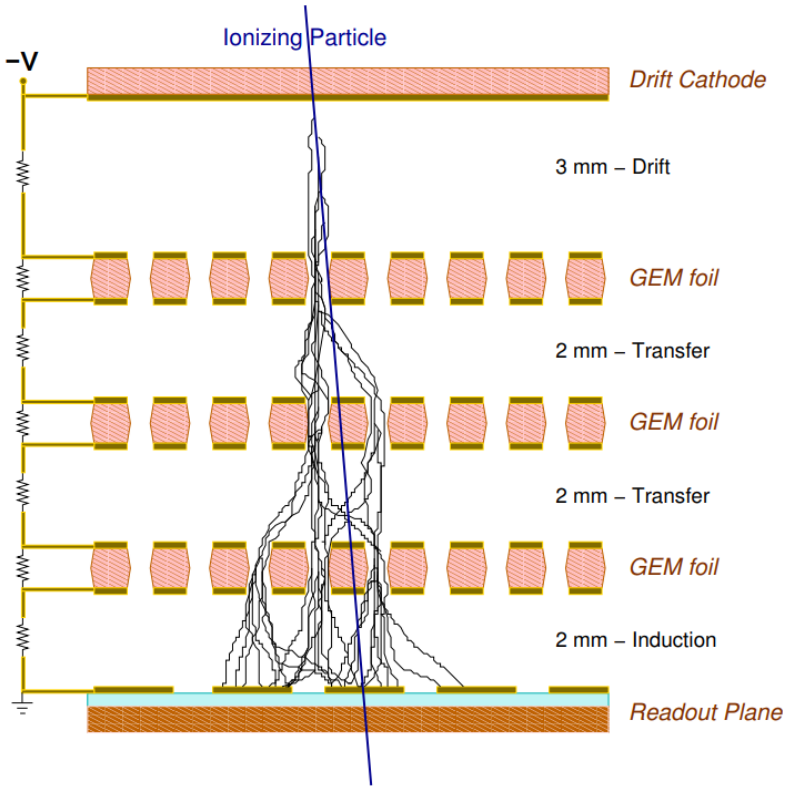

Figure 3.4: Principle of GEM operation [1].

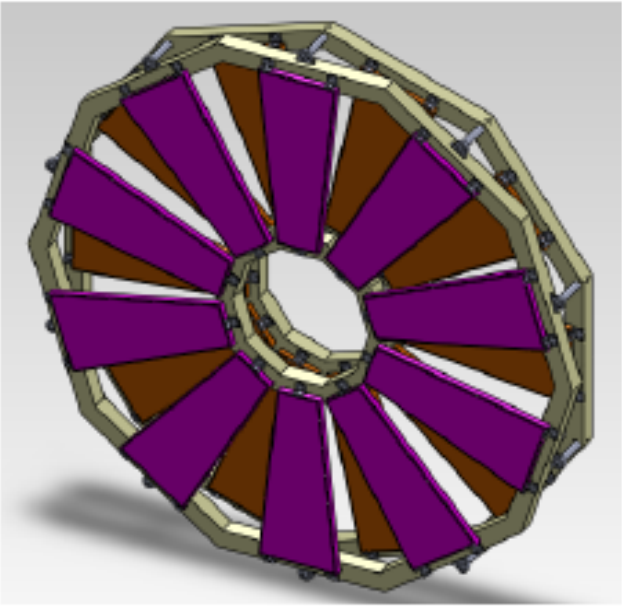

Figure 3.5: Design of GEM detector plane in SIDIS configuration. SoLID will contain six of these [1].

Fig. 3.5. These chambers provide a 2D readout for particle tracking with a resolution of 70 µm, and can handle a count rate of up to 100 MHz/cm^2.

The GEMs are housed inside a 1.5 T solenoidal magnet. The magnet was originally built for the CLEO-II experiment and has been acquired for use on SoLID. The purpose of the CLEO II magnet (in SIDIS) is to allow the GEMs to measure the momentum and charge sign, based on the curvature of the particle's ionization track. A positively (negatively) charged particle will travel in a counterclockwise (clockwise) helix around the beam axis. These data are also then used to determine the vertex angles of the reaction.

There are a total of six GEM planes inside the solenoid. The first four are upstream from the LAEC (section 3.4.5) used for both large and forward angle measurements, while the latter two, downstream from the LAEC, are forward angle only.

3.4.2 Light Gas Cherenkov Detector (LGC)

The LGC will be placed after the GEM detectors to discriminate scattered electrons from produced pions. The LGC will also be used in the PVDIS configurations and so is designed with 30 sectors due to PVDIS requirements. In the SIDIS configuration, the LGC will be filled with CO_2 at 1 atm pressure, with a refractive index of 1.0004. Each sector has two spherical mirrors reflecting the Cherenkov light into a Light collecting (Winston) cone. For each cone there is a 3 x 3 array of photomultiplier tubes (PMTs). The design of the

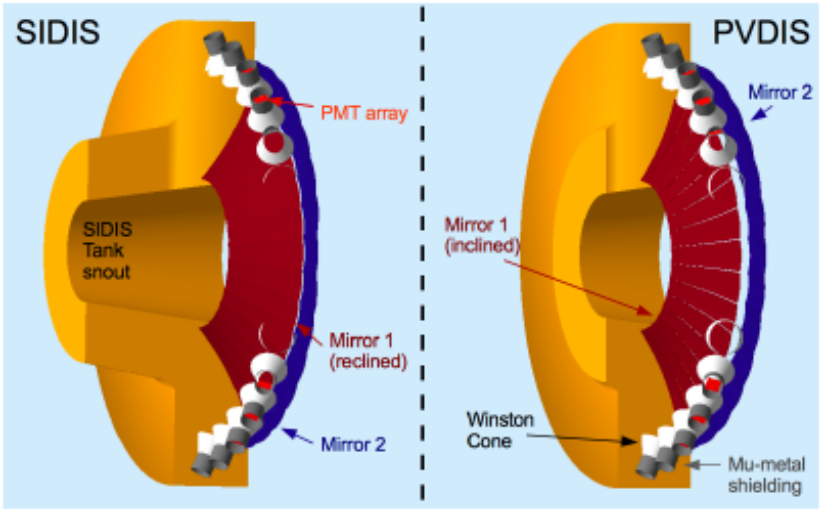

Figure 3.6: Design of LGC detector for SIDIS and PVDIS configurations [1].

LGC is shown in Fig. 3.6.

The PMTs that will be employed are Hamamatsu flat panel multianode photomultiplier tube assemblies [33], which each have an 8 x 8 pixel array. These pixels will be wired together for one signal per PMT, thus nine signals per sector. The trigger will require that at least two PMTs in the same array produce coincident signals, resulting in 36 possible coincidences for each sector. This configuration has shown an overall $> 90\%$ average electron detection efficiency in simulations.

3.4.3 Heavy Gas Cherenkov Detector (HGC)

The SoLID Heavy Gas Cherenkovdetector (HGC) is one of the primary subjects of this thesis. The University of Regina has acquired funding from CFI and Fedoruk Institute to build a prototype segment of this detector. The prototyping process is discussed in greater detail in Chapter 5.

The HGC will be placed after the LGC and provides hadron identification. The detector will be filled with C_4F_8O gas at 1.5 atm absolute pressure. This provides an index of refraction of 1.002, giving a momentum threshold 2.2 GeV/c for pions, and 7.5 GeV/c for kaons, allowing separation of protons and kaons from pions at momenta greater than 2.5 GeV/c.

The HGC is only present in the SIDIS configuration, and so is not bound to the geometry of PVDIS components, as in the case of the LGC. The HGC will be broken into 10 sectors, each with three spherical mirrors, and three light collecting cones and PMT arrays, similar to the design of the LGC. Fig. 3.7 shows the HGC as it appears in the SoLID Preliminary Conceptual Design Report [1].

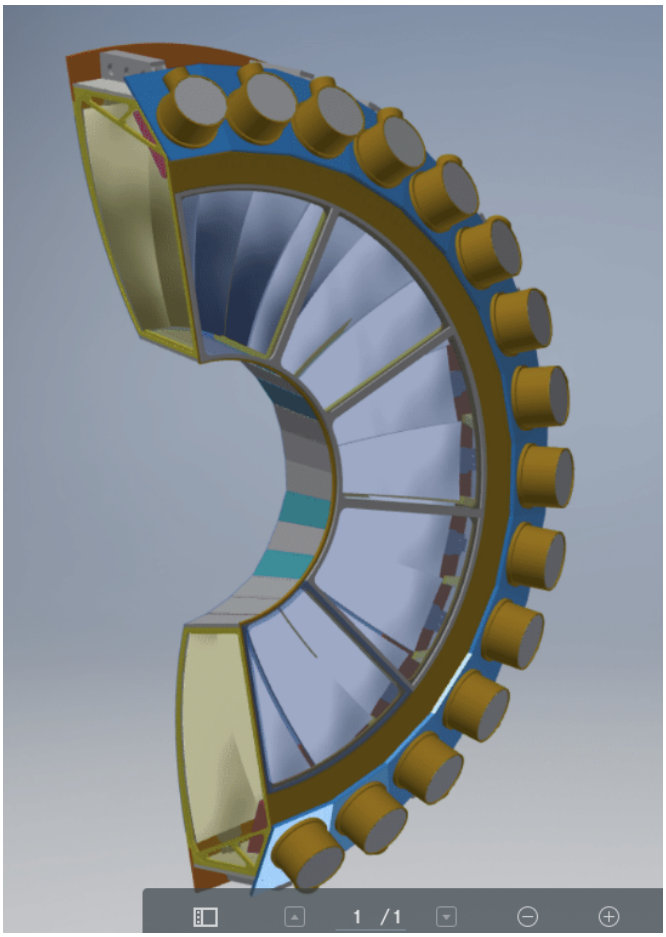

Figure 3.7: CAD image of right hand half (looking downstream) of the HGC. Drawn by Gary Swift [34]. The diameter of the detector is approximately 5.6 m tall.

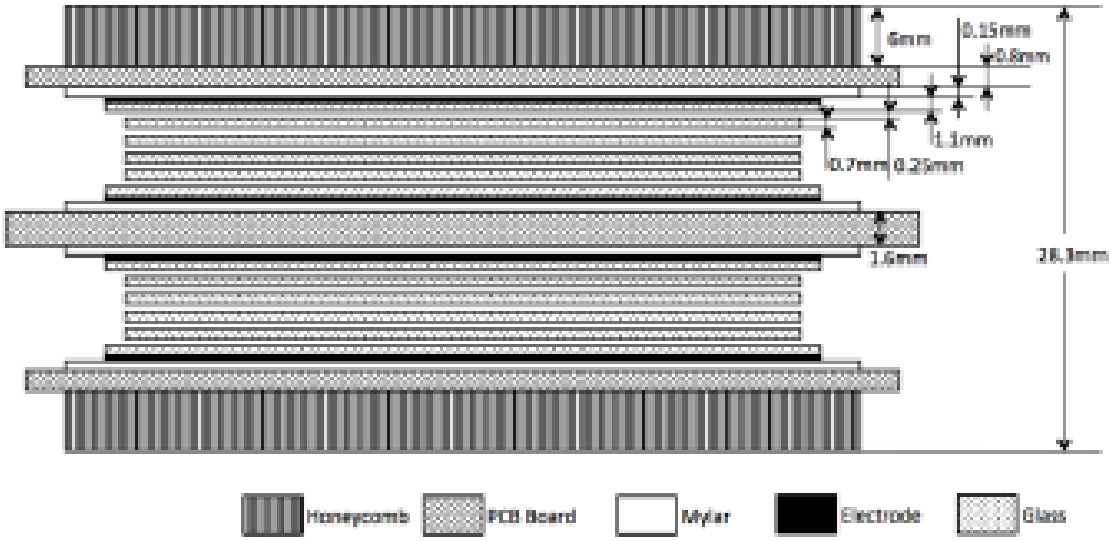

Figure 3.8: Design of MPRC detector plane in SIDIS configuration [1].

3.4.4 Multi-Gap Resistive Plate Chamber (MRPC) detector

The MRPC is another gas avalanche based detector, to be placed behind the HGC. This detector will provide time-of-flight (TOF) information, at a resolution of ∼100 ps, and pion identification at less than 2.5 GeV/c. Fig. 3.8 shows the structure of the MRPC.

3.4.5 Electromagnetic Calorimeter (EC)

The SIDIS configuration includes two electromagnetic calorimeters (ECs) of the same basic design, but with differing acceptances and purposes. The PVDIS configuration also requires an EC, but with significantly different geometries. In order to both meet the physics requirements, and to share as much hardware between configurations as possible, a highly modular design was chosen.

The ECs will consist of hexagonal "Shashlyk" modules with a 100 cm^2 cross-sectional area. The concept behind the Shashlyk design of calorimeter is alternating layers of scintillator and absorber. The layers are stacked longitudinally, while the individual modules will be stacked laterally to build the full ECs.

The modules are also divided longitudinally into pre-shower and shower detectors. The pre-shower consists of $2X_0 = 11.2$ mm (X_0 is the radiation length) of passive radiator (lead), followed by 2 cm of plastic scintillator. Each layer in the shower detector consists of 0.5 mm lead, 1.5 mm plastic scintillator, and two

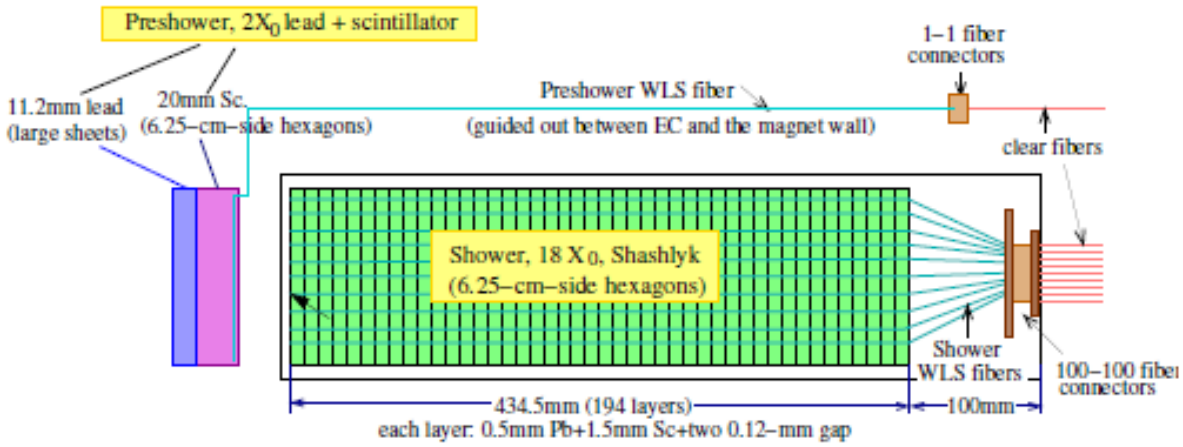

Figure 3.9: Design of electromagnetic calorimeter modules to be used in SoLID [1].

sheets of highly reflective, 0.12 mm paper. The reflective paper separates each lead and scintillator plate, reducing the loss of scintillation light. The shower detector consists of 194 such layers in total, for a length of $18X_0 = 43.3$ cm. The Moliere radius (radius of a cylinder containing 90% of the shower energy) is 5 cm. Fig. 3.9 shows the schematic for one of the EC modules.

Light is collected by wavelength shifting fibers which penetrate through all the layers in the EC modules. This, combined with timing information, also allows for longitudinal sampling, allowing for reconstruction of the entire shower profile. They also have scintillator pad detectors (SPDs) in front of them to reject photons.

The first EC in the stack is the Large Angle Electromagnetic Calorimeter (LAEC). The LAEC is placed between GEMs 4 and 5 and covers polar angles between 16.3 and 24°. The second, forward angle EC (FAEC) is placed at the end of the stack.

Chapter 4

Event Generator

The DEMP event generator was originally developed by Zafar Ahmed to simulate DEMP events with a range of kinematics slightly larger than the acceptance of the SoLID detector [5] [17]. It includes parameterizations of various cross section components, asymmetries, and the calculation of the total cross section. Also included are independently toggle-able corrections for the Fermi momentum of the ^{3}He target, and the passage of particles through matter (ionization, energy loss, bremsstrahlung, multiple scattering), and $\pi - N$ Final State Interaction (FSI).

The work of this M.Sc. project included the parameterization of the asymmetries and their implementation along with multiple scattering, into the event generator. More significantly, this M.Sc. project also included an almost complete rewrite of Ahmed's original code. The first goal of this rewrite was to produce cleaner and more organized code, with more thorough documentation, appropriate for a potential journal publication. The second goal was to improve the computational efficiency of the event generator, to allow for greater statistics with shorter computation time, allowing certain physics studies which were not practical with the original generator. The third goal was to act as an error check on the original generator. By comparing intermediate results and calculations, a second, independent approach should expose any bugs or miscalculations which may impact the final results. The updated event generator can be found, along with the original, on github at `https://github.com/RoryEvansPhysics/DEMP-EvGen`.

4.1 Design

Upon review of the original event generator code, several issues and sources of inefficiency were identified. The bulk of the code was contained in a single .cpp file which was executed using the live C++ interpreter (CINT) which comes withthe ROOT software package developed by the European Organization for Nuclear Research (CERN) [35]. This presents a few issues. The C++ language was not designed as an interpreted language, rather, it is generally intended to be compiled before runtime. Use of the interpreter limits the breadth of C++ libraries and tools to those recognized by the interpreter. It also severely undermines the computation speed. Most code takes a certain amount of time to compile (compilation time) and to compute (computation time). In comparison, the interpreted code will have no compilation time, but the computation time will be, at minimum, equal to the sum of both the compilation time and computation time of compiled code. This is a significant disadvantage when performing multiple runs of the code on different settings, as the code must effectively recompile for each run. Non-interpreted code may run repeatedly after compiling only once. The interpreter also created problems in troubleshooting. If errors exist after computationally heavy parts of the code, this code must run before identifying the error. In compiled code, the error may be identified immediately at compilation time.

These considerations lead to the first guiding principle in the design of the new event generator: The code must fully compile separately from runtime, and be reconfigured without recompiling. CMake was chosen as a convenient tool to configure compilation including ROOT libraries, due to ROOT's native support. The code is compiled using GNU Compiler Collection (GCC). To configure parameters for a run, JsonCpp [36] was chosen to facilitate reading a JSON configuration file during runtime.

Other issues are created by the structure of the original code. The main file is nearly 2000 lines long, making it difficult to read and navigate. It also sources a large list of variables declared in a separate file, many of which have extremely similar purposes. For example, each momentum component, for each particle, for each reference frame, before and after various corrections, are all stored in separate named variables. This large list of variables adds to the clutter and repetition in the code, making it more challenging to understand. Both of these issues can be tackled using an object oriented approach. Use of object oriented programming will allow repetitive code and variable declarations to be consolidated into a small number of flexible object classes.

Fig. 4.1 demonstrates the flow of data in the event generator, starting from random number generators, leading to the output file. The rounded boxes in this chart each indicate the main named variables whose values are pointers to instances of the indicated class. For example, "VertTargNeut" is a pointer to an object

of class "Particle". These variables, the classes, and their place in the structure of the event generator are discussed in the following subsections.

4.1.1 Particle Class

Instances of the particle class contain all of the pieces of information about a single particle, in a single frame of reference, that are relevant to the event generator. This includes the four-momentum, rest mass, charge, etc. The particle inherits from ROOT's TLorentzVector class, which allows for the creation and manipulation of general four-vectors. The TLorentzVector class includes methods to calculate components, angles, and magnitudes of a four-momentum, as well as perform Lorentz boosts and rotations. It also defines algebraic operators for four-vectors. Implementation of this class significantly simplifies calculations within the event generator, and eliminates a large number of messy algorithms that were present in the original event generator.

4.1.2 DEMPEvent class

Instances of the DEMPEvent class represent the event viewed from a single reference frame. The class stores seven particle objects: The incident electron, target neutron, virtual photon, scattered electron, produced pion, and recoiled proton. The class has methods to calculate Mandelstam variables (equations 2.1, 2.2, and 2.3), and functions to perform coordinate transformations on the event. There are five DEMPEvent objects initialized in the event generator, as seen in Fig. 4.1. VertEvent contains the particles as viewed at the vertex of the interaction, in the laboratory rest frame. Once the kinematics calculations have been completed (see Section 4.2), this object is no longer modified. All other DEMPEvent objects are calculated from this object by copying and then transforming them. CofMEvent is the event viewed at the vertex in the center of momentum reference frame. RestEvent is the event viewed at the vertex in the rest frame of the target neutron. TConEvent is the event viewed at the vertex in the coordinate system defined by the Trento Conventions [25].

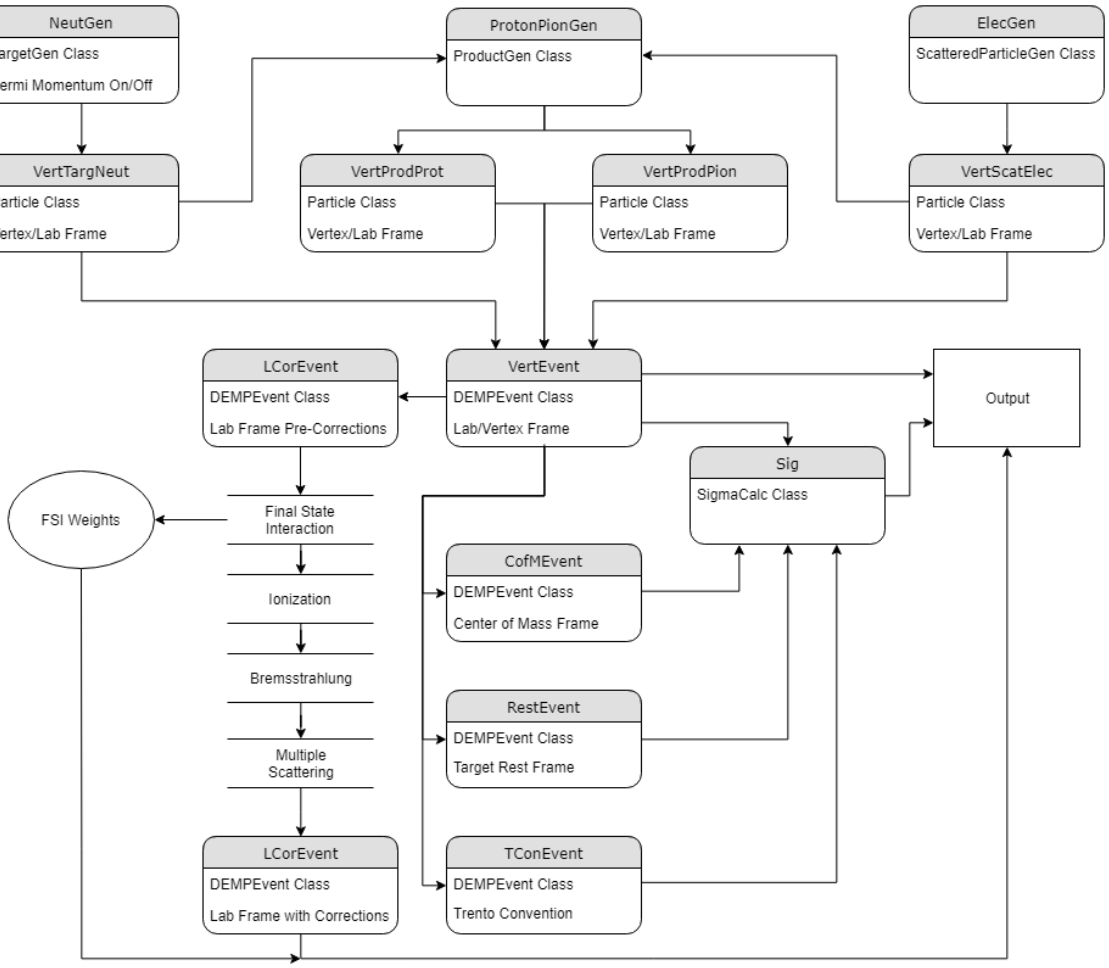

Figure 4.1: Flowchart describing the flow of data through the program, and the structure of the event generator. The rounded boxes signify the most important named variables that appear in the main file of the program. Their values are pointers to an instance of the given class. Arrows indicate how data is moved between these objects. The four open boxes indicate static functions. The "FSI Weights" node represents a simple collection of doubles. The "Output" box represents destination for data to be saved into the output ROOT tree.

4.2 Kinematics

Calculation of particle kinematics begins with random generation of the energy and momentum of the target neutron, as described in Section 4.7.3, if Fermi momentum is enabled. If Fermi momentum is not enabled, it is set to zero, with energy equal to the neutron rest mass. Next, the energy of the scattered electron is selected from a uniform random distribution in a configurable range (typically 0.1 to 0.9 times the energy of the incident beam). The direction of the scattered electron is selected using sphere point picking [37], with a configurable limit on the range θ. The azimuthal angle (ϕ) may be selected from a uniform distribution from 0 to 2π, but selecting the polar angle (θ) uniformly results in bunching near $\theta = 0$. The distribution function for the polar angle is instead $\frac{1}{2}\sin^2(\theta)$. The direction for the produced pion is then selected, again using sphere point picking, with a configurable θ range. The energy of the pion is left to be solved for.

These variables provide all information necessary to uniquely solve for the rest of the kinematic variables. Conservation of four-momentum at the $e \to e'\gamma$ vertex gives the four momentum of the virtual photon:

$$\gamma = e - e'. \tag{4.1}$$

At the $\gamma n \to p\pi$ vertex, conservation of energy gives:

$$\gamma^0 + n^0 = p^0 + \pi^0 \tag{4.2}$$

where γ^0, n^0, p^0, and π^0 represent the 0^{th} component (energy) of the respective particle's four-momentum. Applying the energy-momentum relation then yields:

$$\gamma^0 + n^0 = \sqrt{m_p^2 + |\vec{p}|^2} + \sqrt{m_\pi^2 + |\vec{\pi}|^2} \tag{4.3}$$

where the vectors represent the three-momenta of their respective particles. Finally, conservation of momentum at the $\gamma n - p\pi$ vertex allows the substitution $\vec{p} = \vec{\gamma} + \vec{n} - \vec{\pi}$, yielding the following equation:

$$\gamma^0 + n^0 - \sqrt{m_\pi^2 + |\vec{\pi}|^2} - \sqrt{m_p^2 + |\vec{\gamma} + \vec{n} - \vec{\pi}|^2} = 0, \tag{4.4}$$

The only unknown in this equation is the momentum vector of the pion. Since the direction of the pion has already been specified, Equation 4.4 may be further reduced to a single-valued unknown: the momentum magnitude of the pion. The left hand side of the equation is defined in the event generator as a function of

$|\vec{\pi}|$ in a ROOT TF1 (1-Dim function) object. The TF1 object incorporates a root finding algorithm, using Brent's method [35], which is used to find values for $|\vec{\pi}|$ which solve Equation 4.4. If more than one solution is found, one is picked at random.

The original event generator solved for the pion momentum by simply iterating over the full range of possible values, until the value of the invariant mass, W, differed by less than 1 MeV, between the initial and final state. As such, the use of Brent's method permits a greater degree of accuracy, as well as saving computation time.

The energy and momentum of the recoil proton can then be calculated by a straightforward application of conservation of four-momentum. The following checks are then made to verify thatthe solution is within acceptable limits: The rest mass of the proton is calculated from the solution and compared against the known value, the value of W for the initial state is compared to the final state, and total energy and momentum for the initial state is compared to final state. If any value deviates by more than 1 MeV(/c), or a solution is not found, the event is discarded. In testing over several million events, all events with solutions passed these checks, however, approximately a third of events did not have a solution and were discarded.

4.3 Cross Sections and Weight

Because the events are generated uniformly over the phase space, calculation of the cross section is required to weight each event according to their probability.

4.3.1 Parameterization of $d\sigma_{UU}$

As discussed in Section 2.1.1, the components of σ_{UU} were parameterized by Zafar Ahmed according to Equations 2.7 to 2.10 using VR model data [13] [14]. The results of this parameterization were hard-coded into functions for use in the original event generator. These functions are incorporated into the new event generator and accessed by the SigmaCalc class.

4.3.2 Asymmetries and $d\sigma_{UT}$

Parameterization of the asymmetries is discussed Section 2.3. The parameters are saved to a file and read at runtime into instances of the Asymmetry class. Each Asymmetry object corresponds to one of the five asymmetries and contains each of the parameterized functions for that asymmetry, one for each Q^2, W pair. The Asymmetry class implements a function to retrieve the asymmetry amplitude given Q^2 and t'

as arguments. The value is calculated by selecting the two functions with the associated values of Q^2 closest to the input. These two functions are each evaluated at the input t' value, resulting in two data points, (Q_1^2, A_1) and (Q_2^2, A_2). A line is then drawn between these two points to interpolate a value for the asymmetry amplitude at the input Q^2 value.

The asymmetries are accessed by the SigmaCalc class and used to calculate the cross section component σ_{UT} according to Equation 2.21.

4.3.3 σ and Event Weight

The cross section components σ_{UU} and σ_{UT} are summed to give the overall cross section σ, as shown by Equation 2.18. Explicitly, this cross section is a two-fold differential scattering cross section in the center of mass frame. In order to calculate the event weight, the five-fold differential cross section in the lab frame is needed. This is calculated as follows [5]

$$d^5\sigma = \frac{d^5\sigma}{dE' d\Omega_{e'} d\Omega_\pi} = \Gamma_V J \frac{d^2\sigma}{dt d\phi} \tag{4.5}$$

where J is the Jacobian transformation from the center of mass frame to the lab frame. Γ_V is the virtual photon flux factor, defined as [5]:

$$\Gamma_V = \frac{\alpha}{2\pi} \frac{E'}{E} \frac{(W^2 - M_n^2)}{2M_n Q^2} \frac{1}{1-\epsilon}, \tag{4.6}$$

where α is the fine structure constant, W is the invariant mass of the final state, and ϵ is the virtual photon polarization, as given by Equation 2.6.

The event weight is then given by the following expression:

$$w = \frac{d^2\sigma}{d\Omega_\pi} \frac{(\text{phase-space-factor})(\text{luminosity})(\text{target-factors})}{N_{gen}} \tag{4.7}$$

The phase-space-factor is the fraction of the total kinematically accessible phase space that is covered by the event generator. The luminosity for the SIDIS experiment is 10^{36} cm^{-2}s^{-1} [1]. The target-factors include the 60% target polarization and the 85.6% effective polarized neutron discussed in section 3.3. N_{gen} is the total number of generated events, including those that were discarded due to either falling outside of acceptable parameters, or having no valid solutions in the kinematics solver.

4.4 Phase Space and Acceptance

The current studies with the event generator are run using the following configuration:

- Beam energy: 11 GeV.
- Scattered electron energy: 1.1 to 9.9 GeV.
- Scattered electron θ: 5° to 27°.
- Pion θ: 6° to 18°.

In addition, any events meeting the following criteria are discarded due to being outside the accurate range for the cross section model:

- $t < -1.2\,\mathrm{GeV}^2$
- $Q^2 < 4\,\mathrm{GeV}^2$
- $W < 2\,\mathrm{GeV}^2$

Fig. 4.2 shows the weighted momentum and polar angle distribution of particles generated in this configuration. Fig. 4.3 shows the weighted Q^2 and t distribution.

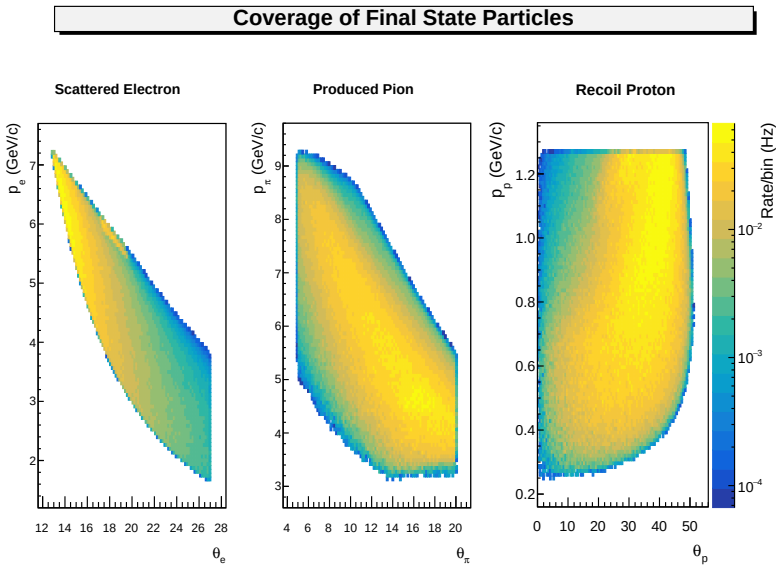

Figure 4.2: Weighted kinematic coverage of the three final state particles produced by the DEMP event generator. The color axis represents the rate for each bin.

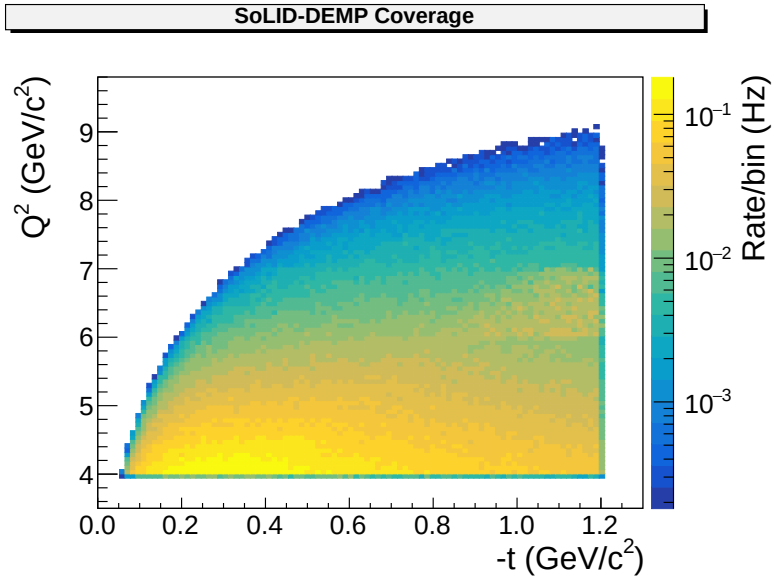

Figure 4.3: Weighted kinematic coverage of the invariant values Q^2 and t produced by the DEMP event generator. The color axis represents the rate for each bin.

Preliminary simulations of the SoLID apparatus have been performed using the GEMC Monte-Carlo simulation [1], providing detector acceptance as an additional factor to the event weight [38]. The detector resolution may also be incorporated by "smearing" the data with small randomly generated adjustments. The adjustments have a Gaussian distribution with widths of 2% for energy/momentum, 0.6 mrad for polar angles, and 5 mrad for azimuthal angle [38]. From this, along with the proposed beam time of 48 days [5] [2], a simulated experimental yield may be calculated:

$$N = w \times (\text{acceptance with resolution}) \times (\text{time}) \tag{4.8}$$

Figs. 4.4 and 4.5 display the same distribution of events as Figs. 4.2 and 4.3 respectively, but with the inclusion of these additional factors. These figures represent the total expected acceptance for the DEMP experiment. Note the absence of events between 14.5°and 16°, where there is a dead-zone between large-angle and forward-angle in the detector.

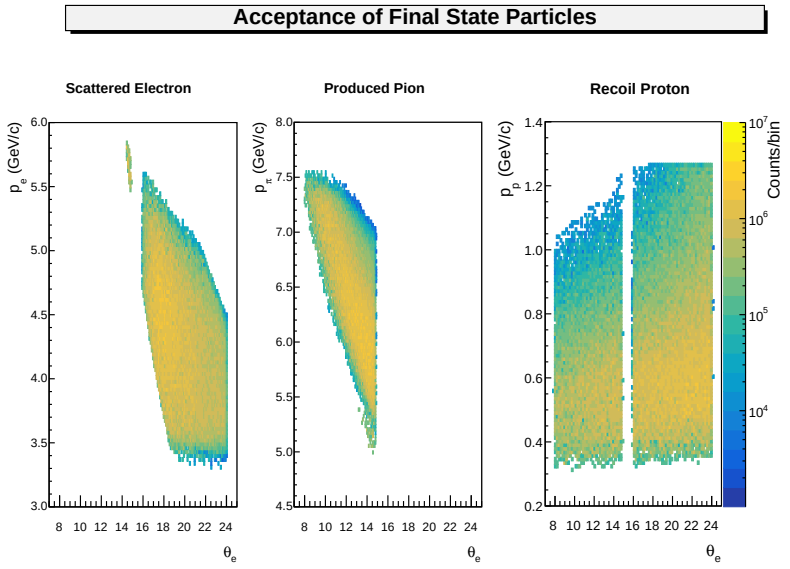

Figure 4.4: Weighted acceptance of the three final state particles produced by the DEMP event generator and measured by SoLID. The color axis represents the expected yield of DEMP events in the SIDIS experiment.

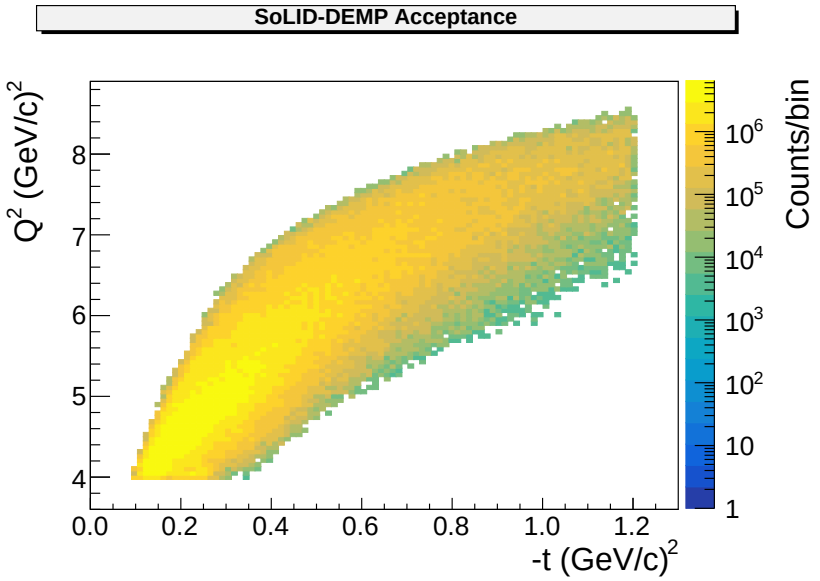

Figure 4.5: Weighted acceptance of events produced by the DEMP event generator and measured by SoLID, in terms of invariant quantities Q^2 and t. The color axis represents the expected yield of DEMP events in the SIDIS experiment.

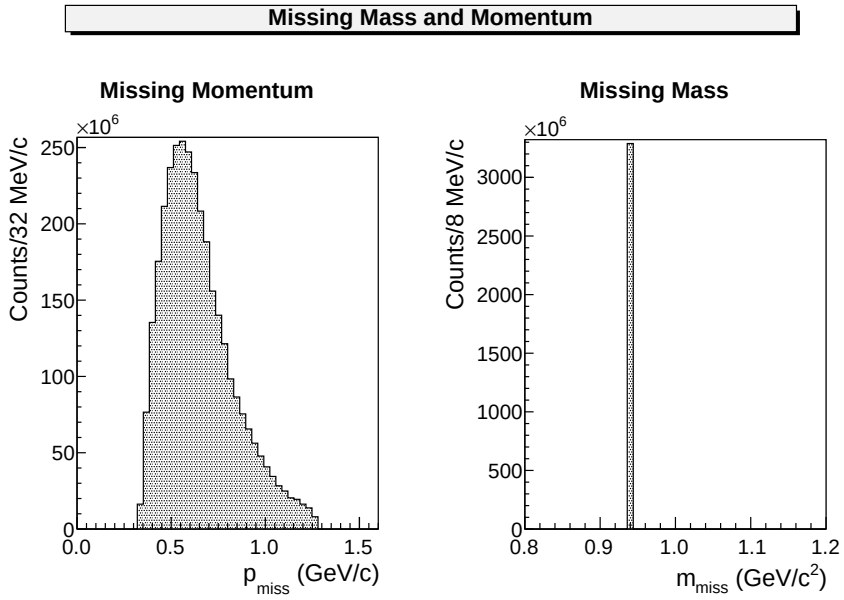

Figure 4.6: Missing mass and momentum distribution with no corrective effects enabled.

4.5 Missing Mass and Momentum

Depending on the quality of data on the recoiled proton provided by SoLID, missing mass and momentum cuts may be necessary in analysis of the data. The missing momentum is also useful in identifying events which have undergone final state interaction (Section 4.7.4). The missing mass and momentum are defined in DEMP as follows:

$$\vec{p}_{miss} = \vec{p}_{beam} - \vec{p}_{e'} - \vec{p}_{\pi} \tag{4.9}$$

$$E_{miss} = E_{beam} + m_n - E_{e'} - E_{\pi} \tag{4.10}$$

$$m^2_{miss} = E^2_{miss} - p^2_{miss} \tag{4.11}$$

$$m^2_{miss} = (E_{beam} + m_n - E_{e'} - E_{\pi})^2 - |\vec{p}_{beam} - \vec{p}_{e'} - \vec{p}_{\pi}|^2 \tag{4.12}$$

The missing mass and momentum distributions produced by the event generator with no corrective effects enabled are shown in Fig. 4.6. Unsurprisingly, in this configuration the missing mass is always equal to the proton mass within computational precision error.

4.6 Likelihood Analysis

In order to extract the five asymmetry components from the measured asymmetry, a 2-dimensional, 5-parameter fit is required. This is accomplished using an unbinned maximum likelihood (UML) method, written by Zhihong Ye [5][38], adapted to the new event generator output. A typical maximum likelihood analysis would require binning in both ϕ and ϕ_S as well as in t. The UML analysis is performed with only t binning.

The extracted values for the asymmetry amplitudes are found from the minimization of the log-likelihood function [23]

$$-\ln L(\theta_k) = -\sum_{i=1}^{N^+} \ln f_+(\phi, \phi_S; \theta_k) - \sum_{i=1}^{N^-} \ln f_-(\phi, \phi_S; \theta_k), \tag{4.13}$$

where

$$f_\pm(\phi, \phi_S; \theta_k) = \frac{1}{C_\pm}\left[1 \pm |P_T| \sum_{k=1}^{6} \theta_k \sin(\mu\phi + \lambda\phi_S)_k\right]. \tag{4.14}$$

$C_\pm$ is a normalization factor, and is taken to be $C_\pm = 1$. f_+ (f_-) corresponds to data taken in the down (up) target polarization configuration, with N_+ (N_-) recorded events. θ_k are the free parameters in the fit, and provide the asymmetry amplitudes simply by:

$$\theta_k = A_{UT}^{\sin(\mu\phi+\lambda\phi_s)_k}. \tag{4.15}$$

The minimization is performed using the ROOT implementation of MINUIT [35]. For this work, the generated data are split into 7 t bins (with roughly equivalent statistics) with the following bounds:

$$-t = [0.05, 0.20, 0.30, 0.40, 0.50, 0.70, 1.0, 3.0], \tag{4.16}$$

as in the DEMP proposal [5]. The results of the UML analysis with no corrective effects enabled are shown in Fig. 4.7. Note that uncertainties are present, but represent only fitting uncertainty, and are here too small to see. The fits for the asymmetries of interest, $\phi - \phi_s$ and ϕ_s, as well as the $2\phi - \phi_s$ and $3\phi - \phi_s$ show good agreement with the input value, especially at high $-t$ values, where the physics of interest lies. Only the $\phi + \phi_s$ asymmetry fits poorly, but this asymmetry is of less significance to this study.

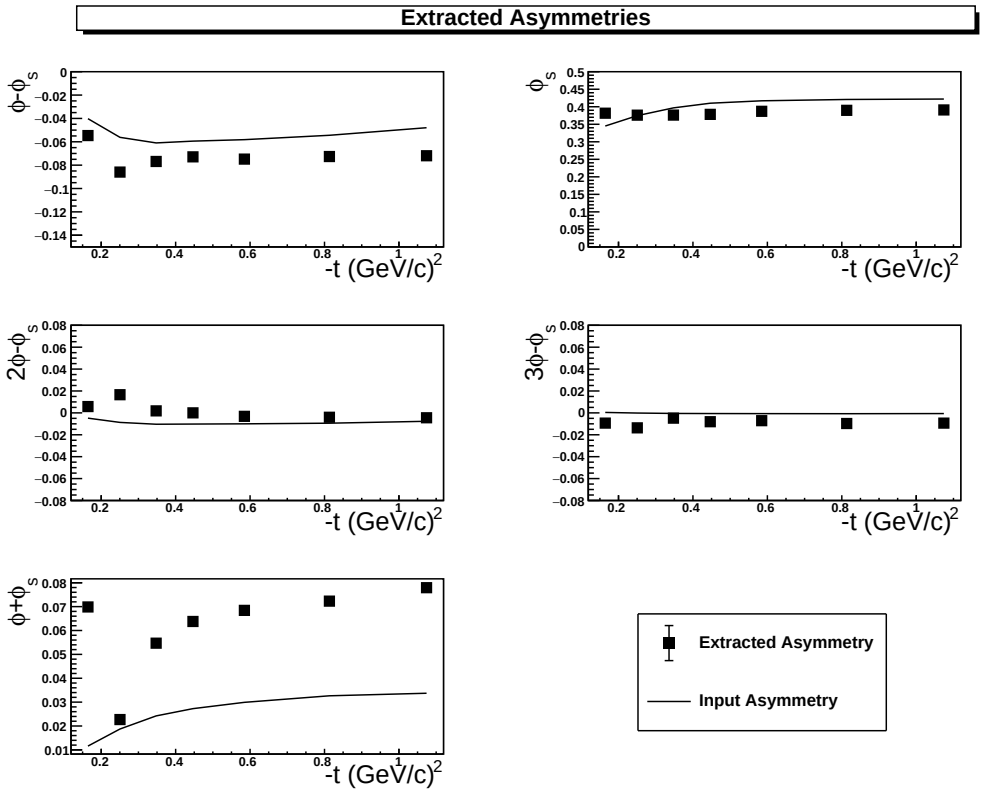

Figure 4.7: Extracted asymmetry results from the UML analysis with no corrective effects enabled. Uncertainties represent fitting uncertainty only, and are included but hidden by the symbols. Lines represent the weighted average value for the input asymmetry amplitude in each bin.

4.7 Corrective Effects

As a particle passes through matter, it is subject to collisions with the particles constituting that matter. This primarily affects charged particles, as they interact electromagnetically with the electrons in the medium. Interactions with atomic nuclei, as well as interactions via the strong nuclear interaction, also contribute, but are less probable.

These collisions will reduce the energy of particles and deflect their paths as they enter the target, leave the target, pass through the air between detectors, and as they pass through the detectors themselves. It is important to understand how these effects will impact the expected acceptance, and the extraction of asymmetries.

4.7.1 Energy Loss

There are two mechanisms included in the event generator, by which particles lose energy as they transition through matter, ionization and bremsstrahlung. The implementation of these effects was originally adapted by Zafar Ahmed [17] from the Hall-A Single Arm Monte Carlo Simulation (SAMC) [39]. The SAMC implementation, and the following sections, are based on thesis work by Xiaodong Jiang [40] and the Particle Data Group Review (PDG) [12].

Ionization

As charged particles pass through matter, they lose energy in elastic collisions with atomic electrons. For high energy particles, the energy loss probability distribution may be described by a Landau distribution with most probable energy loss of [12]

$$\Delta_p = \xi \left[\ln \frac{2mc^2\xi}{(\hbar\omega_p)^2} + j \right] \tag{4.17}$$

where $j = 0.200$ and m is the mass of the traversing particle. $\hbar\omega_p$ is the plasma energy:

$$\hbar\omega_p = \sqrt{\frac{\rho Z}{A}} \times 28.816 \text{ eV} \tag{4.18}$$

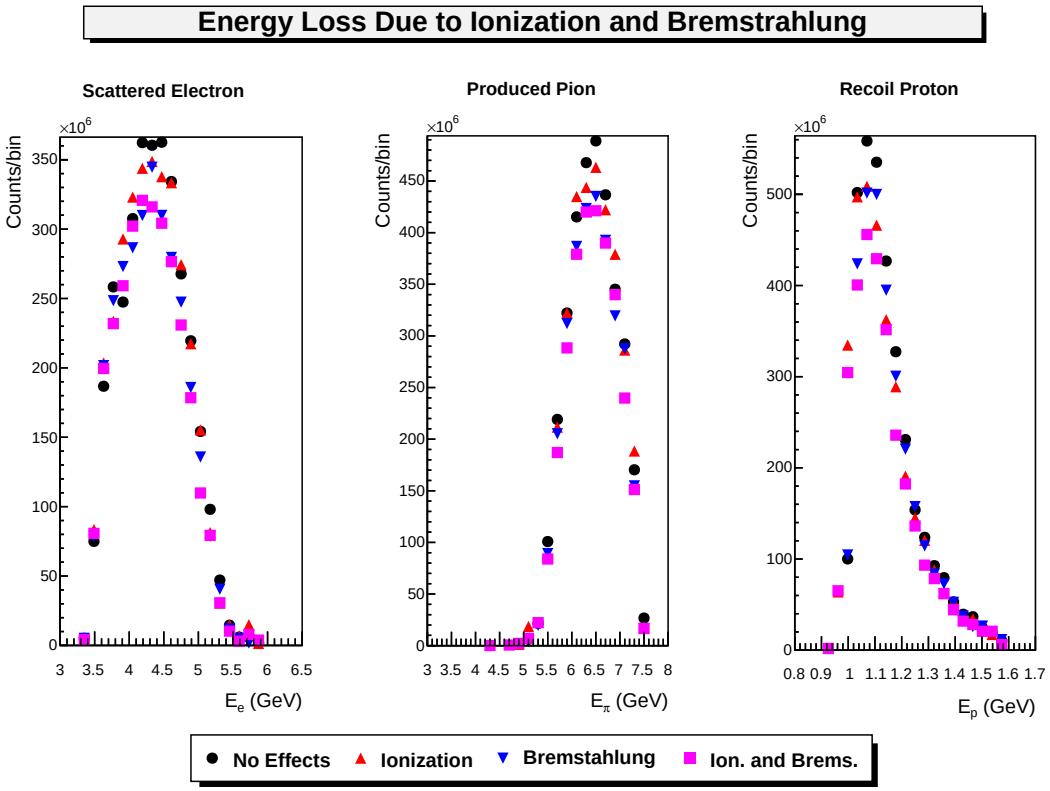

Figure 4.8: Weighted energy distribution of simulated final state particles in the lab frame.

where ρ, Z, and A are the density in g cm^{-3}, atomic number, and atomic mass of the absorber, respectively. The factor ξ is defined as

$$\xi = \frac{K}{2}\frac{Z}{A}z^2\frac{x}{\beta^2} \tag{4.19}$$

where $K = 0.307075$ MeV mol^{-1} cm^2, z is the charge number of the incident particle, and x is the thickness of the absorber. The distribution's full width at half maximum is 4ξ.

In the event generator, the above values are calculated for each particle and material, then passed to a Landau number generator, implemented by ROOT [35], to produce a random number on that probability distribution. The resulting value is subtracted from the energy of the particle while the particles direction is kept the same. The effect of ionization on the energy distribution is shown in Fig. 4.8. As shown, ionization alone has only a minor effect on the energies of the final state particles.

Bremsstrahlung

Bremsstrahlung means "braking radiation" in German. During a collision, energy is not only lost in exchange with the other particle, but also through radiation emitted due to acceleration of the particle. Bremsstrahlung does not affect more massive particles, such as pions or protons, significantly. Typically, only bremsstrahlung of electrons is considered.

When an electron of energy E passes through material of thickness x, the probability of losing energy ΔE [40] is

$$P_e(E, \Delta E, x) = \frac{bx}{\Gamma(1+bt)} \left(\frac{\Delta E}{E}^{bt} \right) \frac{1}{\Delta E}, \tag{4.20}$$

$$b = \frac{4}{3} \left(1 + \frac{Z+1}{9(Z+\eta)\ln(183Z^{-\frac{1}{3}})} \right), \tag{4.21}$$

$$\eta = \frac{\ln(1440Z^{-\frac{2}{3}})}{\ln(183Z^{-\frac{1}{3}})}, \tag{4.22}$$

where Z is the atomic number of the target nuclei.

In the event generator implementation, the energy loss is chosen using

$$\Delta E = ER^{\frac{1}{bt}},$$

where R is a random number chosen from a uniform distribution from 0 to 0.999 (this disallows electrons from losing all of their energy to bremsstrahlung). Bremsstrahlung is applied to the incoming and scattered electrons after ionization energy loss is applied.

The effect of bremsstrahlung on the energy distribution is shown in Fig. 4.8, alongside the effect due to ionization, and due to both effects combined. Again, the effects of bremsstrahlung, or both energy loss effects combined, are minimal.

The effect of energy loss on the missing mass and momentum distributions is shown in Fig. 4.9. The effect is more noticeable here, but still negligible.

Fig. 4.10 shows the effect of energy loss on the UML analysis. The fits are similarly successful as without energy loss, though the $\sin(\phi + \phi_S)$ seems particularly sensitive to this effect.

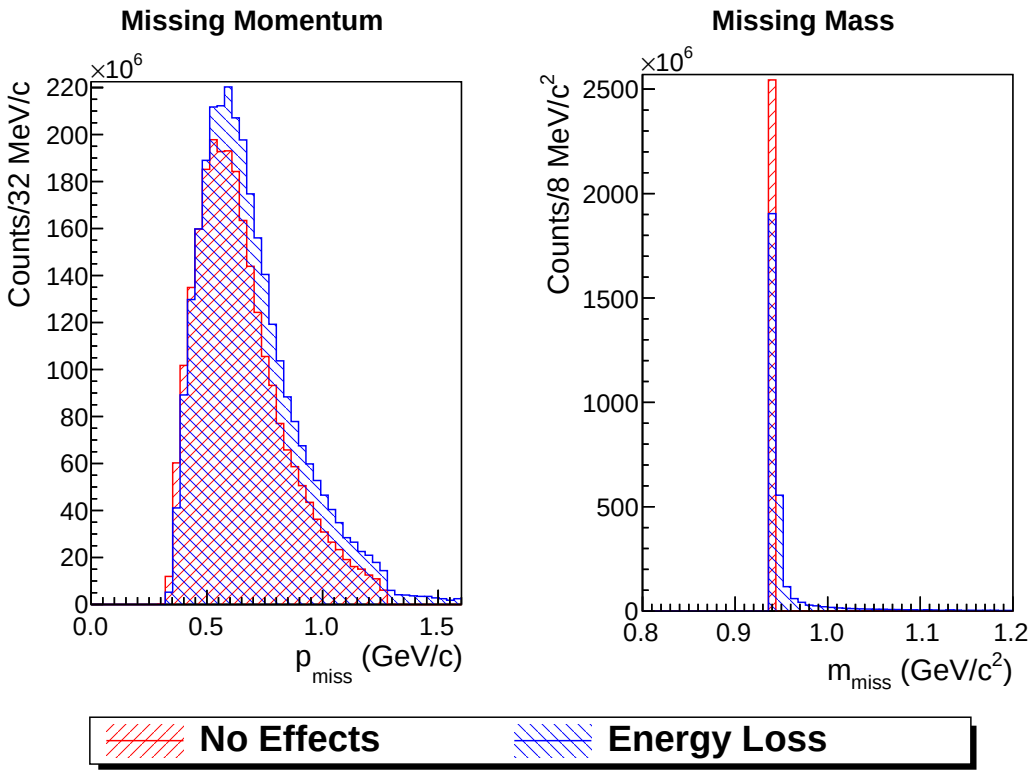

Figure 4.9: Missing mass and momentum distribution with only energy loss effects enabled.

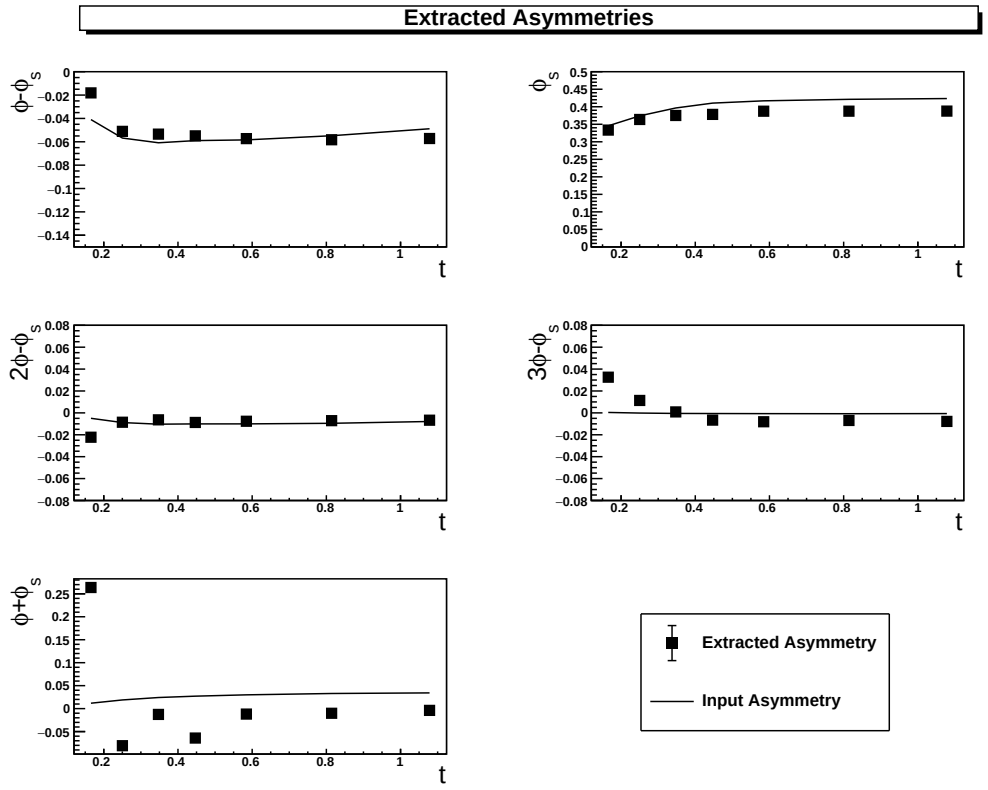

Figure 4.10: Extracted asymmetry results from the UML analysis with only energy loss effects enabled. Uncertainties represent fitting uncertainty only, and are included but hidden by the symbols. Lines represent the weighted average value for the input asymmetry amplitude in each bin.

4.7.2 Multiple Scattering

As a charged particle passes through a medium, it is subject to many Coulomb scattering events. For momenta on the order of hundreds of MeV/c, it is sufficient to use a Gaussian distribution for the net scattering angles through a medium [12]. The rms width for this distribution is given in the PDG [12] as:

$$\theta_0 = \frac{13.6 \text{ MeV}}{\beta c p} z \sqrt{\frac{x}{X_0}} \left[1 + 0.038 \ln \left(\frac{x}{X_0} \right) \right] \tag{4.23}$$

where p, βc, and z are the momentum, velocity, and charge number of the incident particle. x here represents the thickness of the material, defined as the length of material which is traversed multiplied by the mass density (it has dimensions of [mass] [length]$^{-2}$). X_0 is the radiation length of the medium, an intrinsic property of the medium's composition. The PDG defines the radiation length as the mean thickness through which a traversing photon will lose all but $1/e$ of its energy to bremsstrahlung [12].

In the event generator, multiple scattering is calculated by using a coordinate frame in which the initial momentum of the incident particle is along the z-axis. A random θ is selected on the above Gaussian distribution (centered about 0), and a random ϕ selected uniformly from $-\pi/2$ to $\pi/2$. The momentum vector is then rotated about the y-axis by θ, followed by a rotation about the z-axis by ϕ. The particle is then rotated back into the lab coordinate frame. This is done three separate times, in sequence, for three different mediums: target (from the vertex of the interaction to the target window), target window, and air. The incoming electron is also subjected to multiple scattering before the interaction as it passes through the target and target window.

The effect of multiple scattering on the polar angles of the three final state particles is shown in Fig. 4.11. The effect of multiple scattering on the missing mass and momentum distributions is shown in Fig. 4.12. As expected, there is no change to the missing mass, and the effect on missing momentum is small. The effect of multiple scattering is noticeable, but does not significantly alter the shape of these distributions. Furthermore, Fig. 4.13 indicates that the asymmetries may still be extracted successfully with multiple scattering enabled. As in the previous asymmetry extractions, the fits are successful with the exception of the $\sin(\phi + \phi_S)$ asymmetry.

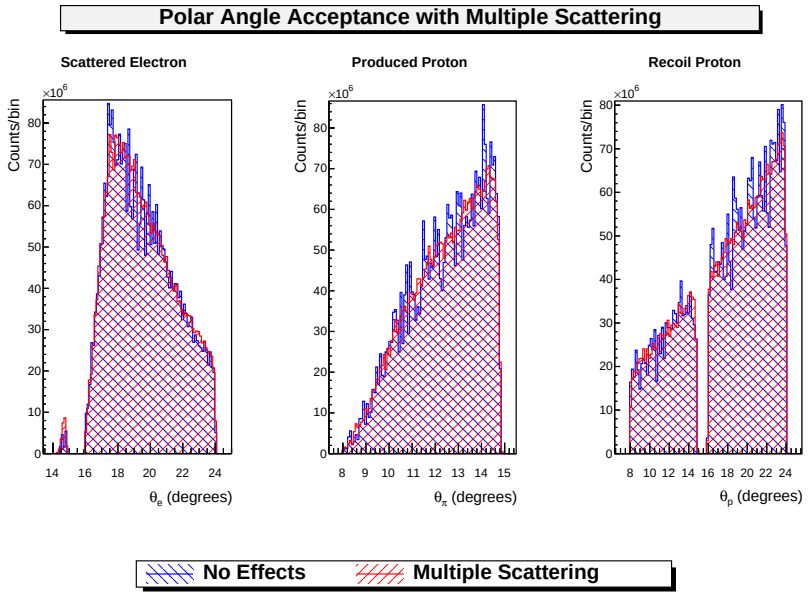

Figure 4.11: Weighted polar angle distribution of simulated final state particles in the lab frame. Data in blue are generated with no corrective effects enabled, data in red are generated with multiple scattering enabled.

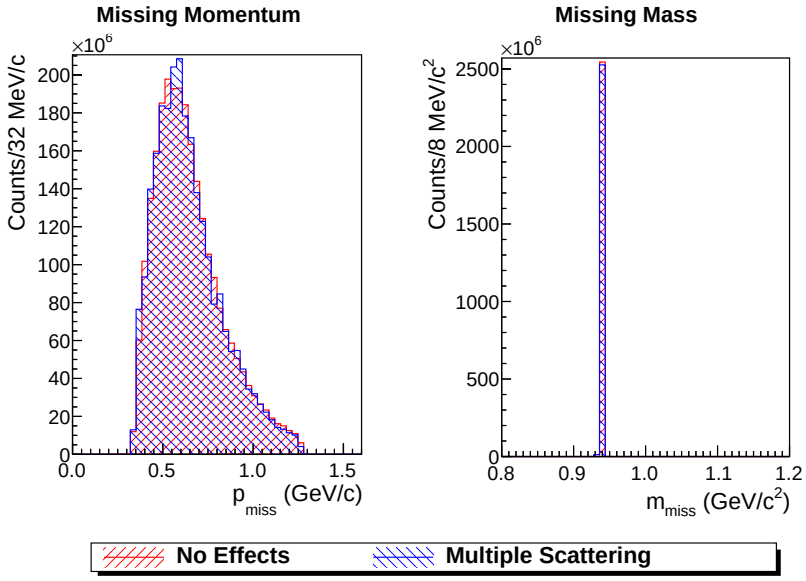

Figure 4.12: Missing mass and momentum distribution with only energy loss effects enabled, shown by the red squares. The blue circles indicate the same data as in Fig. 4.6 for comparison.

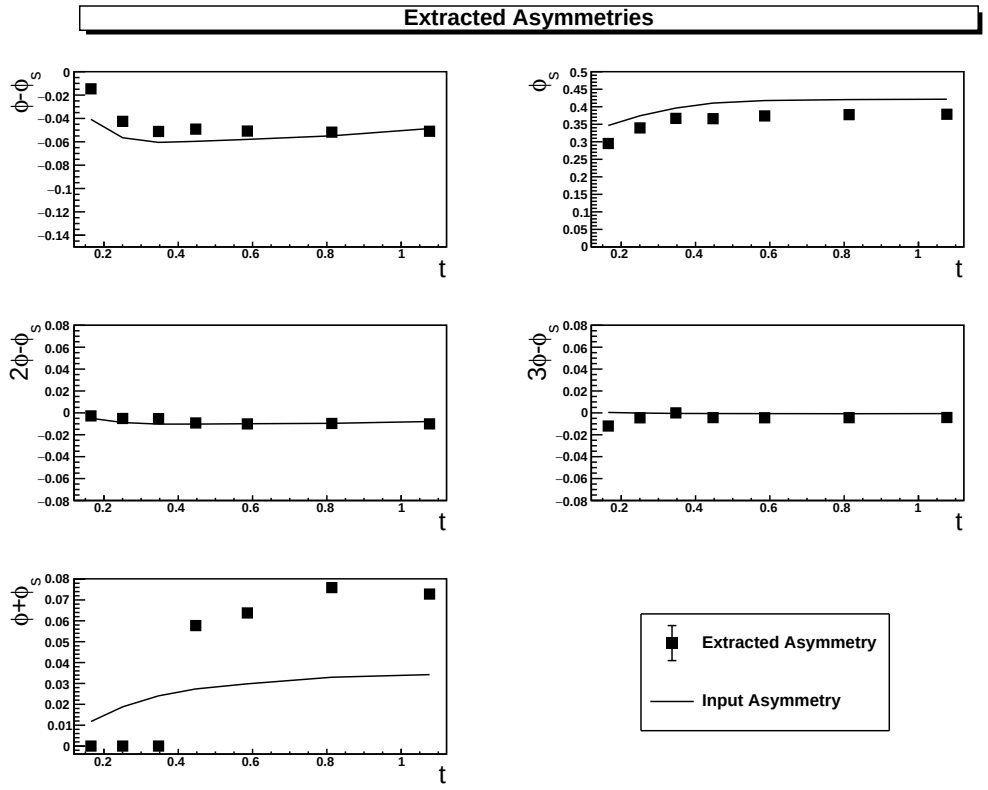

Figure 4.13: Extracted asymmetry results from the UML analysis with only multiple scattering enabled. Uncertainties represent fitting uncertainty only, and are included but hidden by the symbols. Lines represent the weighted average value for the input asymmetry amplitude in each bin.

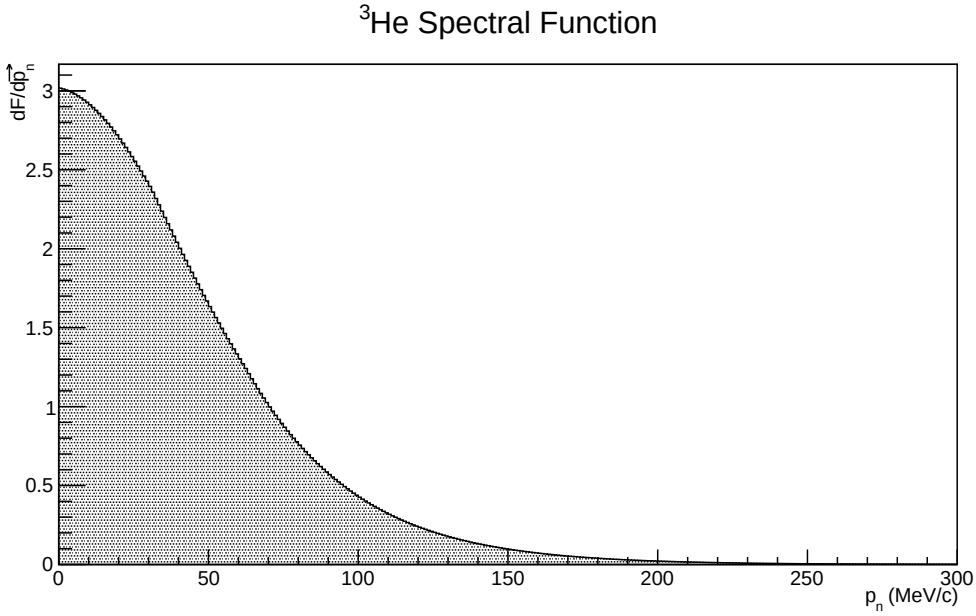

Figure 4.14: ^{3}He spectral function generated according to the Argonne Nuclear Potential [41].

4.7.3 Fermi Momentum

The target neutron in the DEMP experiment is contained within a ^{3}He nucleus. As such, the neutron has a non-zero momentum in the lab frame, known as Fermi momentum. Fermi monentum is incorporated into the event generator in the TargetGen class, which generates the target neutron's momentum before the main kinematics calculation is performed. The direction of the neutron's Fermi momentum is chosen uniformly using sphere point picking [37].

The magnitude of the Fermi momentum follows the distribution shown in Fig. 4.14. This spectral function was produced by a Monte Carlo routine written by Garth Huber and Zafar Ahmed, according to the Argonne Nuclear Potential [41]. The data was originally generated with the following normalization:

$$4\pi \int p^2 \frac{dF}{d\vec{p}} dp \sin\theta d\theta d\phi = 2. \tag{4.24}$$

The distribution was normalized to two in order to describe the two protons in ^{3}He nucleus. For the single neutron, the distribution needs to be normalized to one, as such the data have simply been divided by two and reused in this project.

The resulting momentum distribution is given by a set of 1000 discrete data points, providing the probability density from 0 to 1 GeV/c. As there is no clear, theoretically motivated, functional form for this

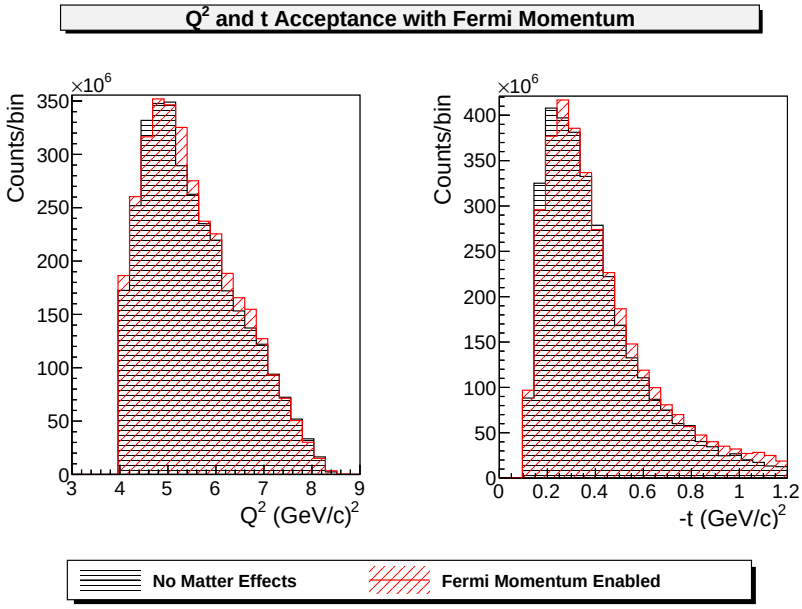

Figure 4.15: Comparison of Q^2 (left) and t (right) weighted distribution with Fermi momentum disabled (blue) and enabled (red).

distribution, the momentum is selected in the generator by a simple Monte Carlo procedure: A point, $(x \in [0, 300], y \in [0, 6.03])$, is randomly selected. If this point lies within the shaded area on Fig. 4.14, then it is used, otherwise the procedure repeats until a point in the shaded area is found. In order to cut down on computation time, the data is truncated at 300 MeV/c beyond which the probabilities are negligible.

Fig. 4.15 demonstrates the effect of Fermi momentum on the generated data. The effect of Fermi momentum on the missing mass and momentum distributions is shown in Fig. 4.16. These plots indicate that the effect of Fermi momentum is minimal.

The effects of Fermi momentum on the asymmetry extraction are shown in Fig. 4.17. Again, the $\sin(\phi + \phi_S)$ asymmetry is most notably affected, while the the other fits agree well with the input.

Fig. 4.18 shows the total effect of multiple scattering, energy loss, and Fermi momentum on the UML analysis. These data clearly demonstrate the possibility of an accurate extraction of, at least, the $\phi - \phi_s$ and ϕ_s asymmetries at high $-t$, from DEMP data.

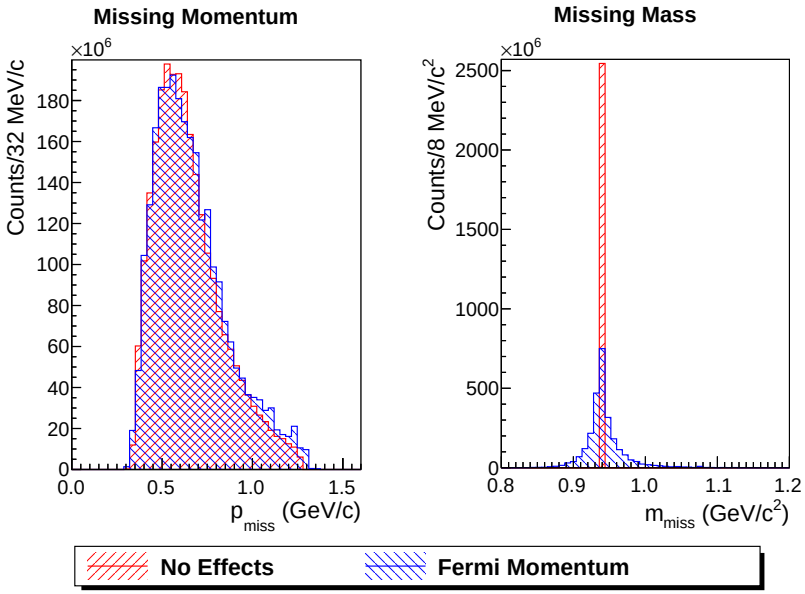

Figure 4.16: Missing mass and momentum distribution with only energy loss effects enabled, shown by the red squares. The blue circles indicate the same data as in Fig. 4.6 for comparison.

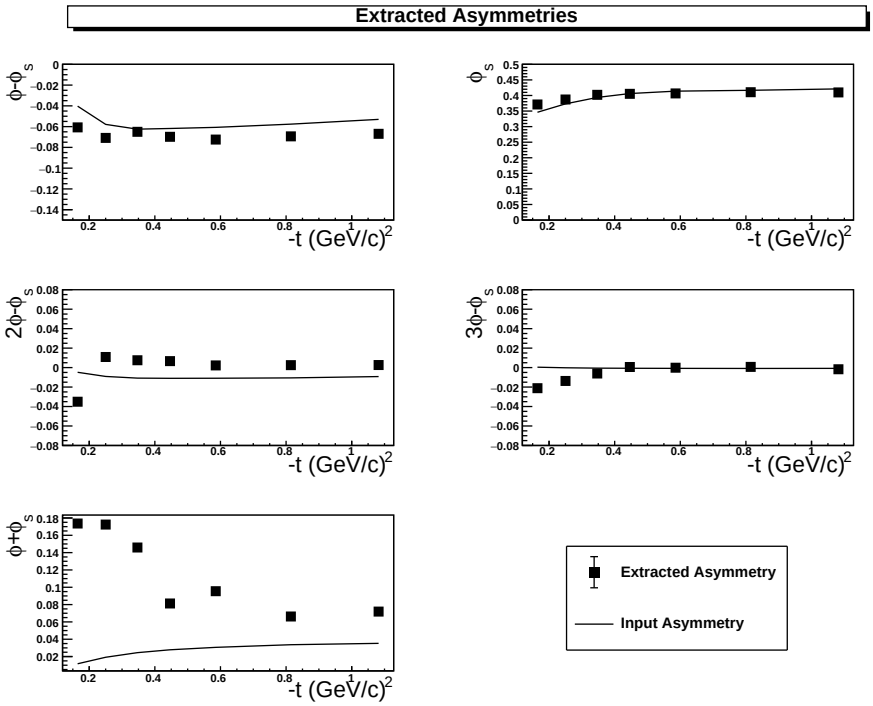

Figure 4.17: Extracted asymmetry results from the UML analysis with only Fermi momentum enabled. Uncertainties represent fitting uncertainty only, and are included but hidden by the symbols. Lines represent the weighted average value for the input asymmetry amplitude in each bin.

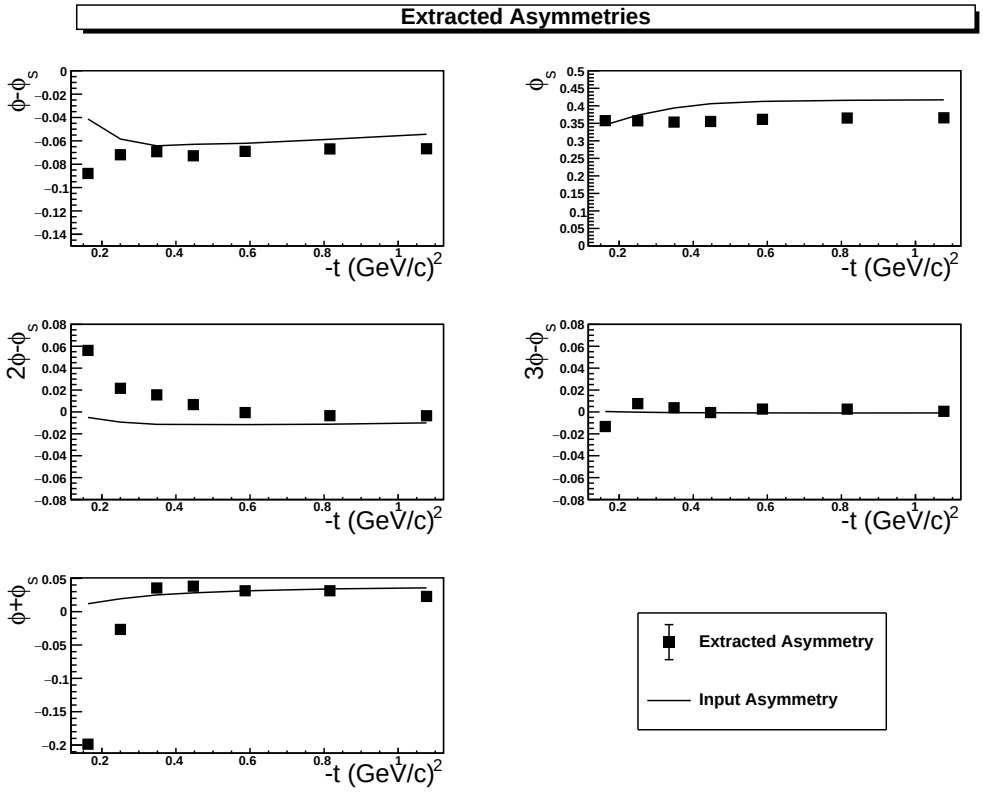

Figure 4.18: Extracted asymmetry results from the UML analysis with multiple scattering, energy loss, and Fermi momentum momentum enabled. Uncertainties represent fitting uncertainty only, and are included but hidden by the symbols. Lines represent the weighted average value for the input asymmetry amplitude in each bin.

4.7.4 Final State Interaction

When the target nucleon emits the charged pion, it is possible for the pion to scatter off of one of the other nucleons in the ^{3}He nucleus as it passes through the nuclear volume. This secondary reaction is known as the Final State Interaction (FSI). A more thorough study on the effects of FSI on DEMP is planned for the future. For the time being however, the effects have been estimated by calculating the kinematics using elastic scattering and the scattering cross section using phase-shift parameterizations by Rowe, Solomon and Landau [42].

FSI is implemented in the event generator using another instance of the TargetGen class to generate a target proton with Fermi Momentum as described in Section 4.7.3. A random direction is selected with sphere point picking [37] to determine the direction of the scattered pion in the pion-nucleon center of mass frame. In the center of mass frame, the total momentum is zero, so:

$$|p_\pi| = |p_p| = p \tag{4.25}$$

$$|p'_\pi| = |p'_p| = p' \tag{4.26}$$

The conservation of energy equation then may be expressed as:

$$E_\pi + E_p = E'_\pi + E'_p \tag{4.27}$$

$$\sqrt{p^2 + m_\pi^2} + \sqrt{p^2 + m_p^2} = \sqrt{p'^2 + m_\pi^2} + \sqrt{p'^2 + m_p^2} \tag{4.28}$$

The only solution to this equation is $p = p'$, and so the kinematics of the outgoing particles are trivial.

The implementation of the cross section calculation was written by A. Shinozaki [43], and further modified by Z. Ahmed [17]. This code is included in the event generator unmodified in order to calculate the $\pi^- N$ differential scattering cross section.

This differential cross section is given in the center of mass frame, and must be transformed via a Jacobian into a Lab frame value which may be used as a correcting factor to the overall event weight. Three different formulations of the Jacobian are made available.

The "William's Weight" uses the following Jacobian [44]:

$$J_{\text{Williams}} = \frac{|p_{\pi,\text{lab}}|^2}{\gamma|p_{\pi,\text{com}}|(|p_{\pi,\text{lab}}| - \beta E_{\pi,\text{lab}}\theta_{\pi,\text{lab}})} \tag{4.29}$$

$$\gamma = \frac{E_{\pi,\text{lab}} + E_{p,\text{lab}}}{|p_{\pi,\text{lab}} + p_{p,\text{lab}}|} \tag{4.30}$$

$$\beta = \frac{|p_{\pi,\text{lab}}| + |p_{p,\text{lab}}|}{E_{\pi,\text{lab}} + E_{p,\text{lab}}} \tag{4.31}$$

The "Dedrick Weight" uses the following Jacobian [45]:

$$J_{\text{Dedrick}} = \frac{\left((g + \cos^2(\theta_{\pi,\text{com}}) + (1-\beta^2)(1 - \cos^2(\theta_{\pi,\text{com}}))\right)^{\frac{3}{2}}}{(1-\beta^2)|(1 + g\cos(\theta_{\pi,\text{com}}))|} \tag{4.32}$$

$$g = \frac{\beta E_{\pi,\text{com}}}{p_{\pi,\text{com}}} \tag{4.33}$$

where β is the same as in the William's Weight. Finally, the "Catchen Weight" uses the following Jacobian [46]:

$$J_{\text{Catchen}} = \frac{|p_{\pi,\text{lab}}|^2 E_{\pi,\text{com}}}{|p_{\pi,\text{com}}|^2 E_{\pi,\text{lab}}} \tag{4.34}$$

The effects of FSI on the missing mass and momentum distributions are shown in Figs. 4.19 and 4.20 respectively, in each of the t bins used in the UML analysis. These figures use the Catchen Weight in weighting the FSI enabled data.

These figures show that a secondary interaction has a much more significant effect on the data than the other corrective effects. However they also indicate that events which undergo FSI occur at a much smaller rate than those that do not. Furthermore, Fig. 4.20 indicates that the majority of FSI events can be eliminated by cutting events with $|\vec{p}_{miss}| > 1.2$ GeV/c. Remaining FSI events constitute only 4% of events [5].

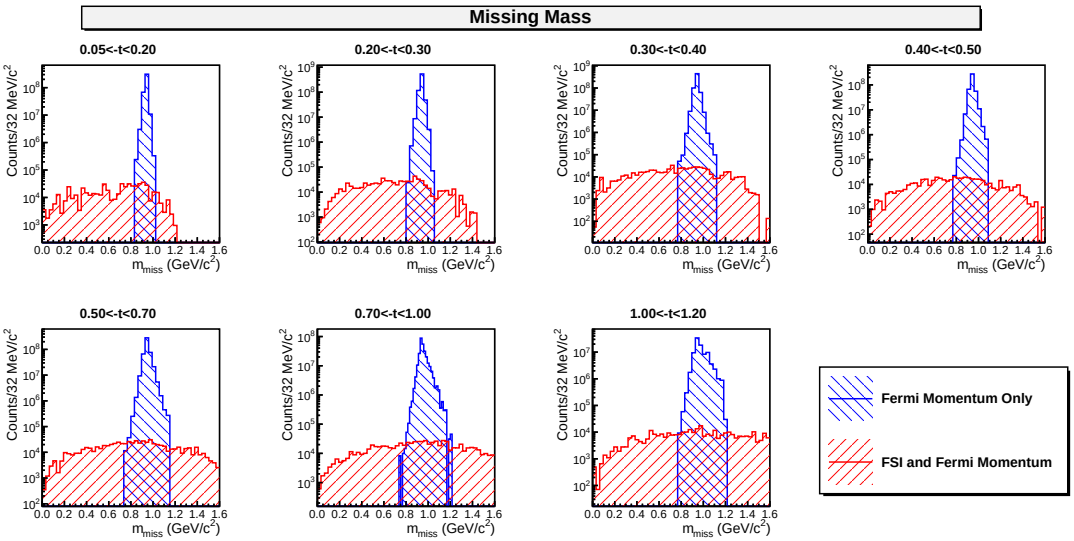

Figure 4.19: Weighted missing mass distribution in each t bin, with FSI and Fermi momentum enabled, compared to the distribution with only Fermi momentum enabled. The FSI distribution uses the Catchen weight in its weighting.

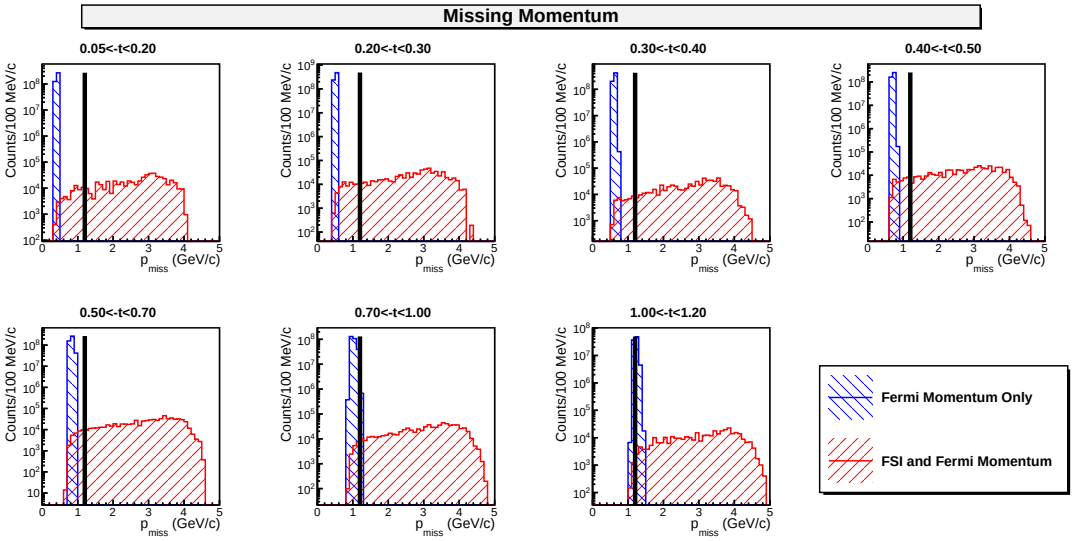

Figure 4.20: Weighted missing momentum distribution in each t bin, with FSI and Fermi momentum enabled, compared to the distribution with only Fermi momentum enabled, and with no effects enabled. The FSI distribution uses the Catchen weight in its weighting.

4.8 Discussion

The DEMP Event Generator has successfully reproduced and expanded upon the results of the original event generator, providing greater flexibility, readability, and statistics. While some discrepancies exist between asymmetry results of the old and new event generator, particularly at low $-t$ (see Appendix A), the possibility of extracting the $\phi - \phi_s$ and ϕ_s asymmetries at high $-t$ values from real data has been demonstrated, with the inclusion of energy loss, multiple scattering, and Fermi momentum effects.

The event generator has shown that the effects of final state interaction may be culled significantly using a $p_{\text{miss}} > 1.2$ GeV/c cut, with remaining events having a negligible contribution.

While the impact of each corrective effect on the acceptance appears negligible, the $\phi + \phi_s$ asymmetry demonstrates a high sensitivity to these effects. While the primary physics interest lies in the $\phi - \phi_S$ and ϕ_S asymmetries, the low quality and high sensitivity of this fit is worth investigating, as the fit is performed simultaneously with those of interest.

In addition, an asymmetry extraction should be attempted on data affected by FSI. The event generator is currently limited in this regard by the fact that it assumes all events undergo FSI. For a proper asymmetry extraction, FSI and non-FSI data need to be mixed.

Chapter 5

Heavy Gas Cherenkov

One of the major components of this work is the prototyping of the front entry window of the SoLID HGC at University of Regina, funded by CFI and Fedoruk Institute.

5.1 Requirements and Preliminary Design

The SoLID Heavy Gas Cherenkov (HGC) detector is an integral part of the SoLID SIDIS configuration. It will be used primarily to identify pions and reject kaons in the momentum range of 2.5 to 7.5 GeV/c. This is accomplished by using C_4F_8O (or equivalent) at a pressure of 1.5 atm (152 kPa, absolute pressure). At 20°C, this provides an index of refraction of 1.002, or a threshold velocity of $0.998c$. This corresponds to a threshold momentum of 2.2 GeV/c for pions and 7.5 GeV/c for kaons. The detector is required to have full azimuthal coverage and maintain high performance in the fringe magnetic field of the CLEO-II magnet (Section 3.4.1), with field strength as high as 20 mT. The geometrical constraints created by the detector's position within the SoLID detector stack leave less than 1 m of gas length for Cherenkov light production, and approximately 10 cm clearance between the front of the HGC and back of the LGC.

The original design of the HGC, before feedback from the prototyping process, consists of a ring made of 10 segments, each with three spherical mirrors and three PMT arrays. This provides a polar angle coverage of 8° to 14.8°.

The preliminary design places two key requirements on the prototype entry window: Bulging of the pressurized window must be kept to less than 10 cm to prevent interference with the LGC, and particle scattering and energy loss must be minimized through use of low Z materials. Aluminum is the typical

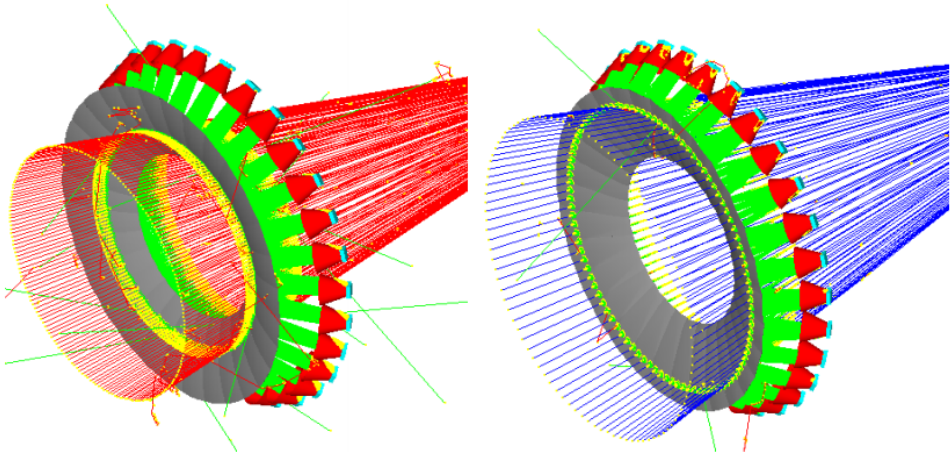

Figure 5.1: GEANT4 simulation of HGC optical system. The spherical mirrors (grey) focus Cherenkov photons (green) created by negatively charged (left) and positively charged (right) pions, onto the PMT arrays (cyan). The effective collection area of the PMTs is increased through use of Winston cones (red) [1].

solution to such requirements, however concerns were raised that an aluminum window would cause high pair production, leading to a large number of false positives. As such, this thesis seeks to finds an alternative entry window material.

5.1.1 Optics

Each of the HGC's 1 m long mirrors will focus Cherenkov light onto a PMT array, 30 total in the preliminary design. Each PMT array may be as small as 20x20 cm through use of light-collecting Winston cones. The PMT arrays planned are Hamamatsu H8500C-03 8 x 8 multianodes. The optical configuration of the HGC design was optimized favoring low angle kinematics, for which particles traverse a shorter gas length. An optimization of the optical system has been performed in GEANT4, taking into account the strong magnetic field [1]. Maximum reflections were limited to two to minimize loss of photons due to imperfect reflection at short wavelengths. Fig. 5.1 was produced by the GEANT4 simulation, and demonstrates the HGC optical design [1].

5.1.2 Gas System

The gases in consideration for use in the SoLID HGC are expensive, at around $300 per kg. As such, as gas system capable of recovering and reusing the gas, removing air and moisture, is highly desirable.

The Low Threshold Cherenkov Detector (LTCC) in JLab's Hall B is a similar, large volume detector,

using C_4F_{10} gas. The planned gas system for the SoLID HGC will as such be of a similar design, and perhaps share some components, with the LTCC [1].

5.1.3 Preliminary Entry Window Design

The preliminary entrance window design consists of two flanges forming the frame. Both pieces have aligned bolt holes, regularly spaced around the circumference. Exterior to the bolt holes, both pieces have a groove to hold an aluminum clamping wire, to crimp and help grip the window material. The flange on the pressurized ("bottom") piece also contains a groove for an O-ring to provide a gas-tight seal. The O-ring and clamping wire themselves are placed beneath the window material on the pressurized side. Fig. 5.2 shows the schematic for the bottom piece of the frame. The top piece is the same but lacks the wire groove. A more detailed view of the bolt, clamp, and O-ring configuration is shown in Figs. 5.3 and 5.4.

5.1.4 Stress Analysis

A finite element analysis of the von Mises Stresses in the entry window was performed by Gary Swift [34]. The results are shown in Fig. 5.5. The analysis indicates that the tension is greatest at the center of the two long, straight sides, followed by the outer curved edge. These are the most likely points of failure.

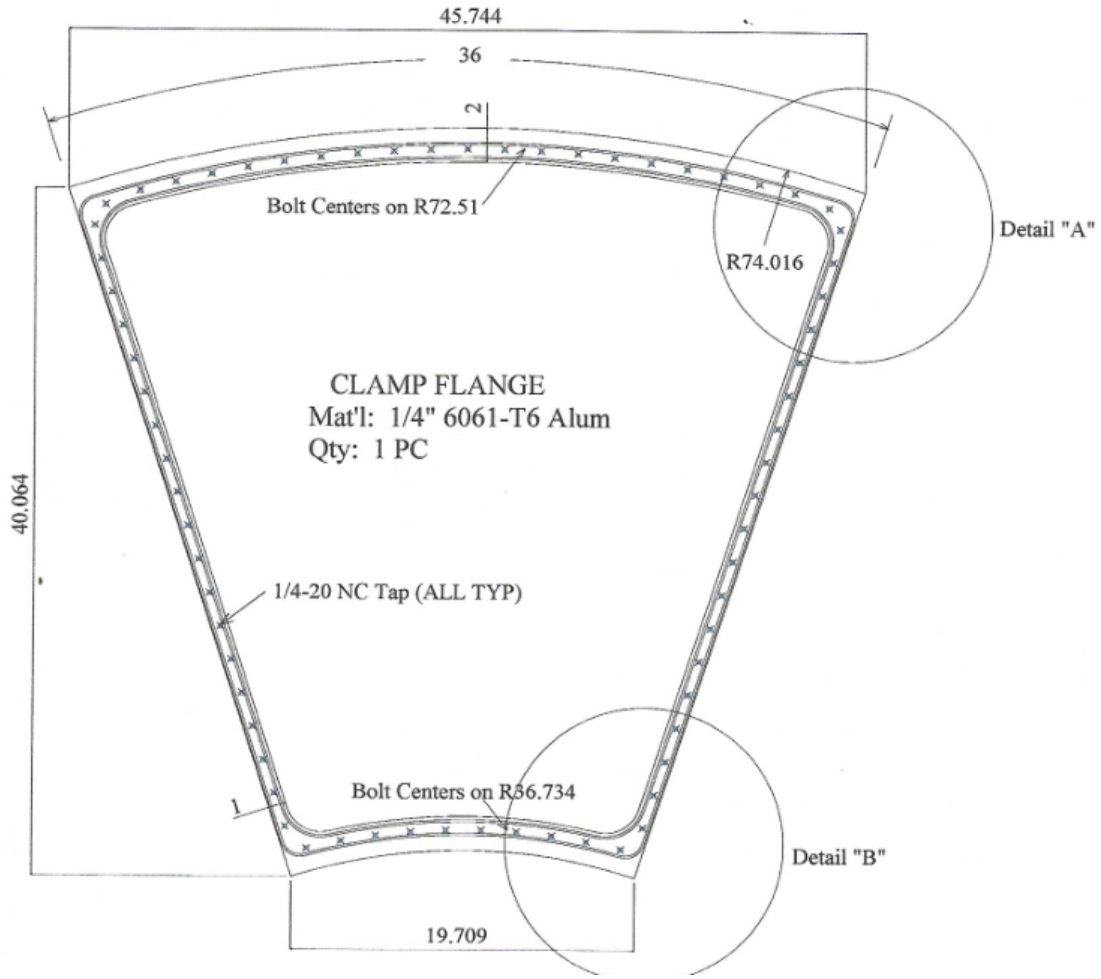

Figure 5.2: Diagram by Lorenz Weber (from the University of Regina machine shop) showing prototype window frame following the preliminary design. Units are in inches. Figs 5.3 and 5.4 show Detail "A" and "B" respectively.

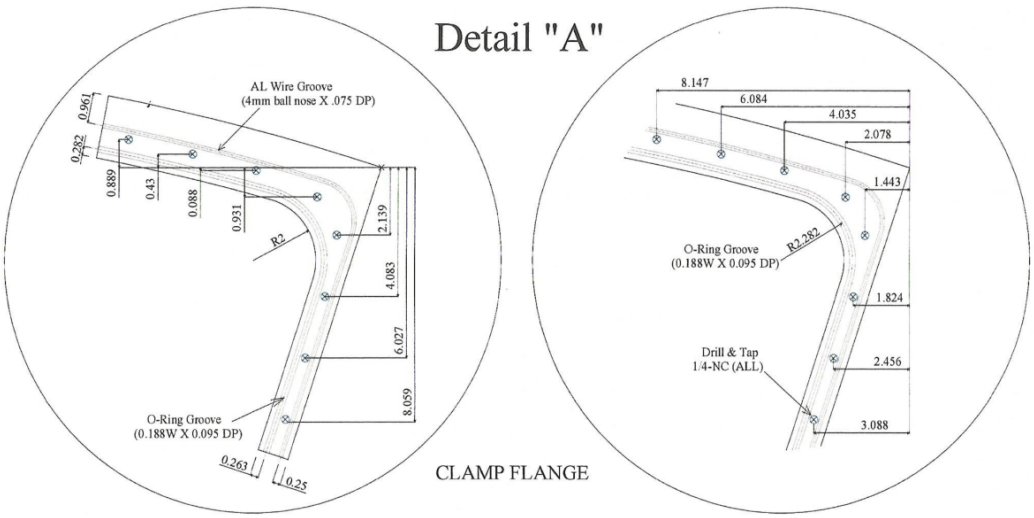

Figure 5.3: Diagram of window frame at Detail "A" in Fig. 5.2. Units are in inches.

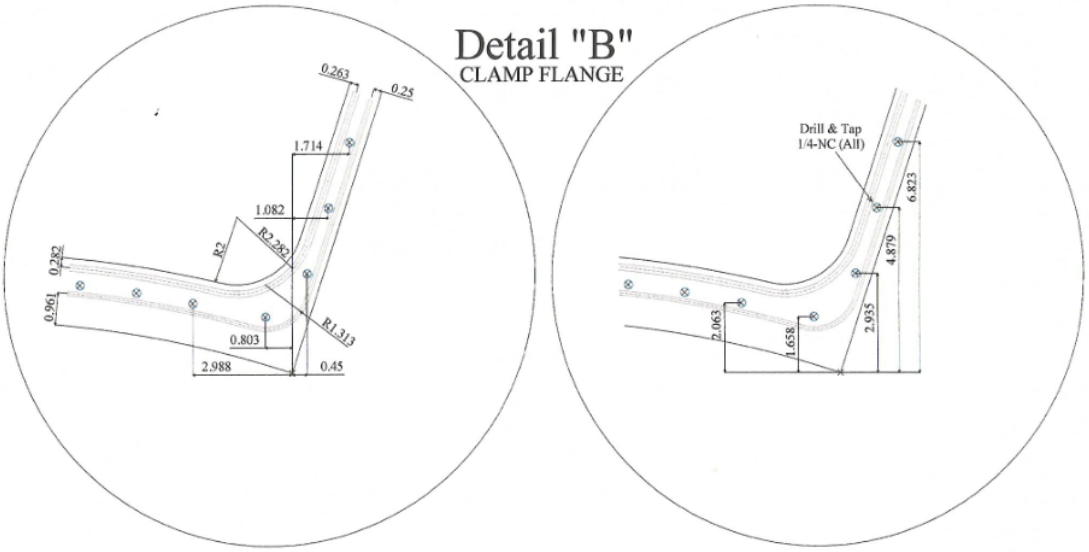

Figure 5.4: Diagram of window frame at Detail "B" in Fig. 5.2. Units are in inches.

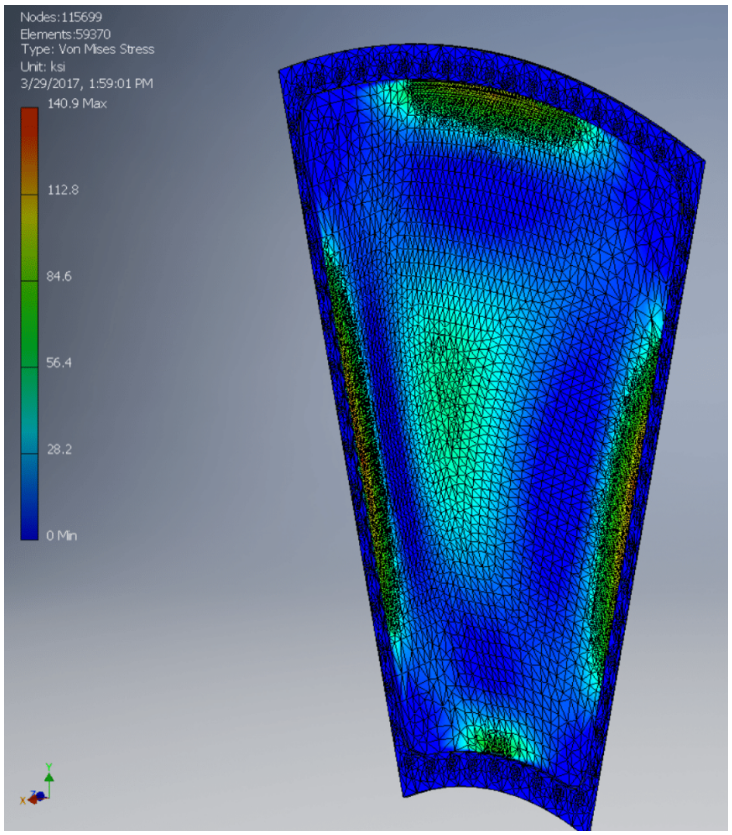

Figure 5.5: Finite element analysis of von Mises Stresses in the HGC entry window [34]. The color axis indicates the tension in the window in units of kilopounds per square inch (ksi).

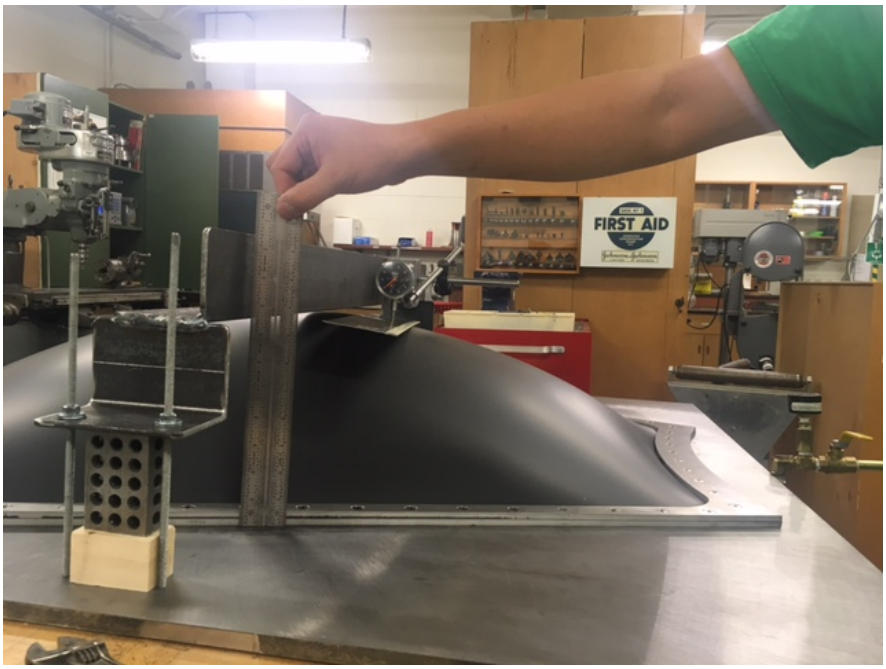

Figure 5.6: Experimental set up including inflated PET/Tedlar window mounted to Frame 1, depth gauge apparatus to measure deflection (center), and pressure gauge and valve (right). Photo taken during the first inflation of the PET/Tedlar window discussed in Section 5.2.3.

5.2 Thin Window Prototyping and Pressure Testing

As the HGC's entry window has been identified as the most likely point of failure, the most logical starting point in the prototyping process is to create a successful window, without the rest of the enclosure.

5.2.1 Pressure Testing Procedure

In order to experimentally test the capabilities of candidate materials, a prototype flange was manufactured based on the specifications given in Section 5.1.3. The material is mounted over the flange and clamped between the two frame pieces, with technique depending on the material. The assembled window is then mounted to a steel plate using an O-ring. A pipe, valve, and pressure gauge is connected to a hole in the center of the plate so air may be pumped in using a hand operated bicycle pump. The pressure gauge reads in units of psi (1 psi = 6.89 kPa). This apparatus is hereby referred to as Frame 1, and is pictured in Fig. 5.6.

After several failed tests using Frame 1, several smaller frames were designed in order to both reduce material usage, and test different flange configurations. A rough frame constructed from acrylic was briefly tested (Frame 2, shown in Fig. 5.7), followed by two steel frames of different flange thickness. These steel

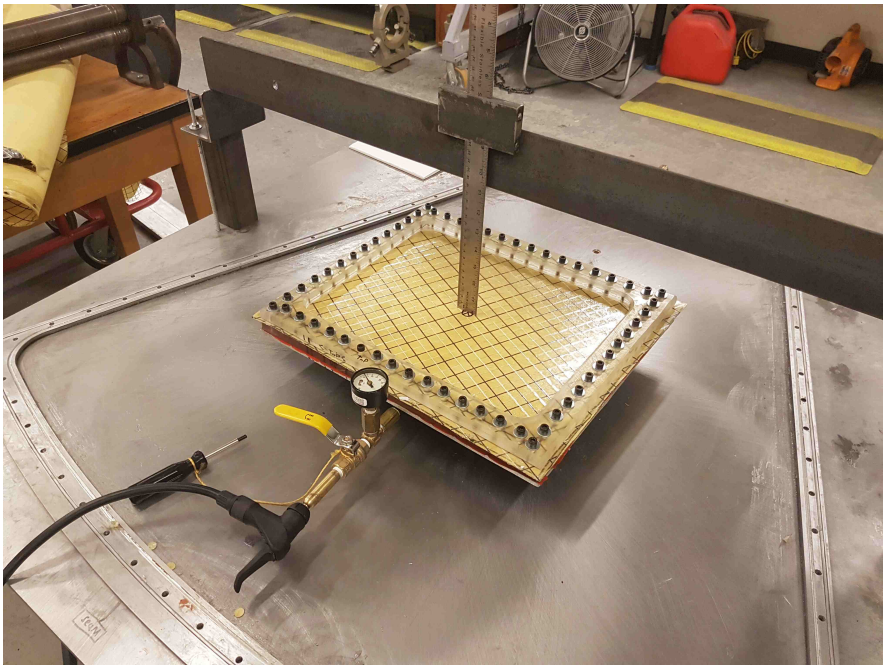

Figure 5.7: Frame 2 with Kevlar-Mylar window (yellow) and ruler deflection apparatus. Also visible, is part of Frame 1, though this is not part of the apparatus.

Frame	Description	Diagram	Sections
1	Full size, according to preliminary design. Aluminum	5.2	5.2.3, 5.2.4, 5.2.5, 5.2.1
2	Approx. $\frac{1}{4}$ scale, acrylic, no wire or O-ring groove	5.8	5.2.4
3	Approx. $\frac{1}{4}$ scale, $\frac{1}{4}$" thick steel.	5.8	5.2.4, 5.2.5, 5.2.1
4	Approx. $\frac{1}{4}$ scale, $\frac{3}{8}$" thick steel.	5.8	5.2.4, 5.2.5, 5.2.1

Table 5.1: Table summarizing the different frames used in the HGC prototyping process. Included in the table are lists of relevant figures and relevant sections for each frame.

frames (and to an approximation, the acrylic frame) followed the schematics given in Fig. 5.8. The two steel frames (Frame 3 and 4) used the same base plate, shown in Fig 5.9, during testing. These frames used a different bolt/clamp/O-ring configuration based on results from testing with Frame 1, which raised concerns that stress was being placed on the bolts instead of the wire. The configuration is shown in Fig. 5.10. Table 5.1 summarizes the different window frames used throughout prototyping process.

In each test, an apparatus is mounted over the frame to measure the deflection of the window. Earlier tests used a precision depth gauge positioned over the center of the window to measure its height past the height at zero over-pressure. The depth gauge reads in units of mil (1 mil = 25.4 µm). The depth gauge proved to have a much higher accuracy than was necessary, but also a narrow range demanding frequent re-positioning and re-zeroing. As such, the gauge was later replaced by a 30 cm ruler (uncertainty of 0.5 mm), mounted in a simple apparatus allowing it to slide vertically.

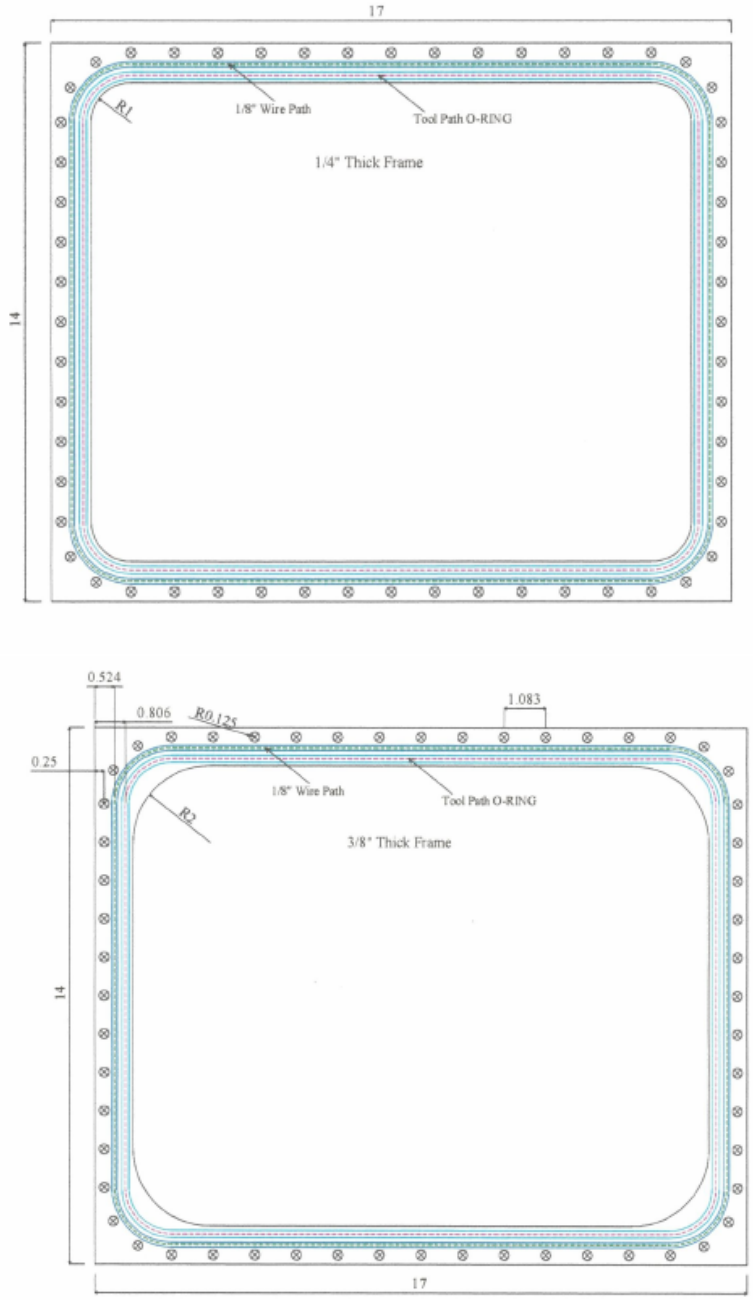

Figure 5.8: Schematic diagram for Frame 3 (top) and 4 (bottom) with units given in inches. R1 = 1" and R2 = 2".

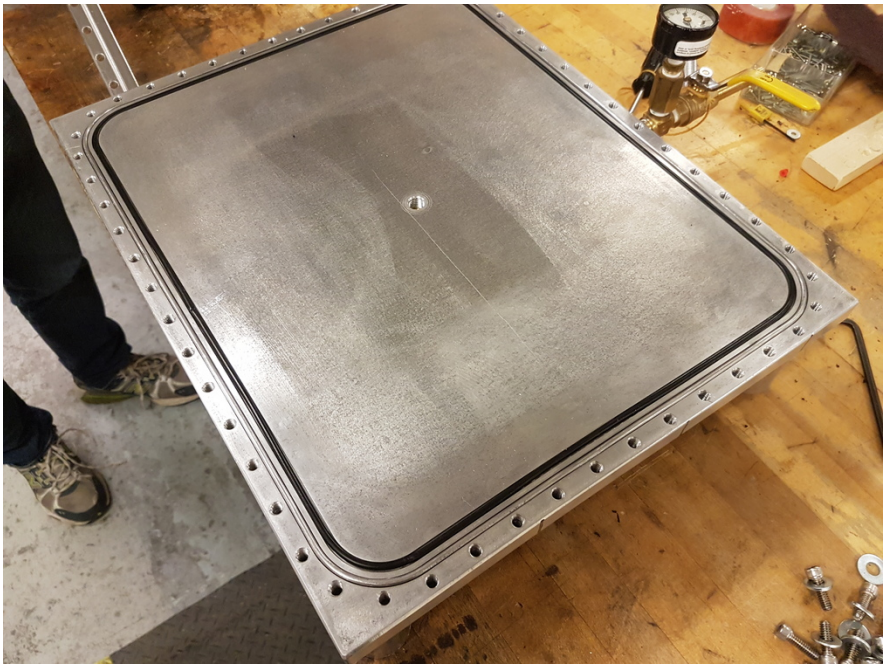

Figure 5.9: Base plate for Frame 3 and 4 with O-ring and clamping wire in place.

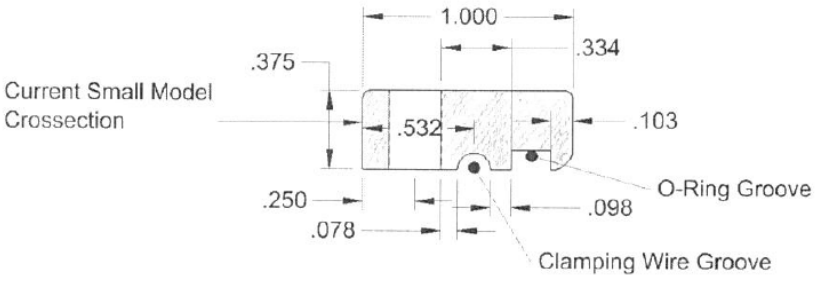

Figure 5.10: Cross-section view of the bolt/wire/O-ring configuration for Frames 3 and 4. Dimensions are in units of inches.

Once the window is prepared, the base procedure for the pressure tests was as follows:

- Either zero the measuring apparatus, or set a reference measurement at zero over-pressure and the valve open.
- Inflate the window a small amount and close the valve.
- Wait a short time for the window to stabilize and measure the deflection and pressure.
- Repeat in small increments of pressure until a target pressure is reached (see Section 5.2.2).
- Perform "soak test" by leaving the window pressurized and sealed for an extended period of time (ideally, many weeks) and observe changes in pressure and deflection.
- Checks for leaks are performed throughout both inflation and soak tests using a soap and water spray.

The precise procedure is modified for each test depending on the most pertinent questions, needs of the particular configuration, as well as emerging results and circumstances during the running of the test.

5.2.2 Window Tension Estimate

In order for testing with the smaller frames to be useful, the maximum tension in the window under pressure should be approximately the same as in the full sized window. In order to estimate a pressure scale factor we consider a strip of material of unit width, under uniform force per unit length, perpendicular to its surface, fixed at its ends. Fig. 5.11 shows a force diagram of the strip.

Assuming the strip takes the shape of a circular arc, the radius of curvature, r, is related to the deflection, h, and width, w, by:

$$r = \frac{w^2}{8h} + \frac{h}{2}. \tag{5.1}$$

Then under a pressure, P, the tension is:

$$T = Pr. \tag{5.2}$$

If w is taken to be the maximum width of the full size widow, 116.19 cm, differential pressure to be 1 atm (operating pressure with safety factor of 2), and deflection restricted to 2.5 cm, the resulting tension is

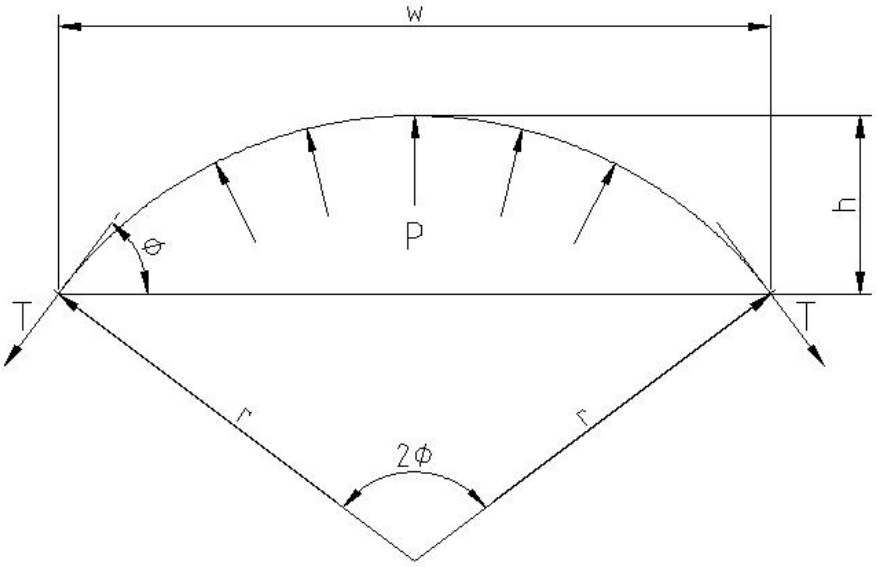

Figure 5.11: Force diagram of a strip of window material of unit width, under equal load per unit length, normal to surface. This approximates the window under pressure.

6.5 kN/cm. Allowing a deflection of 10 cm, however, reduces the tension to only 1.8 kN/cm. This strong relation between deflection and tension indicates a significant trade off when using stronger materials, which tend to stretch less significantly, as lower deflections increase the stress on the frame.

From Equations 5.1 and 5.2, it can also be determined that for a frame with approximately one quarter the dimensions, a four times increase in pressure is required to match the window tension. This gives a target pressure of 60 psi (414 kPa) for Frames 3 and 4.

5.2.3 PET and Tedlar

The first test used three-layer polyethylene terephthalate (PET) and Tedlar® (1.5 mil Tedlar, 3mil PET, 1.5 mil Tedlar) from Madico Inc. [47]. The material was draped over Frame 1 and pulled taut by hand, then cut and mounted, as shown in Fig. 5.6.

Upon initial attempts to inflate the window, it failed to hold pressure. A small anomaly was noted on the surface of the window. Upon closer inspection, a small piece of metal was found to have punctured the window. Many more small pieces of metal were also noted. This was most likely from drilling of the bolt holes in the flange, as this window material was the first to be tested on the newly constructed frame. The window was removed from the base plate and patched with a small piece of the same PET/Tedlar and 5

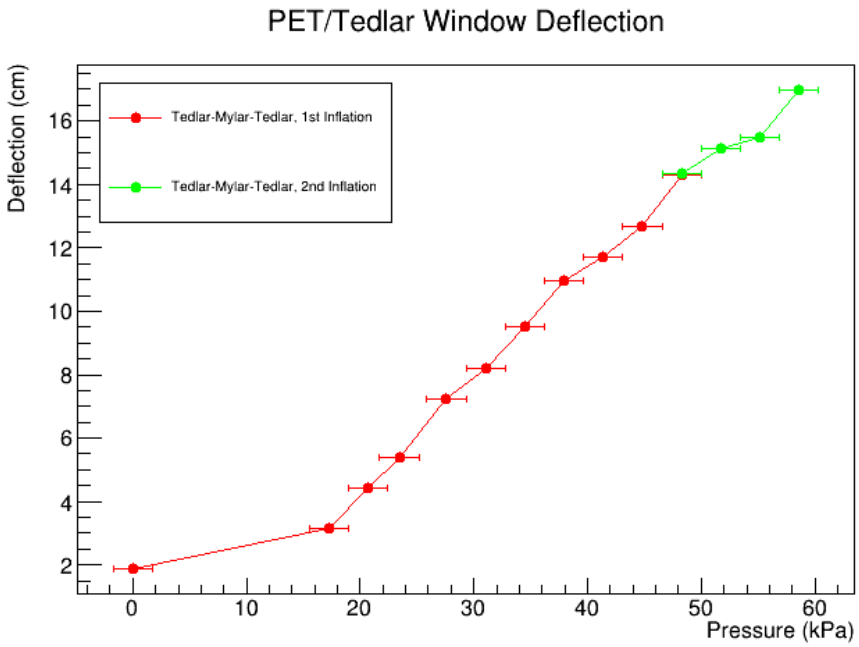

Figure 5.12: Deflection of PET and Tedlar window as a function of pressure. Red points are the initial inflation, and green points are after deflation and re-inflation.

minute epoxy. Upon a second attempt to inflate the window it was now able to build pressure.

The window was inflated in increments of 0.5 to 1 psi, pausing between inflations to allow the window to settle and take measurements. At a differential pressure of 7 psi (48.3 kPa), the total deflection was 5.64" (14.3 cm). The deflection data are shown in Fig. 5.12 by the red points.

The window was then left at pressure overnight. Over approximately the next 22 hours the pressure decreased by 1 psi and the deflection increased by 1.15" (2.92 cm). The decrease in pressure was attributed primarily to the expanded volume of the window.

The window was then fully deflated to observe the elastic properties of the window material. The material did not return to its original shape and approximately retained the shape it had assumed under pressure.

The window was then re-inflated to 7 psi (48.3 kPa). The deflection is assumed to have returned to approximately the same height as before deflating and testing resumed. Pressure was increased past 7 psi (48.3 kPa) with the goal of reaching 14 psi to satisfy the safety factor. The data are shown in Fig. 5.12 by the green points.

The window reached a pressure of only 8.5 psi before a leak was noted. The leak was perceptible by touch and appeared to originate from in between the window material and the top flange piece on the inside of the frame. While inspecting the site for the cause of the leak, catastrophic failure occurred, and the window

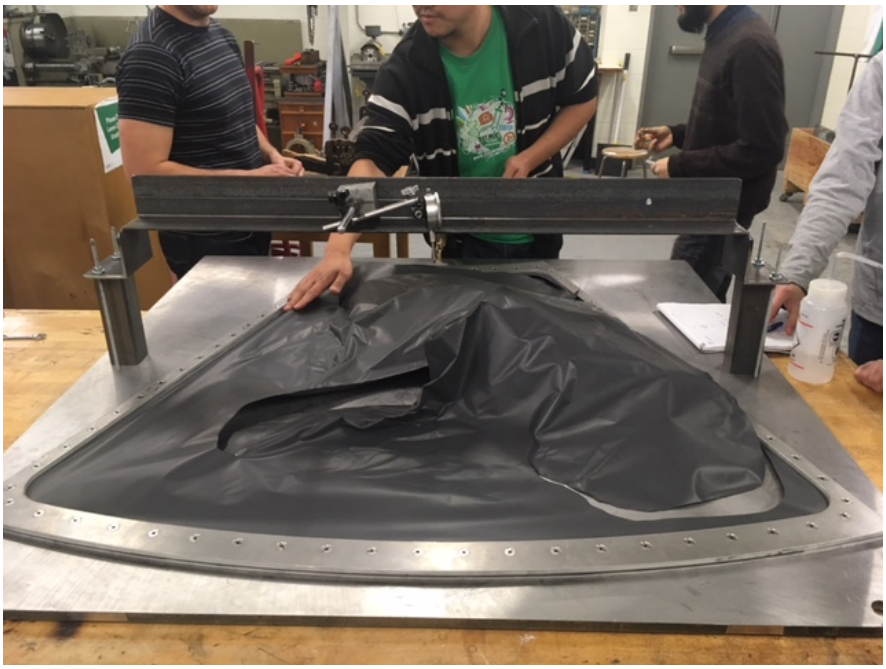

Figure 5.13: Aftermath of failure of the PET/Tedlar window.

burst. The aftermath is shown in Fig. 5.13.

The failure occurred close to the location of the repair patch. The repair may have contributed as the epoxied material was less able to stretch. However, this is also close to one of the long sides highlighted in Fig. 5.5 as a point of high stress. The material created a good air-tight seal, however the deflection exceeded the maximum allowed, and failed to reach the required pressure. In conclusion, PET/Tedlar alone is not suitable for the HGC entry window. Similar materials are also considered unlikely candidates. However this material, and similar materials, are good candidates to provide an air-tight seal in conjunction with another material providing the required tensile strength.

5.2.4 Kevlar and Mylar/Tedlar

Samples of Mylar and Kevlar have been acquired from Challenge Sailcloth [48]. The Mylar has a thickness of 5 mil and is crosshatched with strands of carbon fiber and fiber glass. The Kevlar has a thickness of 12 mil and comes with an adhesive backing. This Kevlar is intended for use as patch material for racing sails, but this provides a suitable source for affordable Kevlar with sufficient dimensions and quantity appropriate to these prototyping efforts.

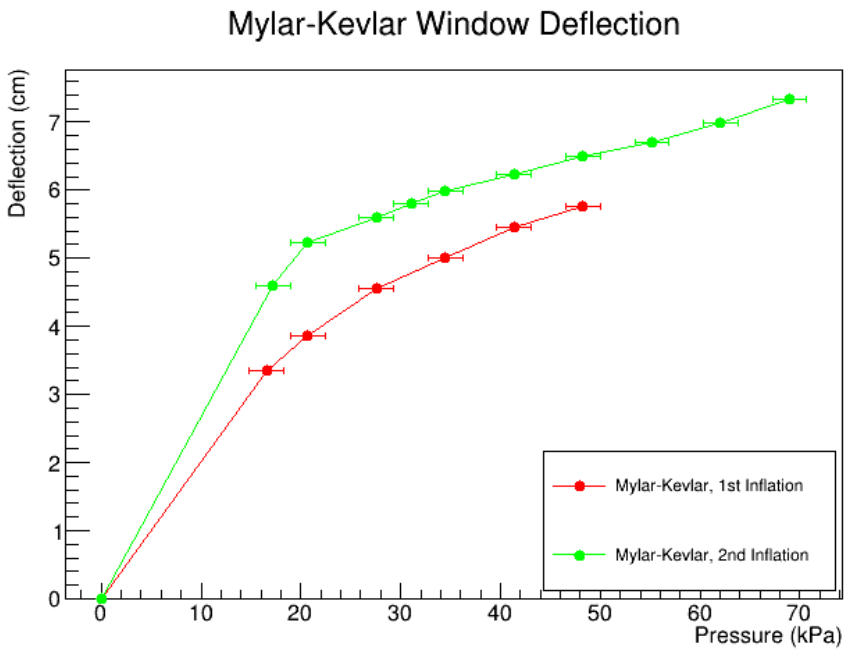

Figure 5.14: Deflection of Mylar/Kevlar window versus pressure. Red points indicate data for the first inflation, and green points indicate data after the window has been deflated and re-inflated.

Test 1: Mylar-Kevlar, Frame 1

In the first test with these materials, a single layer of Kevlar is bonded to a layer of Mylar using the included adhesive backing. The material is then draped over Frame 1 and pulled taut by hand, then cut and mounted. Deflection is measured using the precision depth gauge.

Pressure was increased incrementally to 7 psi (48.3 kPa), at which point the material had bulged to a height of 2.17" (5.52 cm). The data are shown in Fig. 5.14.

A 24 hour soak test was then performed, during which the window deflection increased by 260 mil (6.6 mm), with no measurable change in pressure. The window was then deflated to observe the elastic properties. The window returned nearly to its original state with only slightly more slack than before inflation.

The window was then re-inflated, continuing past 7 psi (48.3 kPa). The data are shown in Fig. 5.14 by the green points. During this phase, while the valve was sealed for data collection, pressure was noted to be slowly decreasing, indicating a potential slow leak. While pumping between 8 and 10 psi, creaking noises were noted coming from the window as it expanded. Shortly after passing 10 psi, a portion of the material slipped out of the flange causing the window to burst. The aftermath is shown in Fig. 5.15.

Analysis of the material after failure indicates that point of failure was where the clamping bolts passed through the material. It is suspected that the clamping wire did not sufficiently hold the tension in the

Figure 5.15: Aftermath of window failure during first Kevlar/Mylar test, focused on the portion that slipped from the flange.

window, allowing the force to pass to the bolts. The point of failure is in close proximity to the point of the previous PET/Tedlar test (Section 5.2.3), near the middle of the longest edge. While close inspection reveals no particular fault at this point in the frame, this is again one of the high stress points highlighted by Fig. 5.5.

The overall deflection at operating pressure exceeds tolerances. Considering this and the ultimate failure of the window, this configuration is deemed unsuitable for the HGC entry window. However, these results are a substantial improvement over the PET/Tedlar window, and merits further testing.

Test 2: Mylar-Kevlar, Circumference Epoxy, Frame 1

In this test, a single layer of Kevlar was bonded to a single layer of Mylar as in the first test. After cutting to shape, LePage ® epoxy resin was applied to the circumference and given 24 hours to set before being mounted to Frame 1. This was done in hopes of strengthening the Kevlar near the failure point of Test 1. This test was the first to use the revised deflection measurement apparatus.

Pressure was increased incrementally to 7 psi (48.3 kPa), at which point the deflection was 6.85 cm. These data are shown in 5.16 by the red points.

After sealing the valve at 7 psi (48.3 kPa), a slow decrease in deflection was noted. Using a spray

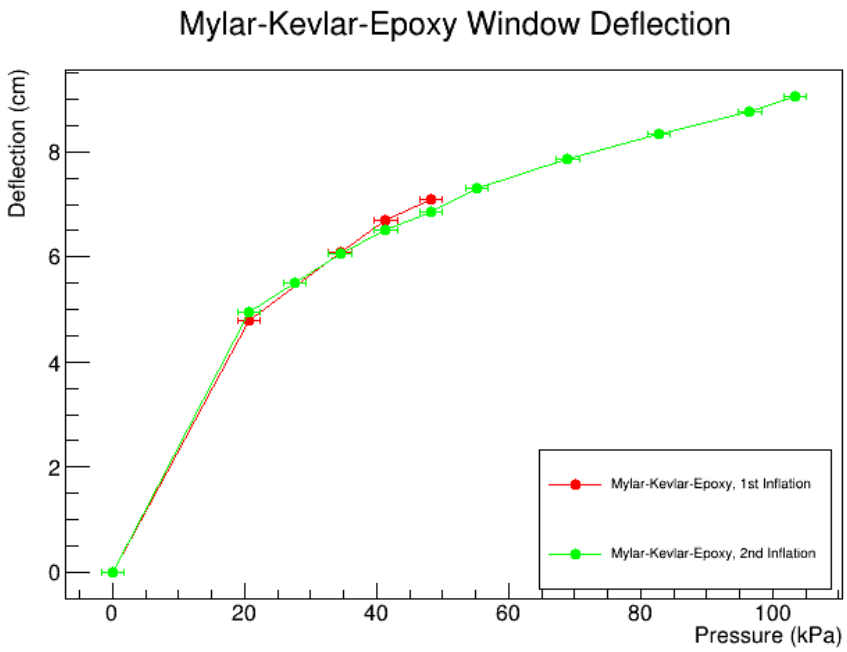

Figure 5.16: Deflection of Mylar/Kevlar window versus pressure. Red points indicate the initial inflation. Green points indicate data after the window was deflated and re-inflated.

bottle with a soap and water mixture, several leaks were identified around the circumference of the window. Bubbling was observed on the outer circumference of the flange, indicating air escaping underneath the Mylar layer. Bubbling was also observed around the bolts, indicating air escape through the bolt holes. Both of these leakage points are outside of the O-ring, indicating failure of the airtight seal.

No soak test was performed due to the clear failure of the seal. The window was deflated and disassembled, then reassembled with additional vacuum grease on the O-ring. The window was inflated again to 7 psi (48.3 kPa), at which point the same leaking was observed. The decision was made to force a failure by continuing to pump and find a maximum pressure. The data from this phase are shown in Fig. 5.16 by the green points. The window failed shortly after passing 15 psi when the material tore from the flange along one edge and burst. Fig. 5.17 shows the aftermath of the window failure.

The failure of this test appears similar in cause to the first Mylar/Kevlar test, indicating potential problems with the design of the frame itself. This test prompted the construction of a miniaturized frame to test alternate frame designs, as well as continue testing window materials, both at reduced material cost.

Figure 5.17: Aftermath of window failure during second Mylar/Kevlar test.

Test 3: Mylar-Kevlar, Epoxy Coating, Frame 2

This test was the first to use one of the miniature test frames discussed in Section 5.2.1. Frame 2 is made from acrylic with a similar design to the later Frames 3 and 4, though lacked both O-ring and wire grooves. At 35.6 cm by 28 cm, it is approximately $\frac{1}{4}$ the dimensions of Frame 1. Equations 5.1 and 5.2 indicates that this necessitates a four times increase in pressure in order to match tension in the window. Including safety factor, this results in a target pressure of up to 60 psi (414 kPa).

The material for this test consisted of two layers of Kevlar in between two layers of Mylar (MKKM). The material was cut to shape and LePage 5 minute epoxy was used to the bind the two Kevlar layers together, and given 24 hours to set, before mounting to Frame 2.

Pressure was raised to 20 psi, at which point the deflection was 2.7 cm. Fig. 5.18 shows the deflection versus pressure by the red points.

The pressure was noted to be decreasing while the valve was closed. Soap and water spray revealed several leak points, both around the outer circumference and through the bolts.

The window was deconstructed and reassembled with additional vacuum grease to attempt to eliminate the leaking. It was then re-inflated to a more conservative 10 psi and left overnight to identify any improvement in the seal. The window was found to be maintaining pressure so testing resumed to higher pressures.

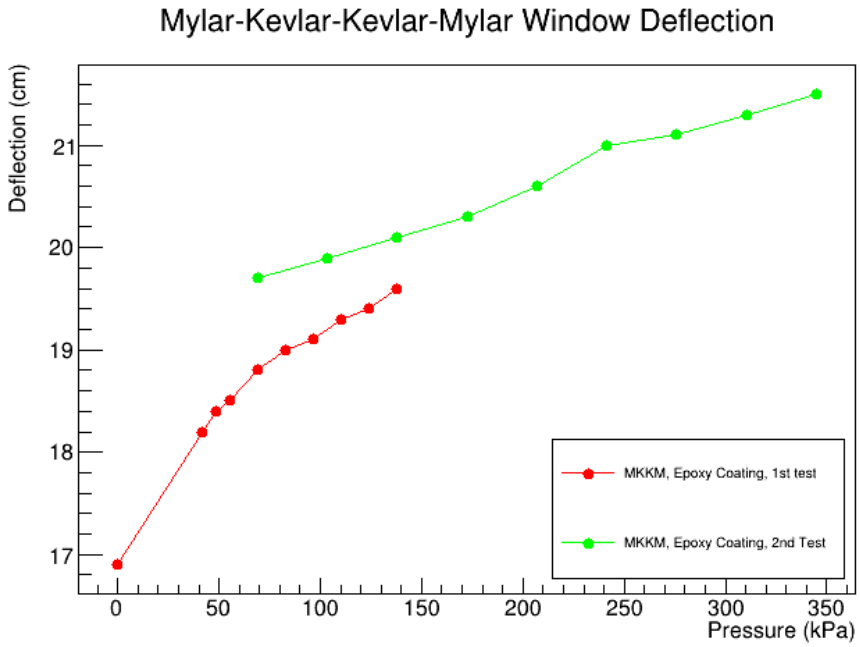

Figure 5.18: Deflection of acrylic frame Mylar/Kevlar frame versus pressure. Red points indicate the initial inflation. Green points indicate inflation after adjustments and reconstruction.

The green points in Fig. 2 show the data after re-inflation. At a pressure of 50 psi and deflection of 4.6 cm the window began leaking again, now much more rapidly. At this point deformation in the frame was noted, as shown in Figs. 5.19 and 5.20.

This test demonstrated a promising method for further testing of window materials. However the need for a more substantial and complete design is clear. Frame 2 includes no O-ring or clamping wire, as in the design of the full window. The window also needs to be mounted to a thicker plate to avoid the deformation shown in Figs. 5.19 and 5.20. This test prompted the construction of Frame 3.

Test 4: Pre-stretched Mylar, Kevlar, and Epoxy, Frame 3

Considering notable differences in deflection after repeated inflation in previous tests, it was suggested to pre-stretch the material before mounting. In this test, a layer of Kevlar was adhered to a layer of Mylar. The material was stretched over a wooden frame using a vise grip, and stapled in place as shown in Fig. 5.21. The Kevlar was then coated with LePage 5 minute epoxy and allowed to set. The material is then clamped into Frame 3 and cut from the wooden frame. Results for the pressure test are shown in Fig. 5.22 in red.

Between 40 and 45 psi the window burst, tearing along the full length of three of the sides, and demolishing

Figure 5.19: Top down view of the window frame and plate, showing inward deformation at 50 psi. A straight steel rod provides a reference.

Figure 5.20: Side view of the window frame and plate, showing upward deformation at 50 psi.

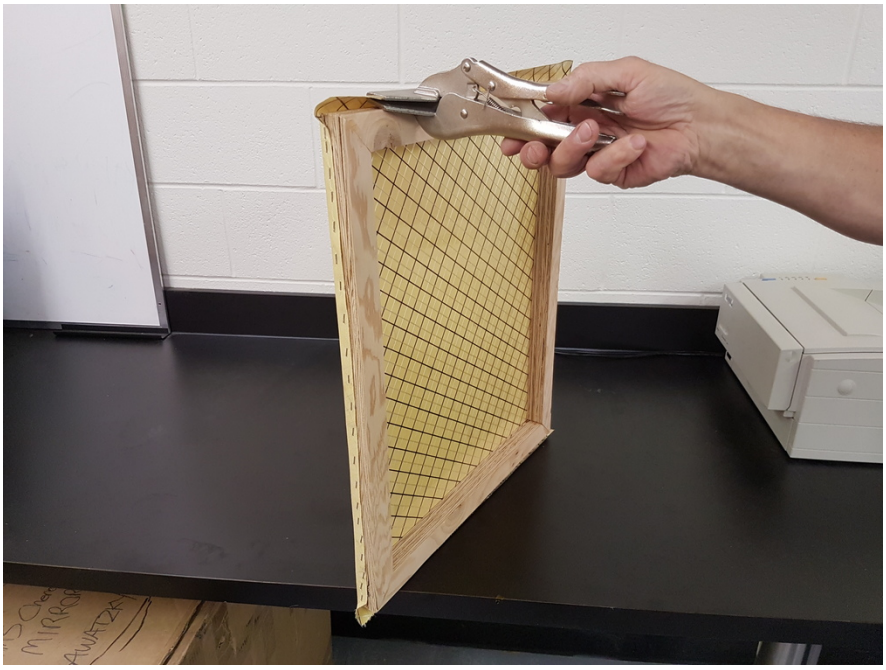

Figure 5.21: Pre-stretching of window material over a wooden frame before Test 4. The same procedure is used in Tests 5 to 8.

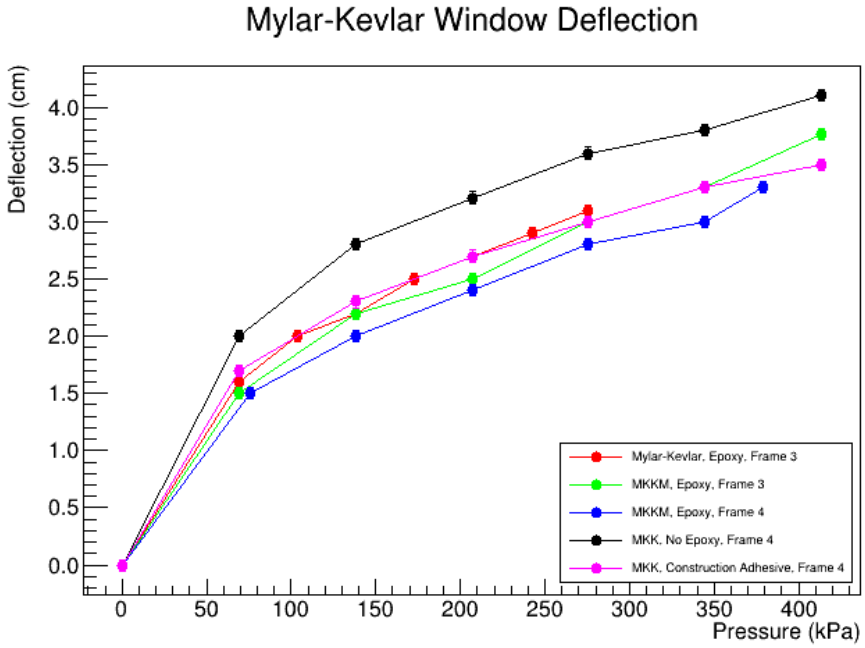

Figure 5.22: Deflection versus pressure for the five window configurations in tests 4 to 8, using Frames 3 and 4.

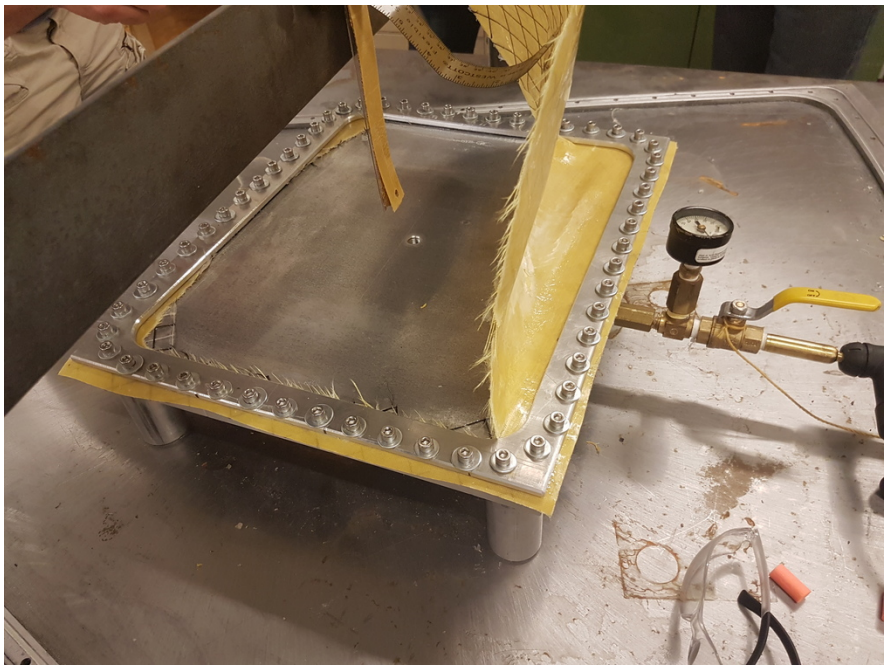

Figure 5.23: Mylar-Kevlar window after bursting during Test 4.

the measurement apparatus as shown in Fig. 5.23. Fig. 5.24 shows the dismantled window after the failure. It is hypothesized that the sharp corner of the inner circumference of the flange may have cut into the window when under pressure, causing the failure. After this test, the inner circumference of Frame 3 was given a radius by first using a 45° bevel cutter, and then filing smooth.

Test 5: Pre-stretched Mylar-Kevlar-Kevlar-Mylar and Epoxy, Frame 3

For this test, an additional layer of Mylar-Kevlar was added to increase the tensile strength. A bonded Mylar-Kevlar layer was stretched over the wooden frame as in Test 4 (Fig. 5.21). The Kevlar was coated with 5 minute epoxy and another bonded Mylar-Kevlar over the frame while the epoxy was still wet, with the second layer of Kevlar in contact with the epoxy. This places two layers of Kevlar bonded by epoxy in between two layers of Mylar. The epoxy was set and the window was mounted to Frame 3 and cut from the wooden frame.

Results for the pressure test are shown in Fig. 5.22 in green. Above 30 psi, the material layers began to separate around the edge, outside the window flange as shown in Fig. 5.25. The window reached a pressure of 60 psi (414 kPa) with no obvious signs of failure. The pressure however decreased to 54 psi while the window expanded an additional 4 mm.

The window was left pressurized for 30 minutes, after which the pressure had decreased to 25 psi. The

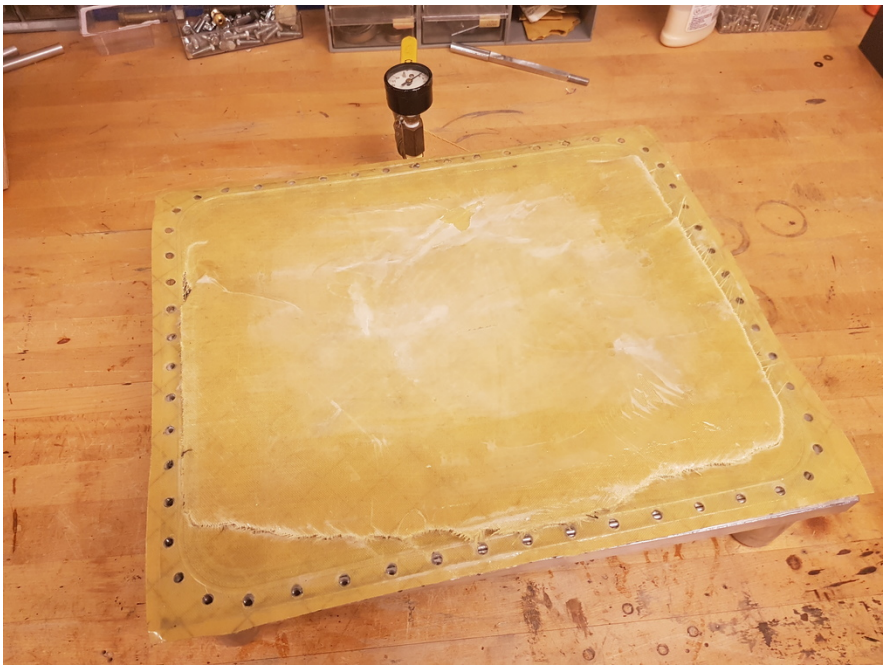

Figure 5.24: Dismantled Mylar-Kevlar window after pressure failure following Test 4.

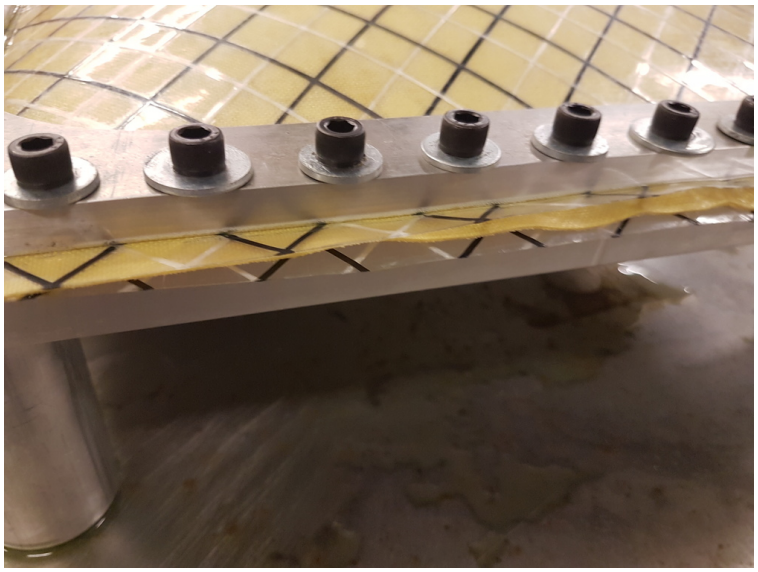

Figure 5.25: Separation of window layers outside of the frame during Test 5.

Figure 5.26: Close up of separated material layers after disassembly following Test 5.

soapy spray was used to check for leaks but did not find any. The window was re-inflated to 35 psi at which point air was found to be escaping between the separated material layers.

The bolts were tightened, which appeared to remedy the leaking. It was then inflated again to 52 psi when the leaking resumed. Curiously, once the pressure had dropped to 30 psi, the window appeared to stop leaking and maintain its pressure. The window was at this point depressurized and dismantled.

Fig. 5.26 shows the separated material layers after disassembly. It appears that the Kevlar layers were drawn inwards, while the Mylar remained mostly in place. As the Kevlar was drawn inward, the force was placed on the material near the bolts, leading to the tear also visible in Fig. 5.26. It was at this point hypothesized that the upward force of the inflated window was causing a prying action on the flange, weakening the grip on the material. It was then decided a thicker flange was likely necessary and Frame 4 was constructed.

Test 6: Pre-stretched Mylar-Kevlar-Kevlar-Mylar, and Epoxy, Frame 4

This window was prepared with the same procedure as Test 5, but mounted to the new Frame 4. Initial pressure test results are shown in Fig. 5.22.

Between 50 and 60 psi, the same edge separation as in Test 5 was observed. The window reached a pressure of 60 psi with no apparent failure. With the valve sealed the pressure dropped to 58 psi as the window expanded an additional 2 mm.

Over the next 30 minutes, the pressure decreased to 50 psi and the deflection increased an additional 4 mm. The soap spray revealed no leaks around the circumference. The window was re-inflated to 60 psi and

Figure 5.27: Close up of damage to Kevlar layers following Test 6.

left sealed. For the next 4 to 5 hours, the pressure decreased at a steady rate of less than 5 psi per hour. At some time between 4 and 5 hours after sealing, the pressure dropped more rapidly to 23 psi, when it seemed to stabilize, holding for at least 12 hours.

Upon attempted re-inflation, it was found to be leaking around one of the bolts. Disassembly revealed much more extensive damage than the previous test, as shown in Fig. 5.27, despite the fact that this test appeared to be an improvement. Once again, the two Mylar layers remained mostly in place while the Kevlar slid between them. It was suggested that it may be beneficial to remove the top layer of Mylar so that the wire could contact the Kevlar directly and improve the grip.

Further damage was noted along the opposite edge, as shown in Fig. 5.28. Here, it appears that the top layer of Mylar was cut by a sharp edge of the wire groove against the Mylar. Following this test, the inside of the wire groove on Frame 4 was radiused similarly to the inner circumference of Frame 3.

It was also noted during disassembly that the two Kevlar layers, bonded by epoxy, were easily pulled apart by hand. Separating the Mylar from the Kevlar (bonded only by the adhesive backing) required significantly more force. It was therefore decided to forego the epoxy bonding in the next test.

Figure 5.28: Closeup detail of damage to top Mylar layer along the location of the wire groove, after Test 6.

Test 7: Pre-stretched Mylar-Kevlar-Kevlar, Frame 4

This test omits both the second layer of Mylar and the epoxy. A layer of Kevlar was bonded to a layer of Kevlar using the included adhesive. A second layer of Kevlar was then bonded to the first layer of Kevlar also using the included adhesive. This three layer material was then stretched over the wooden frame as in Test 4, and mounted to Frame 4. At this point, consideration was also given to the tightness of the bolts. Each bolt was torqued to 100 ft-lb (136 Nm). Initial results of the pressure test are shown in Fig. 5.22.

Once again, layer separation was observed between 50 and 60 psi. After reaching 60 psi, soapy spray revealed leaking around one of the bolts. The leak slowed as pressure leveled at approximately 35 psi after less than 10 minutes.

It was agreed that little more of value could be learned from this particular test, so the opportunity was taken to perform a puncture test. A screwdriver was placed against the center of the window and struck with a mallet. The screwdriver pierced the window, making only a small puncture, through which the window rapidly, but steadily, deflated. There was no explosive burst, or further damage to the window from the puncture.

Disassembly revealed similar damage to Test 5, as expected.

Test 8: Pre-stretched Mylar-Kevlar-Kevlar (MKK), Construction Adhesive, Frame 4

Preparation of this window follows the same procedure as Test 7, with the addition of LePage PL premium construction adhesive to the wire groove on both the base plate and flange, in order to try to bond the frame directly to the window material. The window was clamped into Frame 4 and left for 72 hours before being cut from the wooden frame. The bolts were once again torqued to 100 ft-lb. Initial results of the pressure test are shown in Fig. 5.22.

This configuration was able to reach 60 psi without any apparent issue. After closing the valve, the pressure slowly decreased to 50 psi total, while expanding an additional 3 mm. As this happened, the edges of the material begin to separate as in the previous tests. The pressure then dropped more rapidly to 50 psi and the window began to leak through one of the bolts.

It was decided nothing more could be learned from this window and it was disassembled, revealing the expected damage as in Test 5.

These tests have revealed that Kevlar most likely has sufficient tensile strength to hold the needed pressure. However, it is prone to tearing when subject to shear stress, which is difficult to eliminate within the flange's clamping mechanism. Furthermore, the Kevlar's resistance to stretching leads to greater forces on the frame (due to the decreased radius of curvature, Equations 5.1 and 5.2). It seems pursuing Kevlar as a solution would require significant redesigns to the frame, which may not be feasible. At this point, it was clear that alternative window materials must be considered.

5.2.5 Carbon Fiber Shell

Following previous failures with flexible window materials, a rigid shell became a worthwhile consideration. Excess carbon fiber was available from a previous prototyping project at University of Regina.

The shells were made using the following materials:

- Fibre Glast 1069 3K, 2x2 Twill Weave Carbon Fiber Fabric (0.012 mil thickness)
- Fibre Glast System 2000 Epoxy Resin
- Fibre Glast 2020 Hardener
- Challenge Sailcloth Mylar
- Challenge Sailcloth Kevlar

Figure 5.29: MDF mold for Shell 1.

Flat Mock-Up Windows

In developing a fabrication procedure for a carbon fiber shell, two small mock-up windows were briefly tested. These windows were made with two layers of carbon fiber brushed with epoxy resin while laid flat. In the first window, the carbon fiber was simply mounted to Frame 4 with a layer of Mylar. In the second window, a layer of Mylar was pre-stretched by mounting to Frame 4 and leaving inflated at 10 psi overnight, before removing and mounting along with the carbon fiber.

Both of these windows failed at less than 40 psi. These mock-ups pushed testing toward molded shells with a harder epoxy mixture.

Carbon Fiber Shell 1: 1" Depth

Shell 1 was made to fit Frame 4 using 3 layers of carbon fiber and a mixture of resin and hardener at a 100:23 ratio. A mold was carved out of medium density fiberboard (MDF) with a 1" depth, approximating the shape of an inflated window on Frame 4, as shown in Fig. 5.29

The first layer of carbon fiber was laid over the mold before being coated with the epoxy mixture. A second and third layer of carbon fiber follow, each with a coating of the epoxy mixture. The shell was then left to cure for at least 8 hours.

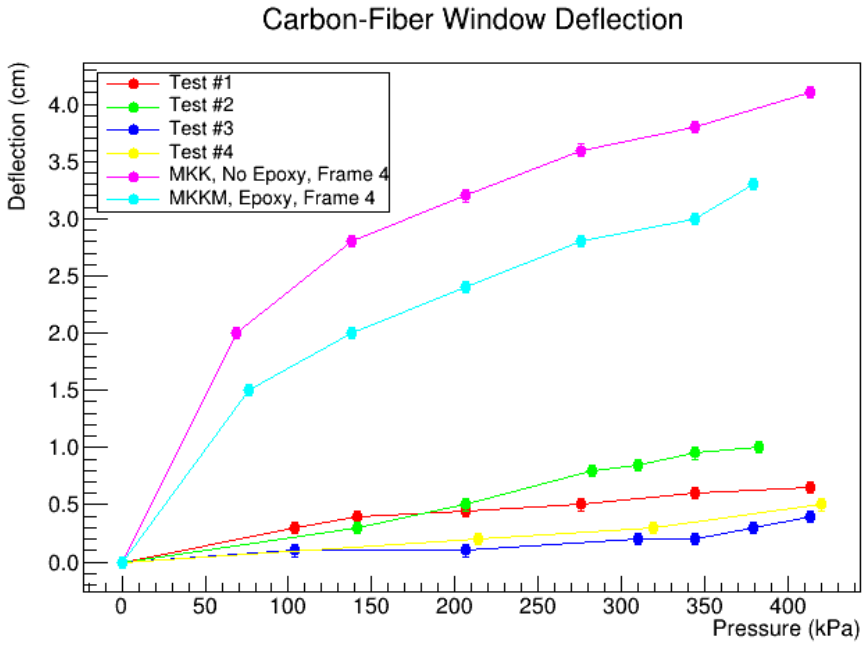

Figure 5.30: Deflection versus pressure for miniature sized carbon fiber shells, with two of the best results from the Kevlar tests for comparison.

Once cured, the shell is removed from the mold and both sides are sanded smooth. A layer of Kevlar is layered over the shell using the adhesive backing. This to ensure that, in the event of a failure, any sharp pieces of carbon fiber are contained. Excess carbon fiber is cut from the sides leaving only a small overhang past the dimensions of Frame 4. Four small holes are drilled into the carbon to make sure air can escape from between the Mylar and the shell, allowing the Mylar to expand under pressure and brace against the shell.

The first test with Shell 1 was performed with a new piece of un-stretched Mylar and no clamping wire. The initial results are shown in Fig. 5.30. Throughout this test the shell was observed to make creaking and popping sounds as pressure was increased. At approximately 40 psi the window was found to be leaking between the frame and through the bolt holes. By 60 psi, the leak rate was outpacing the pump.

C-clamps were applied around the frame to try to reduce leaking, as shown in Fig. 5.31. This was successful in reducing the leak rate, though the leak was still significant. This suggested that while the shell was able to handle the stress, the pressure seal was failing due to poor contact with the O-ring.

The shell was dismantled and refitted with a new Mylar layer, pre-stretched on Frame 4 at 10 psi, and the clamping wire in place. Initial results are again shown in Fig. 5.30 as Test 2. Creaking was noticeably louder during this test, and deflection increasing much faster. The shell was suspected to have been compromised,

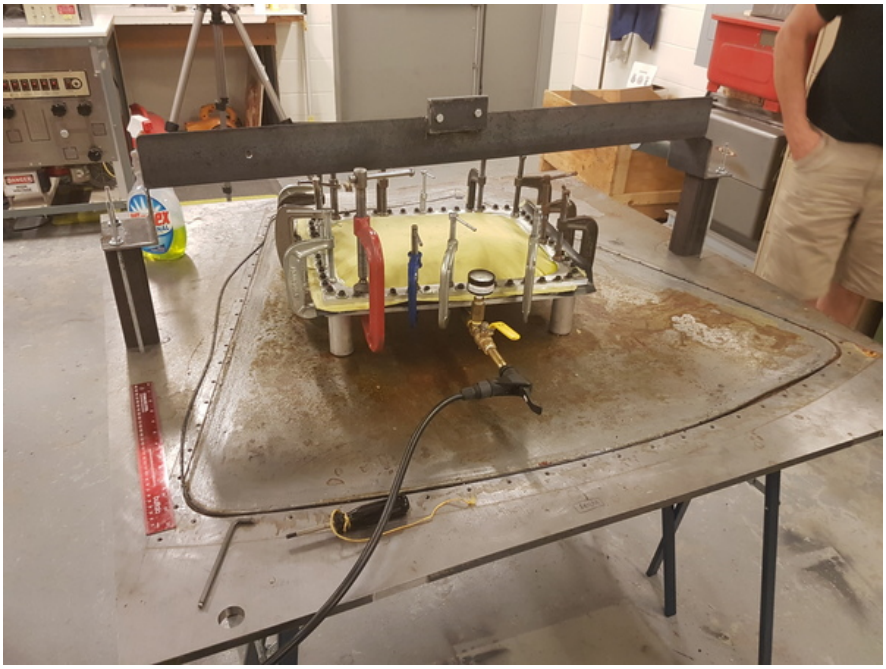

Figure 5.31: C-clamps applied to window frame to try to reduce leaking during a test of Shell 1.

so the decision was made to force a failure of this window to observe failure mode. The window was inflated to 60 psi, where it remained briefly before the carbon fiber burst, tearing the Kevlar with it. The Mylar remained briefly intact before bursting. Fig. 5.32 shows the aftermath of the failure.

Carbon Fiber Shell 2: 1.5" Depth

The fabrication of this shell followed the same procedure as Shell 1, but with a new mold, giving a 1.5" depth. During this test, the creaking sounds were greatly reduced, indicating an improvement in the deeper shell design. However the pressure seal again failed at 60 psi, leaking air around the bolts. Upon disassembly, the carbon fiber appeared to have cracked underneath the flange, which possibly caused failure in the pressure seal, while maintaining the integrity of the load bearing part of the window. The deflection of the window from this test is shown in Fig. 5.30 as Test 3.

Carbon Fiber Shell 3: Sandwich Design

The design of the third shell followed the same design as Shells 1 and 2 in terms of material layers and epoxy mixture, but included a permanently bonded aluminum frame. The shell was fabricated using the same 1.5" mold as in Shell 2, and a layer of Mylar pre-stretched on Frame 3. The circumference of the Mylar was sanded on both sides with a Scotch-Brite pad to create a better bonding surface. The aluminum flange from

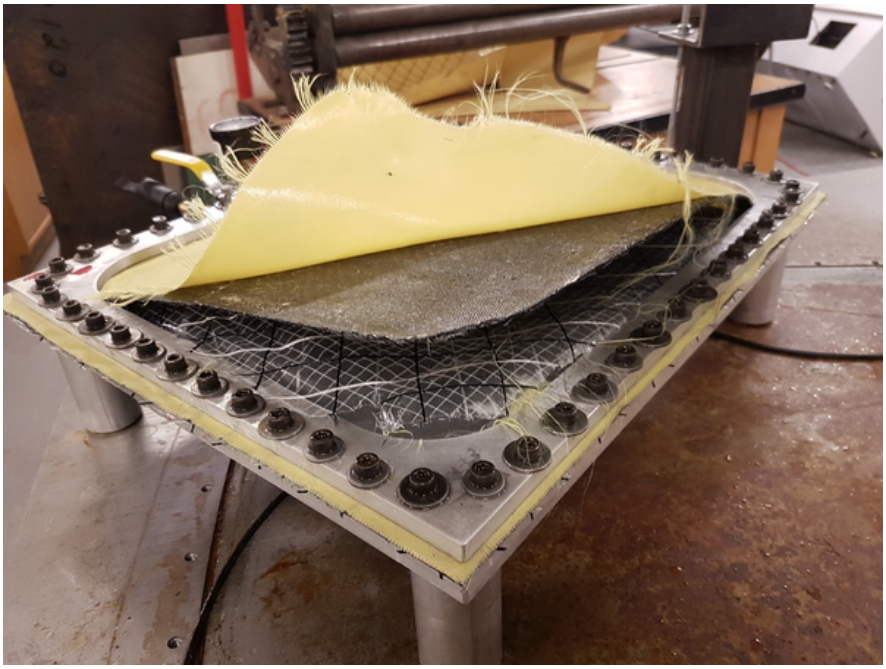

Figure 5.32: Aftermath of forced failure of Shell 1

Frame 3 was placed down with the grooves facing up, and the O-ring in place and coated with the same epoxy mixture used in the shell. The Mylar was then laid on top of the flange, with the bolt holes aligned, followed by another coating of epoxy mixture on the circumference. The shell was then placed on top of the Mylar, and epoxy is again applied to the circumference. Finally, the aluminum flange of Frame 4 is placed on top. The circumference was then weighted down while the epoxy cured.

The end product is a single unit consisting of the two aluminum flanges from Frames 3 and 4, Mylar sealing layer, and carbon fiber shell. Construction of this window effectively retired Frames 3 and 4 as they were now permanently bonded to this window. This assembly was then mounted to the shared steel base plate of Frames 3 and 4 for testing.

This window was able to reach a pressure of 60 psi with only minor creaking and no noticeable leaking. The deflection during this test is shown in Fig. 5.30 as Test 4. The window maintained this pressure for just over three weeks with no noticeable decrease. The window was depressurized and dismantled for inspection. No damage was found in either the shell or the Mylar layer, and so the window was reassembled and inflated again to 60 psi (without stopping for measurements) and left sealed. The window maintained pressure for approximately one month, at which point the result was deemed satisfactory, and the window was deflated and disassembled for inspection. All layers of the window, again, appeared undamaged.

Figure 5.33: Foam cloth being stretched over the wooden frame as a mold for the full-size carbon fiber shell. The yellow color similar to the Kevlar is coincidental.

Carbon Fiber Shell 4: Full Size

The construction of this shell followed the same procedure as the previous shell designs. However, due to the greatly increased size, the mold was constructed using foam cloth stretched over a wooden frame, as shown in Fig. 5.33.

The foam cloth was then coated with the epoxy mixture and allowed to cure. The finished mold is shown in Fig. 5.34. Construction of the shell itself then proceeded as before, using this new mold. The shell was then mounted to Frame 1.

During the first test, above 12 psi the window began leaking from the long, straight sides underneath the flange. The window reached a maximum pressure of 14.5 psi with no damage to the shell. However, loud creaking sounds were observed, and leaking continued, so testing was discontinued. The deflection data are shown in Fig. 5.35 by the red points.

In order to address the side leaking, the flange was reinforced with quarter-inch thick aluminumm bars along the straight sides and C-clamps on the shortest side, as shown in Fig 5.36.

The window reached a pressure of 15 psi with no signs of leaking, though the creaking sounds repeated. The deflection data for the second inflation are shown in Fig. 5.35 by the green points. The window was left at pressure and over the next three days, dropped to 14.4 psi while also expanding an additional 4 mm. The

Figure 5.34: Finished mold for full-size carbon fiber shell. The yellow material is a foam cloth and similarity to the Kevlar is coincidental.

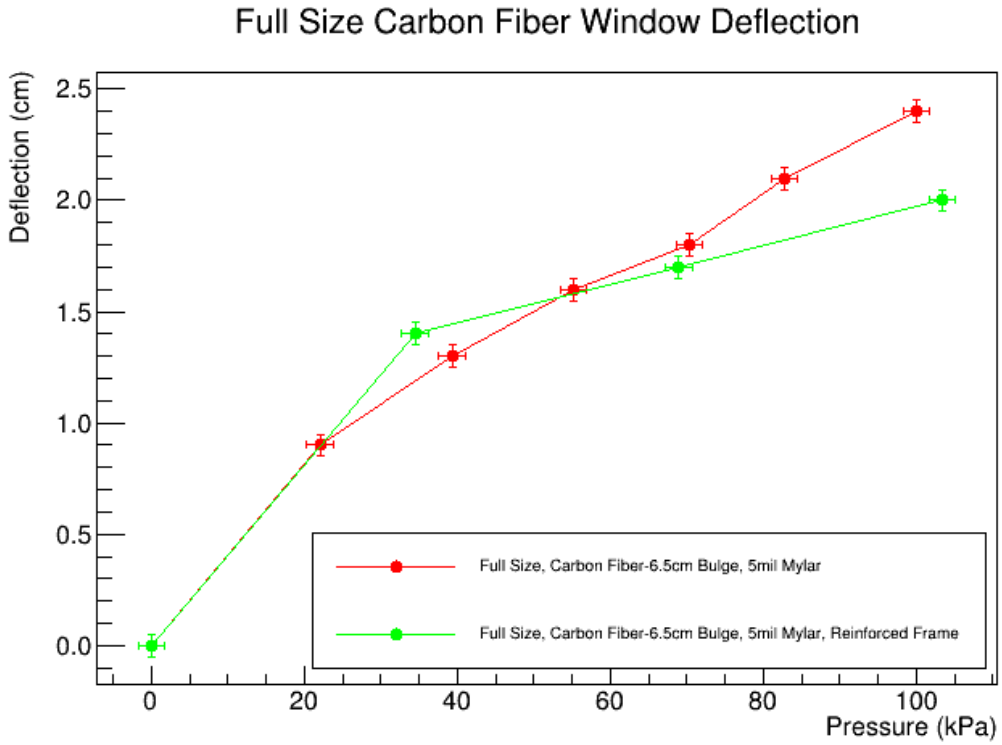

Figure 5.35: Deflection of full size carbon fiber window vs pressure. The dashed red/green line from 0 to 20 kPa simply indicates overlapping of the two lines.

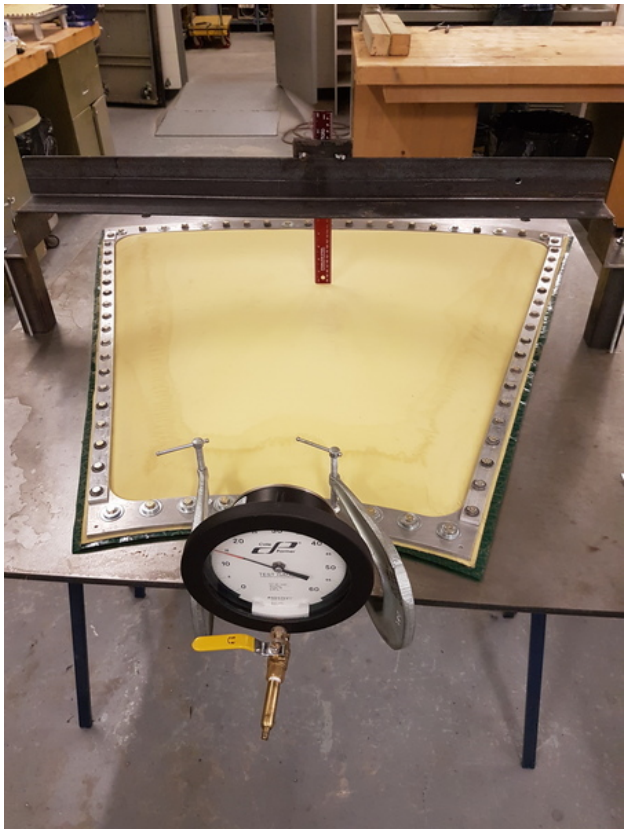

Figure 5.36: Carbon fiber shell 4 on Frame 1, with reinforcing aluminum bars on the left and right sides.

window was then reinflated to 15 psi. Again, over the next few days, the pressure decreased, this time to 14.8 psi. The pressure decreased no further for at least another 13 days, after which, the pressure dropped to 5 psi while unattended. The window was unable to maintain pressure again after this time, indicating failure of the gas seal, though dissasembly showed no obvious damage. The failure of this window most likely lies in the unrevised design of Frame 1 rather than the carbon fiber shell.

Carbon Fiber Shell 5: Small Flat Window

While the previous tests appeared to be moving in the right direction, and suggest a significant positive relationship between the built-in bulge and the structural integrity, concerns have been raised about reproducibility. The process of manufacturing shell 4 is highly involved and contains a lot of room for inconsistencies. Eventually, at least a dozen windows will need to be manufactured to construct the entire HGC, along with replacements. As such, a window design that is easier to produce is desirable.

For this shell, the same epoxy was used as in the previous shells, but 3 layers of Fibre Glast's thicker, 12K 10×10 carbon fiber fabric (30 mil thickness) were used. The construction of this window followed a similar procedure to the flat mock-up windows, but with the addition of Permatex Ultra Copper gasket maker around the perimeter between the base plate and Mylar layer, along with the O-ring.

In testing, this window was able to hold a pressure of 60 psi with minimal deflection, and reached this pressure with no notable creaking sounds, or leaking. The window was able to maintain pressure for nearly a full year, losing less than 10 psi in this time. Fig. 5.37 shows Shell 5 near the end of this period. In addition, both the shell itself and the sealing mylar layer showed no damage upon disassembly, as shown in Fig. 5.38.

This test was, by a wide margin, the most successful small window test, and clearly indicates that future full size window tests should use the same configuration.

Figure 5.37: Shell 5 still under pressure after approximately one year.

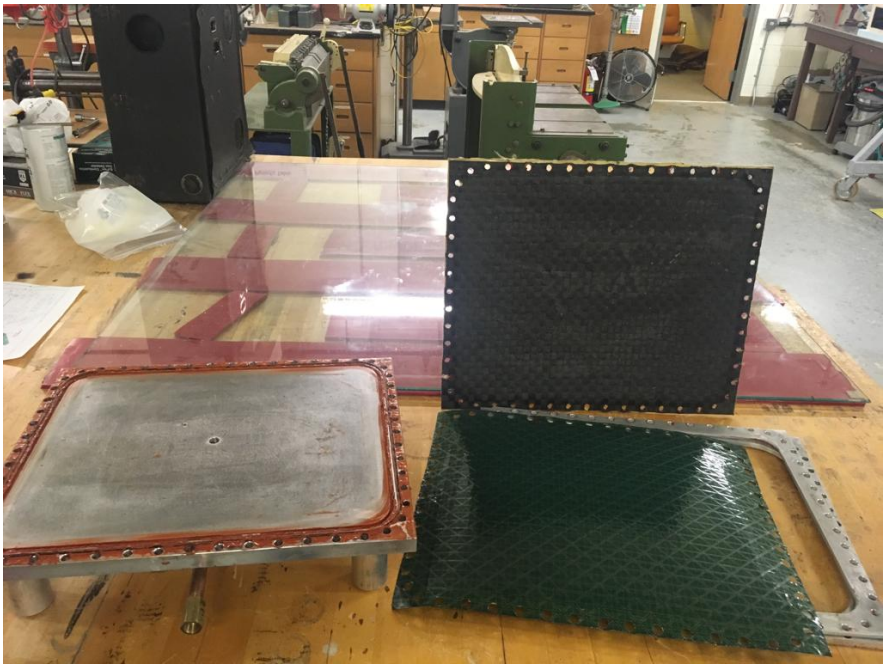

Figure 5.38: Shell 5 after disassembly following approximately one year under pressure.

5.3 Summary

These tests have found a combination of Mylar and carbon fiber to be a strong candidate for the SoLID HGC entry window. The carbon fiber is strong enough to withstand the pressure without failing, while being lower Z and lower density than similarly strong alternatives, such as aluminum.

Several challenges and questions remain, however. The design and layout of the clamping flange must be revised to address issues highlighted throughout testing. Omission of the clamping wire and increased spacing between the O-ring groove and bolt holes is suggested for use with the carbon fiber shell.

The window must also pass some safety tests, such as a puncture test to demonstrate that if the window fails, it does so without damaging surrounding equipment. A complete segment of the HGC must also be constructed and tested with the window.

Chapter 6

Conclusions and Outlook

The two main components of this thesis, the DEMP event generator, and the SoLID Heavy Gas Cherenkov Window prototyping, have concluded successfully.

6.1 Event Generator Status

The rewrite of the DEMP event generator is now ready to be used in further studies approaching the beginning of SoLID science and the DEMP experiment. The next steps for the generator will involve generating much larger data sets in order to improve upon projections used in this thesis as well as in the DEMP proposal [5]. In particular, the greater statistics will allow for studies on the possibility of using the proton track from SoLID to improve missing mass and momentum resolution. This rigorous testing should also expose any remaining bugs in the code.

The DEMP event generator will be an invaluable tool leading up to the completion of SoLID and the start of the DEMP experiment. It will allow for continued study of the extraction of the $A_{UT}^{\sin(\phi-\phi_S)}$ and $A_{UT}^{\sin(\phi_S)}$ under the changing design and specifications of SoLID.

The improved kinematics method used in the DEMP event generator also has potential application to other experiments. Interest has been expressed in a "clean" version of the kinematics solver, isolated from experiment and model dependent calculations, for use in proposed experiments in the planned Electron Ion Collider (EIC) [49]. While the DEMP generator calculates cross sections and weights along with each event, there is no reason this cannot be done afterwards by a secondary program. Furthermore, while DEMP is a fixed target experiment, the kinematics solver is agnostic to this, and easily accommodates two moving

initial state particles, such as in the EIC, or in the case of Fermi momentum (which is not treated as a special case).

It may furthermore be possible to adapt the kinematics component of the DEMP event generator into a fully general kinematics generator. Almost any subatomic physics experiment requires a Monte-Carlo simulation for acceptance and/or phase-space studies during the proposal stages. A singular solution for the computationally intensive kinematics calculations may be a worthwhile endeavor.

6.2 Continuing HGC Window Prototyping

The prototyping work for the SoLID-HGC entry window (section 5.2) has produced a strong candidate for a suitable set of materials and configuration, that satisfy both experimental and safety requirements. In continuation of this work, further studies are under way, focusing primarily on making these results more practicable. Of most significant concern is the reproducibility of the carbon fiber shell fabrication. While earlier results of this thesis suggest that a larger built-in curve improves the structural integrity of the shell, the process of creating these shells proves challenging to perform consistently, and the final test demonstrated that a flat window is feasible if thicker carbon fiber is used.

As such, testing of flat formed, full size windows is underway at University of Regina. One such window has been constructed, reaching a pressure of 26 psi in two separate tests, nearly four times operating pressure, again with minimal bulging, and no creaking. This shell was constructed for the original full size frame. However, the geometry of the entry window has changed in response to feedback from this project, as well as from other SoLID component prototyping. Thus, a new test frame and window should be constructed, not only to incorporate these design changes, but also to address outstanding issues with the placement of the O-ring groove and bolt holes discussed in Chapter 5. This will also prove useful as the project approaches construction of a full segment of the HGC.

New simulations have been performed by Zhiwen Zhao [50] using an aluminum front entrance window. This simulation showed that earlier concerns about pair production were unfounded, and an aluminum window would have worked. However, the tensile requirements demand the use of aerospace quality 2024-T4 aluminum, of 40 mil thickness. This material is both expensive, and difficult to obtain. The newly developed carbon fiber window is more cost effective, and requires more easily sourced materials.

6.3 Status of SoLID

Current outlook for the SoLID project is promising. After budgetary reviews considering design changes, including feedback from the HGC window prototyping, the project is expected to receive full funding of approximately $80M USD. SoLID is expected to be science ready within approximately the next five years, with DEMP as the flagship experiment of the SoLID-GPD program.

References

[1] *SoLID (Solenoidal Large Intensity Device) Preliminary Conceptual Design Report*. 2014. URL: https://hallaweb.jlab.org/12GeV/SoLID/files/solid_precdr.pdf.

[2] P. Bosted et al. *Target Single Spin Asymmetry in Semi-Inclusive-Deep-Inelastic* $(e, e', \pi^{\pm})$ *Reaction on a Transversely Polarized* ^{3}*He Target at 11 GeV*. 2008. URL: http://hallaweb.jlab.org/collab/PAC/PAC34/PR-09-014-transversity.pdf.

[3] B. Q. Ma et al. *Asymmetries in Semi-Inclusive-Deep-Ineslastic* $(e, e', \pi^{\pm})$ *Reactions on a Longitudinally Polarized* ^{3}*He Target at 8.8 and 11 GeV*. URL: https://www.jlab.org/exp_prog/PACpage/PAC37/proposals/Proposals/New%20Proposals/PR-11-007.pdf.

[4] A. Kolarkar et al. *Target Single Spin Asymmetry in Semi-Inclusive-Deep-Ineslastic* $(e, e', \pi^{\pm})$ *Reactions on a Transversely Polarized Proton Target*. URL: https://www.jlab.org/exp_prog/proposals/11/PR12-11-108.pdf.

[5] Garth M. Huber et al. *Measurement of Deep Exclusive* π^- *Production using a Transversely Polarized* ^{3}*He Target and the SoLID Spectrometer*. 2016. URL: https://misportal.jlab.org/pacProposals/proposals/1317/attachments/99852/Proposal.pdf.

[6] Wikipedia, the free encyclopedia. *The Standard Model of Elementary Particles*. [Online; accessed November 23, 2018]. 2006. URL: https://commons.wikimedia.org/wiki/File:Standard_Model_of_Elementary_Particles.svg.

[7] Steven Weinberg. "A Model of Leptons". In: *Phys. Rev. Lett.* 19 (21 Nov. 1967), pp. 1264–1266. DOI: 10.1103/PhysRevLett.19.1264. URL: https://link.aps.org/doi/10.1103/PhysRevLett.19.1264.

[8] David J. Griffiths. *Introduction to Elementary Particles*. 2nd ed. Wiley-VCH, 2010.

[9] Hans Frauenfelder and Ernest M. Henley. *Subatomic Physics*. 2nd ed. Prentice Hall, 1994.

[10] N. F. Mott and Harrie Stewart Wilson Massey. *The theory of atomic collisions*. 3rd ed. Clarendon, 1965.

[11] E. D. Bloom et al. "High-Energy Inelastic $e-p$ Scattering at 6° and 10°". In: *Phys. Rev. Lett.* 23 (16 Oct. 1969), pp. 930–934. DOI: 10.1103/PhysRevLett.23.930. URL: https://link.aps.org/doi/10.1103/PhysRevLett.23.930.

[12] C. Patrignani et al. "Review of Particle Physics". In: *Chin. Phys.* C40.10 (2016), p. 100001. DOI: 10.1088/1674-1137/40/10/100001.

[13] Tom Vrancx and Jan Ryckebusch. "Charged-pion electroproduction above the resonance region". In: *Phys. Rev. C* 89 (2 Feb. 2014), p. 025203. DOI: 10.1103/PhysRevC.89.025203. URL: https://link.aps.org/doi/10.1103/PhysRevC.89.025203.

[14] Tom Vrancx et al. "$K^+\Lambda$ electroproduction above the resonance region". In: *Phys. Rev. C* 89 (6 June 2014), p. 065202. DOI: 10.1103/PhysRevC.89.065202. arXiv: 1404.4156.

[15] J. Nys and J. Ryckebusch. *StrangeCalc*. 2018. URL: http://rprmodel.ugent.be/calc/.

[16] H. P. Blok et al. "Charged pion form factor between $Q^2 = 0.60$ and 2.45 GeV^2. I. Measurements of the cross section for the ^{1}H$(e, e'\pi^+)n$ reaction". In: *Phys. Rev. C* 78 (4 Oct. 2008), p. 045202. DOI: 10.1103/PhysRevC.78.045202. URL: https://link.aps.org/doi/10.1103/PhysRevC.78.045202.

[17] Zafar Ahmed. Private Communications. 2016-2019.

[18] A. V. Radyushkin. *Generalized Parton Distributions*, pp. 1037–1099. DOI: 10.1142/9789812810458_0027. eprint: arXiv:hep-ph/0101225.

[19] L. L. Frankfurt et al. "Hard exclusive pseudoscalar meson electroproduction and spin structure of the nucleon". In: *Phys. Rev. D* 60 (1 June 1999), p. 014010. DOI: 10.1103/PhysRevD.60.014010. URL: https://link.aps.org/doi/10.1103/PhysRevD.60.014010.

[20] John C. Collins et al. "Factorization for hard exclusive electroproduction of mesons in QCD". In: *Phys. Rev. D* 56 (5 Sept. 1997), pp. 2982–3006. DOI: 10.1103/PhysRevD.56.2982. URL: https://link.aps.org/doi/10.1103/PhysRevD.56.2982.

[21] S. V. Goloskokov and P. Kroll. "An attempt to understand exclusive pi+ electroproduction". In: *The European Physical Journal C* 65.1 (Nov. 2009), p. 137. DOI: 10.1140/epjc/s10052-009-1178-9. eprint: arXiv:0906.0460.

[22] S. V. Goloskokov and P. Kroll. "Transversity in hard exclusive electroproduction of pseudoscalar mesons". In: *The European Physical Journal A* 47.9 (Sept. 2011), p. 112. DOI: 10.1140/epja/i2011-11112-6. eprint: arXiv:1106.4897.

[23] Ivana Hristova. "Transverse-Target Single-Spin Azimuthal Asymmetry in Hard Exclusive Electroproduction of Single Pions at HERMES". PhD thesis. Humboldt University of Berlin, 2007.

[24] M. Diehl and S. Sapeta. "On the analysis of lepton scattering on longitudinally or transversely polarized protons". In: (2005). DOI: 10.1140/epjc/s2005-02242-9. eprint: arXiv:hep-ph/0503023.

[25] A. Bacchetta et al. "Single-spin asymmetries: The Trento conventions". In: *Physical Review D* 70.11, 117504 (Dec. 2004), p. 117504. DOI: 10.1103/PhysRevD.70.117504. eprint: hep-ph/0410050.

[26] S. V. Goloskokov and P. Kroll. Private Communications. 2009-2017.

[27] *Jefferson Lab.* URL: https://www.jlab.org/.

[28] J. L. Friar et al. "Neutron polarization in polarized ^{3}He targets". In: *Phys. Rev. C* 42 (6 Dec. 1990), pp. 2310–2314. DOI: 10.1103/PhysRevC.42.2310. URL: https://link.aps.org/doi/10.1103/PhysRevC.42.2310.

[29] C. Ciofi degli Atti and S. Scopetta. "On the extraction of the neutron spin structure functions and the Gerasimov-Drell-Hearn integral from the process He→3(e→,e) in the resonance region". In: *Physics Letters B* 404.3 (1997), pp. 223–229. ISSN: 0370-2693. DOI: https://doi.org/10.1016/S0370-2693(97)00576-5. URL: http://www.sciencedirect.com/science/article/pii/S0370269397005765.

[30] R.-W. Schulze and P. U. Sauer. "Polarized deep-inelastic lepton scattering from the polarized two- and three-nucleon bound states". In: *Phys. Rev. C* 56 (4 Oct. 1997), pp. 2293–2315. DOI: 10.1103/PhysRevC.56.2293. URL: https://link.aps.org/doi/10.1103/PhysRevC.56.2293.

[31] F. Bissey et al. "Structure functions for the three-nucleon system". In: *Phys. Rev. C* 64 (2 July 2001), p. 024004. DOI: 10.1103/PhysRevC.64.024004. URL: https://link.aps.org/doi/10.1103/PhysRevC.64.024004.

[32] Fabio Sauli. "The gas electron multiplier (GEM): Operating principles and applications". In: *Nuclear Instruments and Methods in Physics Research Section A: Accelerators, Spectrometers, Detectors and Associated Equipment* 805 (2016). Special Issue in memory of Glenn F. Knoll, pp. 2–24. ISSN: 0168-9002. DOI: https://doi.org/10.1016/j.nima.2015.07.060. URL: http://www.sciencedirect.com/science/article/pii/S0168900215008980.

[33] *Flat Panel Type Multianode PMT Assembly H8500 Series*. Hamamatsu. URL: https://www.hamamatsu.com/resources/pdf/etd/H8500_H10966_TPMH1327E.pdf.

[34] Gary Swift. Private Communications. Duke University, 2016-2019.

[35] Rene Brun and Fons Rademakers. "ROOT - An Object Oriented Data Analysis Framework". In: *AIHENP'96 Workshop, Lausane*. Vol. 389. 1996, pp. 81–86.

[36] Baptiste Lepilleur et. al. *JsonCpp*. 2007. URL: https://github.com/open-source-parsers/jsoncpp.

[37] Eric W. Wesstein. *Sphere Point Picking. From MathWorld – A Wolfram Web Resource*. http://mathworld.wolfram.com/SpherePointPicking.html.

[38] Zhihong Ye. *Event Generator for Deep Virtual Meson Proudction for SoLID and EIC*. https://github.com/yezhihong/SoLID-DVMP.

[39] Alexander Deur et al. *Hall-A Single Arm Monte Carlo Simulation Tool in C*. Sept. 2013. URL: https://userweb.jlab.org/~yez/Work/SAMC/.

[40] Xiaodong Jiang. "Measurement of Interference Structure Functions in Quasielastic Proton Knockout From ^{12}C". PhD thesis. University of Massachuetts Amherst, 1998.

[41] R. Schiavilla et al. "Momentum distributions in A = 3 and 4 nuclei". In: *Nuclear Physics A* 449.2 (1986), pp. 219–242. ISSN: 0375-9474. DOI: https://doi.org/10.1016/0375-9474(86)90003-5. URL: http://www.sciencedirect.com/science/article/pii/0375947486900035.

[42] Glenn Rowe et al. "Energy-dependent phase shift analysis of pion-nucleon scattering below 400 MeV". In: *Phys. Rev. C* 18 (1 July 1978), pp. 584–589. DOI: 10.1103/PhysRevC.18.584. URL: https://link.aps.org/doi/10.1103/PhysRevC.18.584.

[43] A. Shinozaki. "Total Cross-Section for the $(\gamma, \pi^+\pi^-)$ process on ^{2}H and ^{12}C from 550-1105 MeV". PhD thesis. University of Regina, 2002.

[44] W. S. C. Williams. *An introduction to elementary particles*. Academic Press, 1971. Chap. Appendix B.

[45] K. G. Dedrick. "Kinematics of High-Energy Particles". In: *Rev. Mod. Phys.* 34 (3 July 1962), pp. 429–442. DOI: 10.1103/RevModPhys.34.429. URL: https://link.aps.org/doi/10.1103/RevModPhys.34.429.

[46] Gary L. Catchen et al. "Scattering kinematics: Transformation of differential cross sections between two moving frames". In: *The Journal of Chemical Physics* 69.4 (1978), pp. 1737–1741. DOI: 10.1063/1.436749. eprint: https://doi.org/10.1063/1.436749. URL: https://doi.org/10.1063/1.436749.

[47] Madico Inc. 64 Industrial Parkway, Woburn, MA 01801.

[48] Challenge Sailcloth, Inc. 711 W 17th St, Cosa Mesa, CA 92627-4345. 949-722-7448.

[49] Zhihong Ye. Private Communications. 2016-2019.

[50] Z. Zhao. Private Communications. 2016-2019.

Appendices

Appendix A

Results from Original Event Generator

Included in the following section are some results of the original event generator, taken from the run-group proposal titled "Measurement of Deep Exclusive π^- Production using a Transversely Polarized ^{3}He Target and the SoLID Spectrometer" [5]. These are included for comparison with results from the new event generator, discussed in Chapter 4.

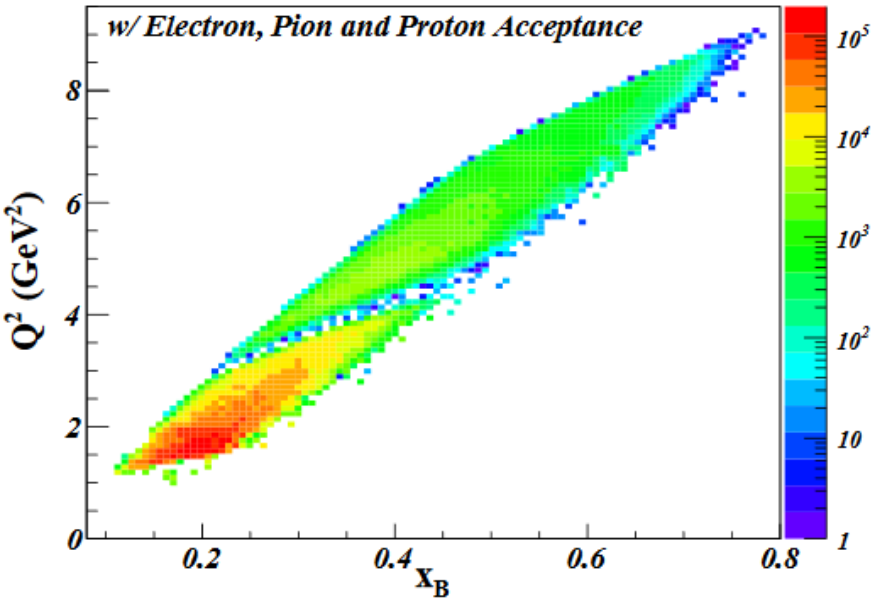

Figure A.1: Kinematic coverage produced by the original event generator in terms of Q^2 and x_B [5]. Compare with Fig. 4.5.

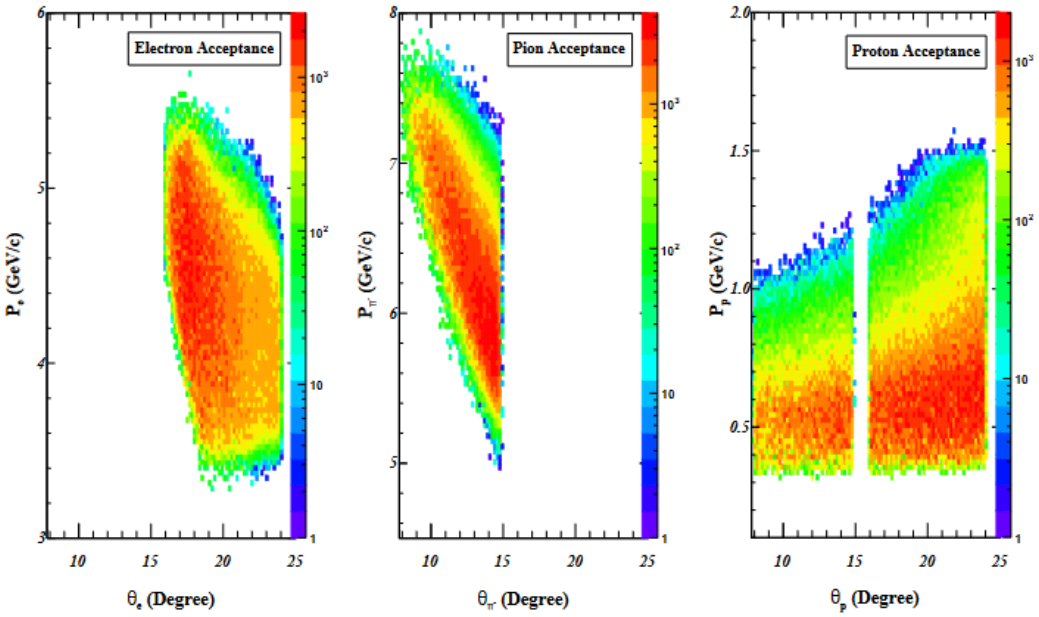

Figure A.2: Kinematic coverage of final state particles produced by the original event generator in terms of p and θ [5]. Compare with Fig. 4.4.

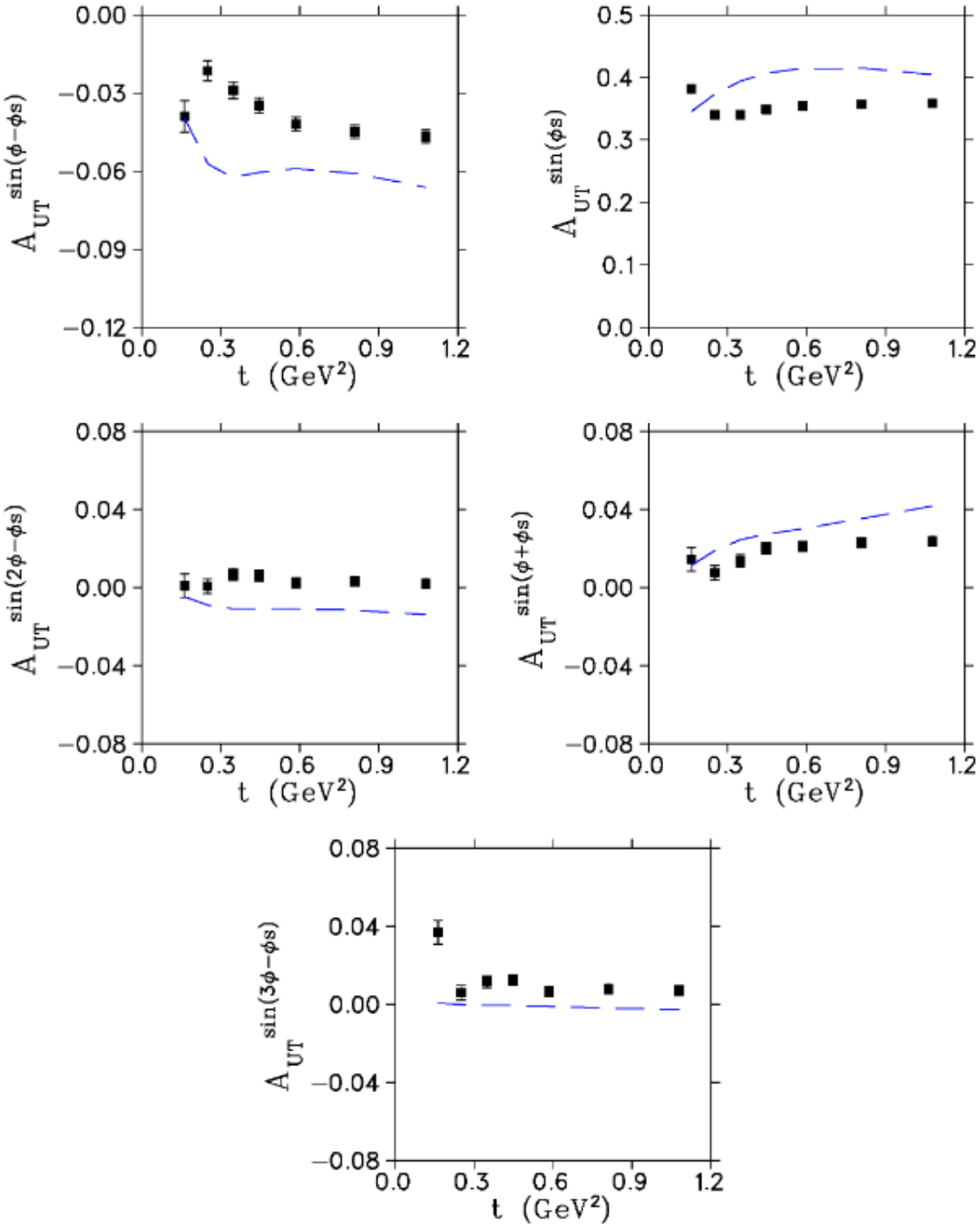

Figure A.3: UML results based on data from the original event generator, including Fermi momentum, multiple scattering, and energy loss effects. [5]. Compare with Fig. 4.18.

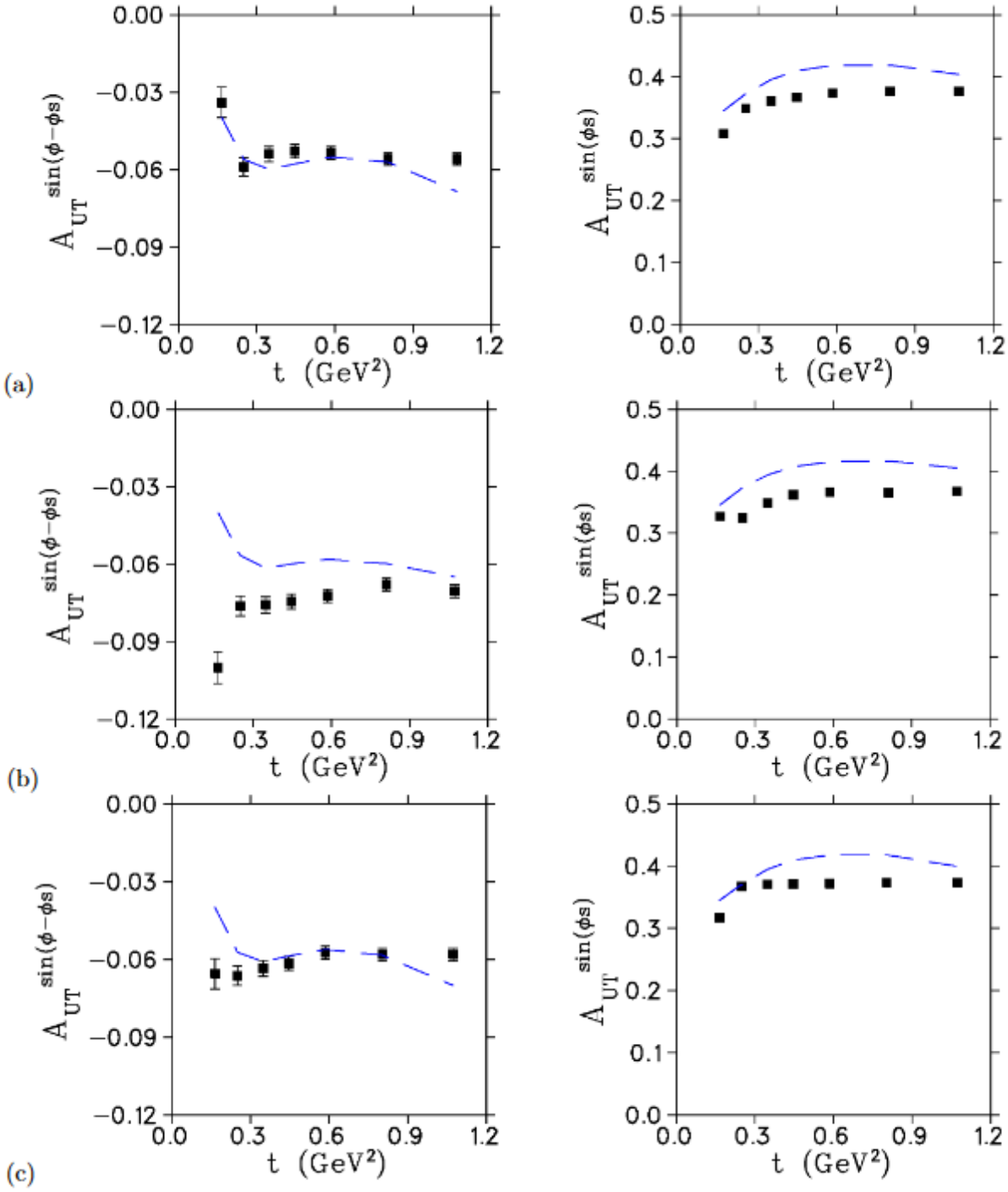

Figure A.4: UML results for the two most theoretically relevent asymmetries, based on data from the original event generator, with a) no corrective effects enabled (compare with Fig. 4.7), b) Fermi momentum enabled (comapre with 4.17) and c) Multiple scattering and energy loss enabled [5].